

UNIVERSIDADE FEDERAL DO ABC
CENTRO DE CIÊNCIAS NATURAIS E HUMANAS
PROGRAMA DE PÓS-GRADUAÇÃO EM NANOCIÊNCIAS E
MATERIAIS AVANÇADOS

PEDRO HENRIQUE THIAYAMITI SANTOS

**MODELAGEM COMPUTACIONAL DE
INTERFACES METAL - ÁGUA**

Orientadora: Profa. Dra. Luana Sucupira Pedroza



SANTO ANDRÉ

2021

FEDERAL UNIVERSITY OF ABC
CENTER FOR NATURAL AND HUMAN SCIENCES
GRADUATE PROGRAM IN NANOSCIENCE AND
ADVANCED MATERIALS

PEDRO HENRIQUE THIAYAMITI SANTOS

COMPUTATIONAL MODELING OF
METAL - WATER INTERFACES

Advisor: Prof. Dr. Luana Sucupira Pedroza



SANTO ANDRÉ

2021

PEDRO HENRIQUE THIAYAMITI SANTOS

**MODELAGEM COMPUTACIONAL DE
INTERFACES ÁGUA/METAL**

Master's thesis presented to the Graduate Program in Nanoscience and Advanced Materials of the Center for Natural and Human Sciences from the Federal University of ABC, for the Defense Examination, as part of the requirements to obtain the Master's degree in Nanoscience and Advanced Materials.

Advisor: Prof. Dr. Luana Sucupira Pedroza

Santo André

2021

Sistema de Bibliotecas da Universidade Federal do ABC
Elaborada pelo Sistema de Geração de Ficha Catalográfica da UFABC
com os dados fornecidos pelo(a) autor(a).

SANTOS, PEDRO HENRIQUE THIAIAMITI
Modelagem computacional de interfaces água/metal / PEDRO
HENRIQUE THIAIAMITI SANTOS. — 2020.

115 fls. : il.

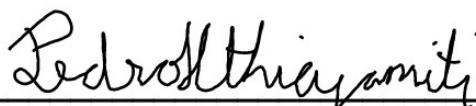
Orientadora: LUANA SUCUPIRA PEDROZA

Dissertação (Mestrado) — Universidade Federal do ABC, Programa
de Pós-Graduação em Nanociências e Materiais Avançados, Santo
André, 2020.

1. Heterogeneous Interfaces. 2. Computational simulation. 3.
DFT. 4. Molecular Dynamics. I. PEDROZA, LUANA SUCUPIRA. II.
Programa de Pós-Graduação em Nanociências e Materiais
Avançados, 2020. III. Título.

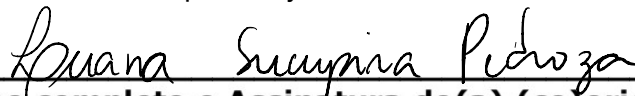
Este exemplar foi revisado e alterado em relação à versão original, de acordo com as observações levantadas pela banca examinadora no dia da defesa, sob responsabilidade única do(a) autor(a) e com a anuência do(a) (co)orientador(a).

Santo André , 04 de Fevereiro de 2021 .



Nome completo e Assinatura do(a) autor(a)

Pedro Henrique Thiayamiti Santos



Nome completo e Assinatura do(a) (co)orientador(a)

Luana Sucupira Pedroza



MINISTÉRIO DA EDUCAÇÃO

Fundação Universidade Federal do ABC

Avenida dos Estados, 5001 – Bairro Santa Terezinha – Santo André – SP

CEP 09210-580 · Fone: (11) 4996-0017

FOLHA DE ASSINATURAS

Assinaturas dos membros da Banca Examinadora que avaliou e aprovou a Defesa de Dissertação de Mestrado do candidato, PEDRO HENRIQUE THIAYAMITI SANTOS realizada em 14 de Dezembro de 2020:


Prof.(a) GUSTAVO TROIANO FELICIANO

UNIVERSIDADE ESTADUAL PAULISTA JÚLIO DE MESQUITA FILHO


Prof.(a) MAURICIO DOMINGUES COUTINHO NETO
UNIVERSIDADE FEDERAL DO ABC

Prof.(a) ALEXANDRE REILY ROCHA
UNIVERSIDADE ESTADUAL PAULISTA JÚLIO DE MESQUITA FILHO

Prof.(a) GUSTAVO MARTINI DALPIAN
UNIVERSIDADE FEDERAL DO ABC


Prof.(a) LUANA SUCUPIRA PEDROZA
UNIVERSIDADE FEDERAL DO ABC - Presidente

* Por ausência do membro titular, foi substituído pelo membro suplente descrito acima: nome completo, instituição e assinatura

“This study was financed in part by the Coordenação de Aperfeiçoamento de Pessoal de
Nível Superior - Brasil (CAPES) - Finance Code 001”



Acknowledgements

First of all, I would like to offer my sincerest thanks and praise to my advisor, Luana Sucupira Pedroza, for not only diligently guiding and supporting my academic development during the last two years but also for being so patient and understanding towards my lack of experience and knowledge since I started this research with barely any previous knowledge on the field. I deeply appreciate your careful revision of all my work, your feedback, your ideas, the constant instruction for methodological rigor, and your encouragement. I hold in high esteem your abilities as a researcher and as a teacher, you set a great example. I for sure could not have done this without you. I would also like to thank you for the access of the Mildred cluster, it speeded up the research.

I would like to mention that I feel in debt to the PostDoc Márcio Sampaio for your teaching and your support in the development of the last part of the research. You helped me a lot with great insights into the theory and also helped me understand the logic of the many codes used in the protocol. Your guidance and contribution was invaluable.

Moreover, I would like to thank the PostDoc Aline Olimpio Pereira who actually developed the protocol which I used in this research.

I also would like to thank the ABCsim group, whose members took me in during this journey. In this matter, I would like to thank professor Ronei Miotto for the weekly meetings where he shed some light on basic quantum mechanics. And I also would like to express my gratitude to professor Yuri Alexandre Aoto, for Python lessons and for the amazing opportunity to contribute to his book. In addition, I would like to especially express my deep gratitude to Matheus Morato Ferreira de Moraes, Jhonathan Rosa de Souza, and Pedro Tendrih Sodré who started as just colleagues but became close friends. We had a blast during many gatherings and had numerous interesting discussions on a myriad of topics and you also served as a healing balm during the countless situations that made me consider giving up. I hope I could be such a good friend to you as well.

Furthermore, I would like to thank professors Paula Homem de Melo, Maurício Domingues Coutinho Neto, Cédric Rocha Leão, Thiago Branquinho de Queiroz, Jorge Diego Marconi, Flávio Leandro de Souza, Gustavo Martini Dalpian, and Fernando Luis da Silva Semião for letting me attend your classes and receive a little bit of your knowledge, this helped me grasp a tad bit of the mind-boggling conundrum that pervades the realm of materials simulation.

I also think highly of the “Condensed matter group” which organized many seminars where I was able to get to know many different research topics.

I would also like to thank my amazing family for the love and also for tolerating the many discussions I brought up about physics and chemistry when you actually had no interest and just wanted me to shut up.

Finally, I would like to dedicate this thesis to my mother Miriam Leiko Tayamiti, who created the initial spark of interest in science in me. You still teach me constantly, even though I am a bit more reluctant nowadays.

“God made the bulk; the surface was invented by the devil.”

Wolfgang Pauli

Resumo

O comportamento da água nas superfícies metálicas é importante tanto do ponto de vista teórico quanto prático. O primeiro, porque o entendimento dos detalhes microscópicos dos processos eletroquímicos associados é necessário para melhorar esse campo de pesquisa. O segundo devido ao fato de ter um papel fundamental em muitas aplicações na eletroquímica, por exemplo, em dispositivos de conversão e armazenamento de energia, em corrosão e em catálise heterogênea. No entanto, as caracterizações experimentais da interface metal/água até o momento são complexas e limitadas, levando a muitos aspectos nebulosos. Nesse sentido, simulações atomísticas podem complementar o quadro nanoscópico desse sistema, validando e prevendo dados empíricos e também auxiliando na sua interpretação. A abordagem ideal seria realizar uma simulação de dinâmica molecular totalmente *ab initio* para descrever com precisão as propriedades estruturais e dinâmicas da interface. No entanto, isso é computacionalmente muito caro. Portanto, os protótipos geralmente têm modelos restritos em termos de tamanho e tempo. Uma alternativa para contornar esse obstáculo é realizar um protocolo computacional híbrido do tipo QM/MM. Nesta estrutura, uma abordagem em multi escala para as interações entre água e metal pode ser implementada, com métodos de mecânica quântica fornecendo a reatividade da superfície em simulações em larga escala. Por meio desse método, a interface de ouro e água, influenciada pelos efeitos de polarização do metal devido à presença de água, foi analisada com o objetivo de desenvolver um campo de força, capaz de incluir a polarização, para descrever de forma acurada essa interface.

Palavras-chave: interfaces heterogêneas, DFT, mecânica molecular

Abstract

The behavior of water at metal surfaces is important both from theoretical and practical points of view. The former because the understanding of the microscopic details of the associated electrochemical processes is necessary to improve this field. The latter due to the fact it has a key role in many applications of electrochemistry, e.g. in energy conversion and storage devices, corrosion and heterogeneous catalysis. Yet, experimental characterizations of the metal/aqueous interface have had many setbacks, leading to many unclear aspects. In this regard, atomistic simulations can complement the nanoscopic picture of this system, validating and predicting empirical data and also assisting in their interpretation. The best-case scenario would be performing a full *ab initio* molecular dynamics simulation to accurately describe the structural and dynamic properties of the interface. However, this is computationally too expensive. Hence the usual prototype systems have models restricted in terms of size and time. An alternative to bypass this hindrance is to carry out a hybrid QM/MM computational protocol. In this framework, a multi-scale approach to the water and metal interactions can be implemented, with quantum mechanics methods providing the reactivity of the surface in large scale simulations. By means of this method the interface of gold and water, influenced by the polarization effects of the metal due to the presence of water, was analyzed in the interest of developing a reliable force field capable to include the polarization, to describe this water/metal interface.

Keywords: Heterogeneous interfaces, DFT, molecular mechanics

List of Figures

1.1	Spatial and temporal scales limitations of simulation and modeling methods.	23
2.1	Diagram the steps of a computational protocol to develop a force field for water/metal interface, capable to account the polarization effects of the system.	25
2.2	Schematic representation of the corollary of Hohenberg-Kohn First Theorem.	26
2.3	Scheme comparing many-body approach and DFT.	27
2.4	Scheme comparing pseudo-potential vs all electron wave-functions potentials.	30
2.5	Outline of the rod model. Gold's core are represented by yellow spheres, while the charged virtual sites are depicted by the grey sphere. For visualization of the structures the softwares Visual Molecular Dynamics (VMD), ⁸⁶ (X-Window) Crystalline Structures and Densities (XCrySDen) ⁸⁷ and Avogadro ⁸⁸ were employed during this work.	33
2.6	Illustration of Merz-Singh-Kollman scheme for a water molecule.	34
2.7	Lennard-Jones potential $U(r)$, and internal force $F(r)$. Adapted from Damasceno <i>et al.</i> ⁹⁴	36
3.1	Diagram of the steps of a computational protocol to develop a force field for water/metal interface, capable to account the polarization effects of the system. Focus on the first step: Geometry optimization.	39
3.2	Diagram of a geometry optimization procedure, by means of a CG scheme embedded with an electronic structure calculation through DFT method. .	41
3.3	Framework of DFT's self consistent procedure, with indication of the approximations and the restrictions employed. Besides a brief description of the analytical form of some of its steps.	41

3.4	Diagram the steps of a computational protocol to develop a force field for water/metal interface, capable to account the polarization effects of the system. Focus on the second step: Computing the electrostatic potential. .	42
3.5	Fluxogram of the steps of the QM/MM procedure, with the analytical formulas of the computed parameters at each step, according to Sanz-Navarro's ⁸⁰ and Crespo's ⁸¹ articles.	43
3.6	Illustration of the QM/MM components. In this case is an additive scheme, without mechanical coupling. The water molecule is represented by the TIP3P model and accounted for the MM part of the system. The electrostatic potential generated by its classical point charges were applied as an external potential in the QM calculation of the metal slab which accounted for the QM part of the system.	44
3.7	Overview of the virtual sites of the rod model. The yellow spheres stands for metal ions, while the red and gray spheres designate the oxygen and hydrogen atoms and white spheres indicates the virtual charged particles of the rod model, respectively.	45
3.8	Overview of the supercell system, consisted of a 3x2 pattern grid of replicas of the QM unit cell, applied in the classical molecular dynamic simulation in order to retrieve the average behavior of the rods.	47
3.9	Diagram the steps of a computational protocol to develop a force field for water/metal interface, capable to account the polarization effects of the system. Focus on the third step: Fitting of Charges.	49
3.10	Diagram the steps of a computational protocol to develop a force field for water/metal interface, capable to account the polarization effects of the system. Focus on the forth step: Fitting of Van der Waals parameters. . .	50
4.1	Prototype system used in the geometry optimization scheme, a 4 layers slab of gold with 6 vs 4 atoms per layer and one molecule of water, in an unit cell with 20 Å of vacuum in the slab's non periodical direction. . . .	55
4.2	Illustration from top perspective, of water's adsorption sites at the Au(111) surface. The yellow spheres stands for gold atoms, while the red spheres designate the oxygen atom of the water molecule.	56

4.3	Distances between water molecule and gold atoms in the top layer. Distance δ was applied to check if the water molecule was at atop position, and distance d was applied in the Van der Waals parameters fitting. The yellow spheres stands for gold atoms, while the red and gray spheres designate the oxygen and hydrogen atoms of the water molecule, respectively.	57
4.4	Most energetically stable geometries of the isolated water molecule at a Au(111) metallic surface. On the left there is the flat configuration, with water's dipole moment parallel to the slab's surface, on the middle there is the up configuration with the water's dipole moment perpendicular to the slab's surface and pointing away from surface and on the right theres the flat-down configuration with the water's dipole moment pointing towards the slab's surface in a slanted/oblique direction.	57
4.5	Illustration of the binding angle α between water and the gold surface, applied to identify if the water molecule was in the flat, down, up or flat-down configuration.	58
4.6	Plot of the nanosmoothed averages, of the electrostatic potentials without external field (No-ext) and the neutral atom electrostatic potential, in the z direction (slab's non periodical direction) in order to compute the VNA Shift.	60
4.7	Top view of the average behaviour of the rods for each layer of the slab. In the yellow/gray spheres, yellow stands for gold atoms while the gray portion indicates the virtual sites representing the charged particles of the rod model. The red and white spheres designate the oxygen and hydrogen atoms of the water molecule, respectively.	61
4.8	Side view of the average behaviour of the rods. In the yellow/gray spheres, yellow stands for gold atoms while the gray portion indicates the virtual sites representing the charged particles of the rod model. The red and white spheres designate the oxygen and hydrogen atoms of the water molecule, respectively.	61
4.9	Perspective view of the average behaviour of the rods, with indication of the relevant sites.	62

4.10	Comparison between QM/MM (left), and RESP-Free (right, all charges were fitted) potential. The blue and red colors represent the most negative and most positive values of electrostatic potential.	64
4.11	Comparison between QM/MM (left) and RESP-M0free (right, charges of the relevant site were fitted while charges of other sites were set to be zero) potential. The blue and red colors represent the most negative and most positive values of electrostatic potential.	64
4.12	Comparison between QM/MM (left) and RESP-M0Same (right, charges of the relevant site were equal while charges of other sites were set to be zero) potential. The blue and red colors represent the most negative and most positive values of electrostatic potential.	65
4.13	Comparison between QM/MM (left) and RESP-Same (right, charges of the relevant site were equal while the charges at other sites were fitted) potential. The blue and red colors represent the most negative and most positive values of electrostatic potential.	65
4.14	QM/MM electrostatic potential. The blue and red colors represent the most negative and most positive values of electrostatic potential.	66
4.15	Charges from the RESP fitting of the QM electrostatic potential, for each of the fifteen relevant sites, in each set of restrictions, in the Image 5. . . .	69
4.16	Distances between each atom from the water molecule in the flat configuration and the seven nearest gold atoms. On the left the focus is the oxygen, in the middle is one of the hydrogen labeled as Hydrogen 1 and on the right is the other hydrogen labeled as Hydrogen 2.	70
4.17	Distances between each atom from the water molecule in the flat-down configuration and the seven nearest gold atoms. On the left the focus is the oxygen, in the middle is one of the hydrogen labeled as Hydrogen 1 and on the right is the other hydrogen labeled as Hydrogen 2.	70
4.18	Distances between each atom from the water molecule in the flat configuration and the seven nearest gold atoms. On the left the focus is the oxygen, in the middle is one of the hydrogen labeled as Hydrogen 1 and on the right is the other hydrogen labeled as Hydrogen 2.	71

4.19	Assessment of the range of the Lennard Jones parameters with water at the flat configuration.	72
4.20	Assessment of the range of the Lennard Jones parameters with water at the flat configuration.	73
6.1	Plot of total energies vs cell volume fitted to a Murnaghan equation of state in order to evaluate Au lattice constant.	94
6.2	Comparison between determined lattice constant of gold. Dots represents values obtained using different functionals (LDA, SOGGA, WC, PBEsol, AM05, TPSS and PBE) reported by Haas et al. ¹²⁸ and experimental values reported by Haas et al. ¹²⁸ (Exp1) and by Patel ¹¹⁶ (Exp2). Dashed lines indicates the values calculated in this work using PBE functional. . .	95
6.3	Comparison between determined lattice constant of gold. Dots represents values obtained using Hartree-Fock and experimental value reported by Haas et al. ¹²⁸ and also a value from empirical electron theory. Dashed lines indicates the values calculated in this work using PBE functional. . .	95
6.4	Comparison between determined lattice constant of gold. Dots represents values obtained using different functionals (LDA, SOGGA, WC, PBEsol, AM05, TPSS and PBE) reported by Haas et al. ¹²⁸ and experimental values reported by Haas et al. ¹²⁸ (Exp1) and by Patel ¹¹⁶ (Exp2). Dashed lines indicates the values calculated in this work using PBE functional. . .	96
6.5	Determined work function of gold. Dots represents values using different functionals reported by Huzayyin ⁸ and experimental values reported by Hansson. ¹¹⁷	98
6.6	Assessment of the range of the Lennard Jones parameters with water at the flat-down configuration.	106
6.7	Assessment of the range of the Lennard Jones parameters with water at the up configuration.	106

List of Tables

4.1	Properties of the gold slab. Comparing with experimental values reported by Patel ¹¹⁶ (lattice constant) and by Hansson ¹¹⁷ (work function).	54
4.2	Properties of the water molecule. Comparing with experimental data reported by Benedict <i>et al</i> (water’s internal angle and O-H distances) and ¹²¹ and Clough <i>et al</i> ¹²² (dipole moment).	54
4.3	Adsorption energies for each configuration of water molecule related to the metal surface, with and without BSSE error correction.	59
4.4	Description of the average lengths l of the rods of the selected sites and the indexes of their correspondent metal. The l s were computed in CPPTRAJ after a 600 ps classical molecular dynamics simulation in the NVT emsemble. These rods were selected by fulfilling the criteria that this l s were larger or equal than 0.05 Å and also that the virtual sites were associated with metal atoms belonging to the top two layers.	63
4.5	Statistics of RESP fitting. Showing the root-mean-square error and the relative root-mean-square error for each image in each set of restrictions applied in the RESP procedure.	67
4.6	Average RESP charges of each layer of the slab for the set “Free”.	68
4.7	Average RESP charges of each layer of the slab for the set “Same”.	69
4.8	Distances between each atom from the water molecule and the seven nearest gold atoms, considering the up, the flat-down and the up configurations.	71
4.9	Relations between ϵ_H and ϵ_O for each configuration.	71
4.10	Lennard-Jones parameters for each configuration.	72
6.1	Cutoff radius of each “zeta” representing the radial part of the atomic orbitals of gold atoms.	91

6.2	Cutoff radius of each “zeta” representing the radial part of the atomic orbitals of oxygen atoms.	92
6.3	Cutoff radius of each “zeta” representing the radial part of the atomic orbitals of hydrogen atoms.	92
6.4	Properties of water TIP3P model.	98
6.5	Charges from the RESP fitting, for each of the fifteen relevant sites, in each set of restrictions, in Images 1 and 2.	100
6.6	Charges from the RESP fitting, for each of the fifteen relevant sites, in each set of restrictions, in Images 3 and 4.	101
6.7	Charges from the RESP fitting, for each of the fifteen relevant sites, in each set of restrictions, in Images 6 and 7.	102
6.8	Charges from the RESP fitting, for each of the fifteen relevant sites, in each set of restrictions, in Images 8 and 9.	103

Contents

1	INTRODUCTION	21
2	THEORETICAL BACKGROUND	25
2.1	Density Functional Theory	26
2.1.1	The Kohn-Sham Method	27
2.1.2	Exchange-correlation functionals	28
2.1.3	Pseudo-potentials	29
2.2	Quantum Mechanics/Molecular Mechanics approach	31
2.3	Rod model	32
2.4	Merz-Singh-Kollman (MK) model	33
2.5	Restrained Electrostatic Potential (RESP)	35
2.6	Non-bonded Lennard-Jones parameters	35
3	PARAMETRIZATION PROTOCOL	39
3.1	Reference geometry calculation procedure	40
3.2	Electrostatic potential	42
3.3	Rod model	45
3.4	Molecular dynamics	46
3.5	RESP	48
3.6	Van der Waals interaction	50
4	RESULTS	53
4.1	System	53
4.2	Selected sites	60
4.3	RESP	63
4.4	Adjustment of Van der Waals parameters	70

5	CONCLUSIONS AND PERSPECTIVES	75
6	SUPPLEMENTARY INFORMATION	91
6.1	Localized basis set description	91
6.2	Pseudo-potential	92
6.2.1	Pseudo-potential description	93
6.3	Results - Slab properties	93
6.3.1	Lattice Parameter	93
6.3.2	Bulk Modulus	96
6.3.3	Cohesive Energy	97
6.3.4	Work Function	97
6.3.5	Water TIP3P	98
6.3.6	Charges	99
6.3.7	Lennard Jonnes parameters	105

Chapter 1

INTRODUCTION

Much effort has been spent over the years on world's trend to pursue eco-friendly and efficient ways to harvest the environment resources. As for the energetic issue, several alternatives are based on development of electrochemical devices such as photovoltaic cells, fuels cells and batteries.¹⁻³ Since most often the physico-chemical processes related to electrochemistry takes place at interfaces,^{4,5} for a comprehensive understanding of associated mechanisms, e.g by which the energetic barriers can be tuned,^{6,7} surface science and interfacial analysis are of the utmost importance in future endeavors to identify and design new electrodes and catalysts.⁸

An extensive literature on electrochemistry and catalytic process was established in the past century.⁹⁻¹³ Initially, focusing in macroscopic behaviour like current-voltage characteristic.^{14,15} Latter, as the relationships between structure and performance became more evident, was honed in chemisorption and physisorption of single atoms or ions, small clusters and molecules on surfaces.¹ In particular, the behavior of water at metal surfaces has motivated many studies,¹⁶⁻¹⁸ since it plays a significant role in electrochemistry (e.g. the above mentioned electrochemical energy storage devices and photovoltaic cells), corrosion studies^{19,20} and heterogeneous catalysis.²¹⁻²³ Alas, comprehensive knowledge on water molecules lodged in the interface is still lacking.^{21,24} Preferred binding site and orientation of water monomers are a case in point,²⁵ these factors, for instance, affect how the system react to an applied electric field or how water may dissociates at surfaces in a water-splitting apparatus for hydrogen production.²⁶

From the theoretical point of view, understanding at a microscopic level how liquid water interacts with metal surfaces is feasible, but not yet a simple task. In this context, computational simulation is an efficient tool to predict/validate and interpret the empirical data.²⁷ The rationale of this approach has been described, among many references, by

Thiel and Madey²⁸ and latter by Henderson.²⁹

In this regard, the hereafter addressing topic is concerned with the capabilities of the computational simulations. A thorough description of the system would require accurate modelling of the electronic effects such as dispersion and polarization of a large region and it's dynamics for long time periods. Since the setting includes a region with periodic pattern (i.e. the slab) filled with delocalized valence electrons, and in counterpart an adjacent region with strong local polarization effects,³⁰ there are many intricacies associated with the description of the non bonded interactions (electrostatic and the Van der Waals) between the atoms in water molecule and the gold atoms. Full *ab initio* molecular dynamic calculations could circumvent these limitations, however, it is computationally too expensive.

Focusing solely in the computational restriction, an alternative would be to perform a full classical molecular dynamics simulations, since they have lower computational cost and could be done for large systems and long time periods. Yet, this approach would imply in the neglect of electronic structure effects,³¹ that is, the model would not be able to reproduce the quantum behaviour of atoms in the interface water-metal. For instance, most classical molecular dynamic force-field models do not account for the polarization of the metal due to the interaction with the water, which is observed when a quantum chemical calculation is performed. They consider only the electrostatic charges. As a consequence, the preferential adsorption site and the most energetically favourable configuration for the orientation of the water's dipole moment vector related to the metal surface are wrong. For example, applying the potential designed for interfaces called INTERFACE³² the water molecule does not stabilize above an atom of gold (top position) as reported in the literature.⁸ Other potentials correct this problem of adsorption site, by adding Gaussian potentials at the metal atoms or by introducing virtual sites, located at the region between the atoms (hollow sites) of the outermost metal layer, with potentials like Lennard Jones and/or Gaussian,³³ but these methods still are not capable of identifying the correct minimum configuration, that should be with the dipole moment parallel to the surface (flat configuration) or lack the ability to compute the accurate magnitude of the energy difference between top and hollow sites. Therefore, a satisfactory parametrization of the interactions in this system through this approach is hitherto unknown.

In this context, an interesting alternative to simultaneously tackle the different above mentioned restrictions and achieve a comprehensive understanding of the associated phenomena at this interface, is to implement a hybrid computational protocol of the Quantum Mechanics Molecular Mechanics (QM/MM) type. With this strategy one is capable of adequately describe this system and also have an affordable balance between accuracy and feasibility. QM/MM tactic relies on the fact that in the study of reactivity of some chemical species, although the quantum description of the interactions is critical, in most cases the surrounding environment can be modeled by just classical force fields.³⁴⁻³⁶ A typical example is the enzymatic catalysis where an active site of a protein is relatively small compared to the whole supra-molecular assembly, therefore an atomistic description of interaction can be implemented only at the active site and for the rest a classical molecular dynamic approach can be applied.³⁷

As shown in Figure 1.1, the hybrid QM/MM framework allows an accurate and consistent treatment of information, such as the reactivity of the metal surface, calculated in a quantum method, to be replicated and processed by classical methods³⁸ in a multiscale approach. So, accurate properties from quantum methods are broadened to reach longer time and larger size scales.

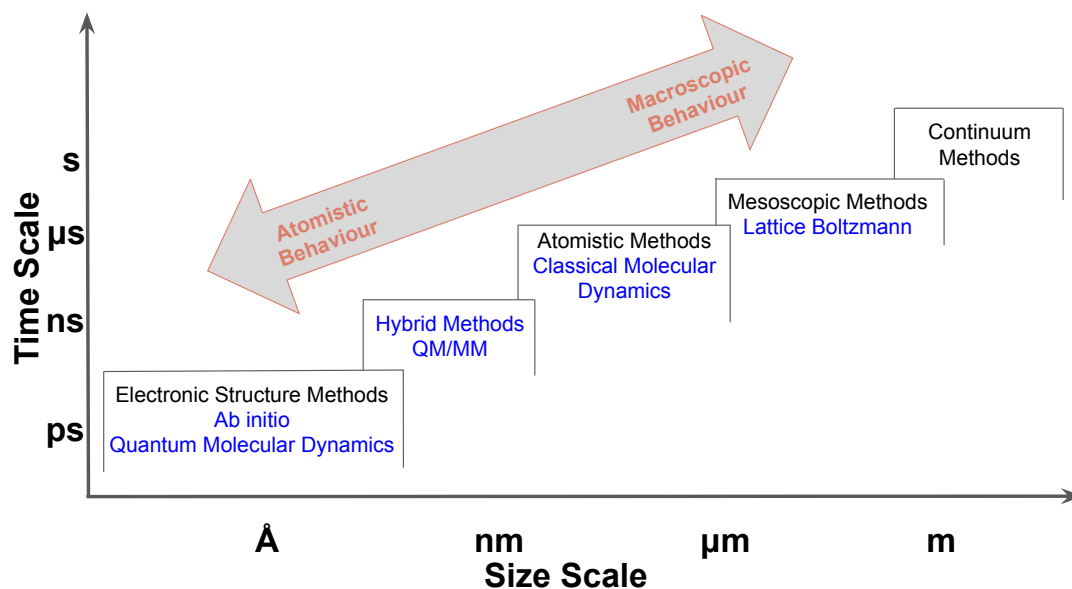


Figure 1.1: Spatial and temporal scales limitations of simulation and modeling methods.

In the QM/MM approach the quantum mechanics part can be carried out using Density Functional Theory (DFT).^{39,40} Currently, it is the main technique for simulations in chemistry and in physics, due to the computational cost-benefit ratio's equivalent, accuracy and computational time.⁴¹ This theory can provide many information

of the electronic structure of the system, allowing a microscopic characterization/modelling that can complement experimental works.⁴² Yet one should bear in mind that many phenomena which are of paramount importance for technological advance still lack deeper analysis (through simulations) due to restrictions of computational power and limitations associated with the many approximations used (e.g Born–Oppenheimer (BO), norm-conserving pseudopotentials, exchange-correlation functional, etc).^{43–45} For instance, DFT is bounded by the applied functional and it is well established that the LDA/GGA approximations can not provide a proper description of the asymptotic decreasing behavior of the long-range Van der Waals (vdW) interactions, which has motivated a large number of theoretical studies.^{24, 46–48}

In this scenario, the main goal of this research was to parametrize a reliable force-field (an analytical formula) model for water/metal interaction capable of including the polarization effects at the interface. In order to achieve this objective, two sets of parameters were analyzed, the electrostatics (which accounted for the polarization of the slab) and the Van der Waals. Towards the first set, charges of the metal atoms were computed, through a fitting method with restrains (the RESP method), so that they reproduce the electrostatic potential obtained through a quantum mechanical calculation (in this case DFT as previously mentioned) on the most stable configuration of the system. Towards the second set, the parameters of a Lennard Jones potential were adjusted for the metal/oxygen and the metal/hydrogen interactions.

This work is organized as follows: In chapter 2, the theoretical background relevant to the implemented QM/MM approach is reviewed. A short introduction is first given for DFT, which is the starting point for calculations, then for the inherent approximations of this approach (like exchange-correlation functional and pseudo-potentials). Next, the theory associated with the following procedures of the protocol (such as the implementation of the rod model to account for the polarization, the selection of relevant fitting sites through a Merz-Singh-Kollman-like scheme followed by the Restrained Electrostatic Potential method and the fitting of Van der Waals parameters) is outlined. In chapter 3, the details of the implementation of the protocol done so far are explained. Then, results are reported in chapter 4. Afterward conclusions concerning this work and an outlook for future research are summarized in chapter 5. Lastly, supplementary material can be found at chapter 6.

Chapter 2

THEORETICAL BACKGROUND

As pointed out in the introduction, the main goal of this work is to accurately describe the interaction between water and gold. For this purpose the resulting model should account for the electronic effects and the long-range Coulomb forces. Towards this objective, a protocol with a hybrid QM/MM scheme was developed. Through this method, the depiction of electronic degrees of freedom was attained through a quantum mechanical method and a classical mechanics force field able to mimic the induced polarization of the metal was established.

In this chapter, there is a review of the theoretical background underlying the work of this research. The structure by which sections will be addressed follows the framework of the methodology that is outlined in the flowchart, see Figure 2.1:

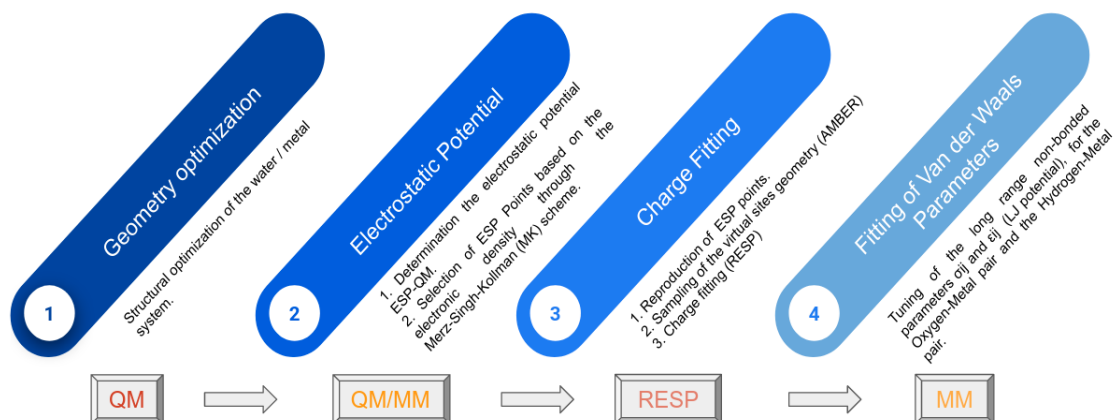


Figure 2.1: Diagram the steps of a computational protocol to develop a force field for water/metal interface, capable to account the polarization effects of the system.

In order to approach the adsorption phenomena, a simplification in the model was made by selecting the most energetically stable structure arrangement. From the energetic aspect, this is a reasonable approximation since the difference between the minimum

energies of each configuration (that is, the geometries of the isolated water molecule adsorbed at the metal surface) is very small, as will be shown latter.

Towards identifying these most energetically stable geometries (local minima on the potential energy surface), an optimization procedure (denoted as structural relaxation) was performed. In order to carry out this procedure an electronic structure calculation is required.

The chosen framework in this work so as to attain the aforementioned electronic structure, was the Density Functional Theory (DFT). It has been the work horse to tackle many-body systems, and it's concepts are abridged in the following sections.

2.1 Density Functional Theory

A comprehensive overview of Density Functional Theory is beyond the scope of this dissertation. Excellent reviews on these subjects are readily found in the literature, e.g. “The Chemist’s Guide to DFT”,⁴⁹ Parr and Yang’s textbook⁵⁰ and Capelle’s article.⁵¹ Here only the central aspects of the theory will be briefly summarized.

Density Functional Theory (DFT) is a technique applied for theoretical investigation of the properties of multi-electronic systems. A priori DFT has two aspects. One that comes directly from two theorems proved by Pierre Hohenberg and Walter Kohn in the article published in 1964.³⁹ And another, that comes from the implementation of approximations to the corollaries conveyed in the former, and which has been developed since the article published by Walter Kohn and Liu Sham in 1965.

The first aspect, depicts DFT as an exact theory. Inspired by the approach suggested by Thomas and Enrico Fermi in 1927, the question if the electronic density “completely” describe the system, led to the formulation of the first theorem’s ansatz, about the existence of a unique mapping, besides an uninteresting additive constant, between the ground state density $\rho_0(\mathbf{r})$ of a many-body electronic system and the external potential ν_{ext} , see Figure 2.2, and by extension with the energy of the system.

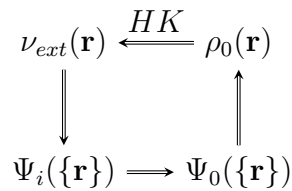


Figure 2.2: Schematic representation of the corollary of Hohenberg-Kohn First Theorem.

Where $\nu_{ext}(\mathbf{r})$ is the external potential, $\Psi_i(\{\mathbf{r}\})$ and $\Psi_0(\{\mathbf{r}\})$ are the wavefunction in

an arbitrary state and in the ground state, respectively and HK stands for the Hohenberg-Kohn theorem.

As mentioned, the second aspect sets DFT closer to a set of approximations. The most popular implementation of these assumptions is the Kohn-Sham method by which a self-consistent framework is applied for the determination of the electronic structure of solids and molecules. This method is described in the next section.

2.1.1 The Kohn-Sham Method

Shortly after Schrödinger equation was formulated, Llewellyn Thomas and Enrico Fermi, formulated a scheme to solve the electronic structure of many-body system also focusing in the electronic density, yet this model had a major downside, it suggested a bad approximation to describe the unknown kinetic energy term, yielding poor results that led to the abandon of this model.⁵²

Based in the example of Thomas Fermi model, Walter Kohn and Lu Jeu Sham realized that the keystone to improve the accuracy of a density based method was the description of the kinetic energy.

The scope of Kohn-Sham method is based on the hypothesis that for any system with interacting particles with exact ground state density $\rho(\mathbf{r})$, there is a fictitious local mo-noelectronic potential $\nu(\mathbf{r})$ with a real density of non-homogeneous electron gas $\rho_{KS}(\mathbf{r})$ ⁵³ with the same value, see Figure 2.3.

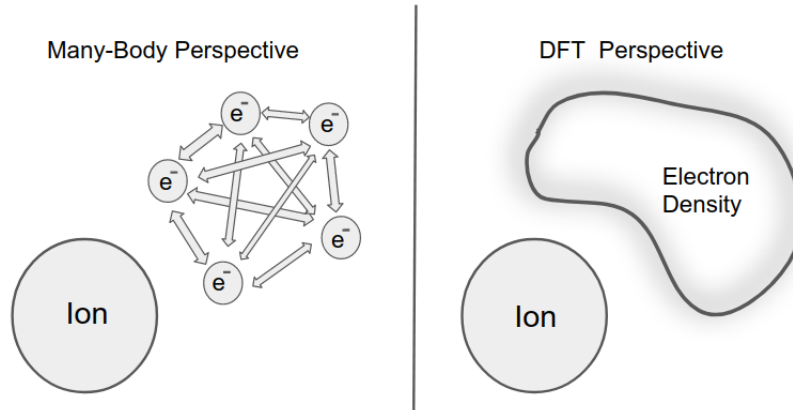


Figure 2.3: Scheme comparing many-body approach and DFT.

Therefore the Kohn-Sham approach deals with equations analogous to the Schrödinger equation, with a one-electron orbitals (KS orbitals) as solutions, see Equation 2.1:⁴⁰

$$\left(\frac{-\hbar^2 \nabla^2}{2m} + \nu(\mathbf{r}) + \nu_H(\mathbf{r}) + \nu_{xc}[\rho(\mathbf{r})] \right) \phi_i(\mathbf{r}) = E_i \phi_i(\mathbf{r}) \quad (2.1)$$

Where ϕ_i are the Kohn-Sham orbitals, E_i are the Kohn-Sham eigenenergies, ν is the external potential, ν_H is the Hartree potential and ν_{xc} is the exchange correlation

potential. The system of equations is self-consistently solved from an initial guess of a density.

An important advantage of this approach is that the many-body problem at the ground-state level can be efficiently replaced by an effective one-body problem. This, in general, allows DFT calculations to be performed with a much lower computational cost in comparison to wave-function methods and still have good accuracy in many results.

Considering the trade-off computational time/cost vs accuracy, it is one of the best approaches nowadays, therefore it is largely used in the fields of physics, chemistry and condensed matter subjects.

In the next sections there is a brief description of simplest functionals implemented in the Kohn-Sham scheme, the Local Density Approximation (LDA) and Generalized Gradient Approximation (GGA). Yet there are many other, like meta-GGA, hybrids and so on so forth.

2.1.2 Exchange-correlation functionals

In the Kohn-Sham approach the ground-state energy is written as

$$E[\rho] = T_s[\rho] + \int d^3r \rho(\mathbf{r}) \nu(\mathbf{r}) + \frac{1}{2} \int \int d^3r d^3r' \frac{\rho(\mathbf{r})\rho(\mathbf{r}')}{|\mathbf{r} - \mathbf{r}'|} + E_{xc}[\rho] \quad (2.2)$$

Where T_s stands for the kinetic energy of the independent particles, the second term is the contribution of the external potential, the third term represents the classical Coulomb interaction energy for the electron density with itself (the Hartree energy), and the E_{xc} is the exchange-correlation energy functional, which account for all the many-body effects of the electron-electron interactions.

The ansatz proposed by Kohn and Sham in 1965 was to take $\epsilon_{xc}(\rho)$ (exchange-correlation energy per particle) to be the exchange and correlation energy density of the uniform electron gas of density ρ , this is the Local Density Approximation.⁴⁰ Within the LDA $\epsilon_{xc}(\rho)$ is a function of only the local value of the density. Usually LDA overestimates the exchange energy (E_x) but underestimates the correlation energy (E_c), for metals this leads to good values of E_{xc} due to systematic error cancellation,⁵⁴ and as a result this approach described reliably properties such as structure, vibrational frequencies, elastic moduli and phase stability of solids. Hence it was implemented for a long time in solid state investigations.⁵⁵

Functionals beyond LDA have corrections for the variation of density according to the position, this can be obtained by including the gradient of the densities in the energy

integral in Equation 2.3:

$$E_{xc}^{GGA}[\rho] = \int f(\rho(\mathbf{r}), \nabla\rho(\mathbf{r}))d\mathbf{r} \quad (2.3)$$

Where $E_{xc}^{GGA}[\rho]$ is the exchange and correlation energy in the GGA framework, $\rho(\mathbf{r})$ and $\nabla\rho(\mathbf{r})$ are the electronic density and its derivative, respectively and f is a parametrized analytic function. The consequence is that these are non-local approximations.

Just coupling the gradient produces many nonphysical properties and in some cases the results are worse than those obtained with LDA. An improvement from this approach is to impose some restrictions. Then this became what is called the Generalized Gradient Approximation (GGA).⁵⁶ In this work a functional of GGA approach was chosen, the nonempirical Perdew, Burke and Ernzerhof (PBE) functional. A meticulous discussion of the physical ideas used to construct the PBE and the consequences for practical calculations is given in the 1997/1998 articles from these authors with Ales Zupan.^{57,58} PBE presented reliable results describing hydrogen bonds in ice^{59,60} and also accurate data for metal.⁶¹ These results motivated many attempts to describe interfaces between water and transition metals^{2,23,24,62-64} which also yielded interesting results.

Yet, a general drawback of all common GGA functionals, including hybrids, that replace part of the local by nonlocal Hartree-Fock exchange, is that they can not describe long-range electron correlations that are responsible for Van der Waals.^{41,47,48,65,66}

Another approximation usually implemented in the framework of DFT is the pseudo-potential, this will be discussed in the next section.

2.1.3 Pseudo-potentials

Electrons in the innermost region of the atoms, such as the core electrons, are tightly bound to the nuclei, i.e. have large binding energy values.⁶⁷ Besides, they are highly localized,⁶⁸ their spatial distribution remains essentially unchanged from one chemical environment to another and perturbations (e.g. excitation by low energy radiation or interaction with neighbouring atoms) will not affect them as intensely as valence electrons. This highly localized aspect of the core electrons render expansions of the core wavefunctions inefficient, due to the large number of terms (e.g. plane wave) required in the summation to describe this pattern.

In addition, in quantum mechanics investigations, the increase of the number of the atoms in the system can rapidly become a major impediment, especially if one carries

out calculations with all electrons. This is due to fact that more basis coefficients and interactions should be considered, therefore the computational effort turns too costly.

A compelling alternative to circumvent these hindrances is to replace the influence of core states on the valence electrons by an effective potential, namely a pseudo-potential.⁶⁹ In this approximation, first introduced by Hans Hellmann in 1934,⁷⁰ the set of pseudo wavefunctions representing the valence electrons have fewer nodes inside core regions, see Figure 2.4, and the effective potential can be represented with just a few Fourier coefficients so a substantial computational saving is possible.^{71,72}

There are two major characteristics desirable for pseudo-potentials, transferability⁷³ and softness.⁷⁴ In essence, the first means that if one changes the chemical environment of the system there will be no loss of information. Pseudo-potentials are developed for isolated atom, yet, in the case of this atom interacting with another, e.g. gold in gold clusters or in gold surfaces with oxygen adsorbed in, the pseudo-potential should accurately reproduce realistic features, describing well until the core radius. The second means a correlation between increasing the wave-function expansion and a fast convergence of calculated properties. Usually soft pseudo-potentials requires a small number of Fourier components for its accurate representation.

In electronic structure codes, two classes of pseudo-potentials are widely employed⁷⁵ the norm-conserving type and the ultrasoft type.⁷⁶ The norm-conserving approach, was initially proposed by Hamann, Schülter, and Chiang (HSC) in 1979.⁷⁷ This framework have two necessary conditions: First, up until the cut-off radius r_c , see Figure 2.4, the norm of each pseudo-wavefunction need to be equal to its corresponding all-electron wavefunction. And second, outside cut-off radius r_c both all-electron and pseudo-wavefunctions have to be identical.^{75,78}

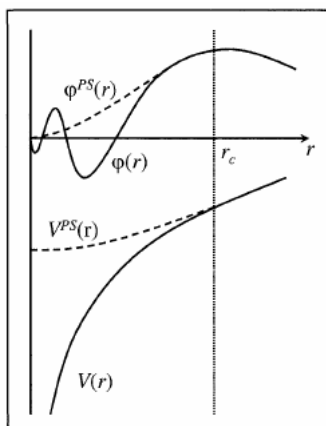


Figure 2.4: Scheme comparing pseudo-potential vs all electron wave-functions potentials.

A norm-conserving pseudo-potential was applied in this work, specifically the Troullier-Martin form.⁷⁹

An efficient method to parametrize a classical model accounting the quantum effects in the system, is to implement a hybrid approach, this will be presented in the next section.

2.2 Quantum Mechanics/Molecular Mechanics approach

The simulation of realistic models requires time and spatial scales that are too demanding in terms of computational effort for one to apply only QM methods, thus a hybrid Quantum Mechanics/Molecular Mechanics approach was used.

Like the DFT's theoretical background, a comprehensive overview of QM/MM theory is beyond the scope of this dissertation. The methodology of the QM/MM procedure used in this work is described in depth in the Sanz-Navarro's article⁸⁰ based in Crespo's article.⁸¹ Only the gist of these papers will be summarized in this section.

Hybrid Quantum Mechanics/Molecular Mechanics (QM/MM) methods were initially applied by Warshel and Levitt in 1976³⁷ to study enzymatic processes. This work lead them to be awarded the Nobel Prize for Chemistry in 2013.⁸² After this seminal research many other QM/MM models have been developed, with different approaches to the partitioning of the system and handling of the coupling terms of the Hamiltonians.

The ingenious idea of Warshel and Levitt was spatially split the system into two interacting parts treated at different levels of theory. The starting premise of QM/MM methods is to treat the region of the system which undergoes the crucial electronic changes using a quantum mechanical method like DFT, coupled cluster (CC) or full configuration interaction (full CI), whilst the rest is modelled using molecular mechanics force-fields.³⁵

There are many issues related to the coupling. For instance, if the scheme is additive or subtractive. In this work, an additive method was chosen, which made possible to divide the code in a modular way and the total energy of the combined system is given by Equation 2.4:

$$E_{tot} = E_{QM} + E_{MM} + E_{QM/MM} \quad (2.4)$$

Where E_{QM} represents the internal Kohn–Sham energy of the quantum subsystem. E_{MM} , stands for two-, three- and four-body bonded interactions, as well as the non-bonded terms such as Van der Waals and Coulomb interactions between classical atoms. The last term

of Equation 2.4, $E_{QM/MM}$, is the mixed interaction between the QM and MM regions. It only contains non bonded interactions between the classical and quantum atoms.

An approach to reproduce the polarizability of the metal slab is to employ the Rod model.⁸³ This model will be described in the next section.

2.3 Rod model

The charge density of a molecule closed to the metallic surface acts as an electric field that induce polarization effects at the electrode surface. The accurate description of this phenomena is complex since these effects are of the same order of intensity as inter-molecular bonds, and have remarkable impact in the adsorption.⁶³

For instance, in the presence of a molecule of water a mirrored image of the partial charges from that molecule is created in the surface of the metal. Thus, by the electrostatic interaction, the molecules that are closer to the surface will be attracted more intensely than the molecules farther away.⁸⁴ Furthermore, the induced charge on electrode surface also affect the charge distribution of the adsorbed molecule, which by its turn alter the interaction between molecules of adsorbate.⁸⁵

Unfortunately, the usual classical force fields for electrodes based on the constant charge approach do not account for polarization, as a result they lack accurate prediction of dynamic properties. Conversely, polarizable force fields typically includes very complex analytic functions or adjusts the redistribution of charge on-the-fly according to a variational procedure, both complicated approaches that are not compatible to the prevailing force fields.³³

In this work, to overcome this drawback, a polarizable classical force field employing the Rod Model,⁸³ where the induced charge effects is attained by the incorporation of dipoles to the system topology, was developed. In this model, only the contribution of charge image effects, that is non-local electronic effects, to the potential energy surface of an adsorbed molecule or ion is examined.

As above mentioned, in order to obtain induced charge effects, dipoles were added to the system topology. Each dipole was composed by a metallic atomic core, with charge ($q_{metal} = -q$), and a charged virtual site, with same charge intensity as the respective metal atom but with opposite sign so that the system remained neutral, connected by a rigid bond of length l_0 that can freely rotate, see Figure 2.5, thus with dipole moment equals to $\mu = ql_0$.

The rotation dynamics of this permanent dipole instantaneously reproduces the surface polarization.

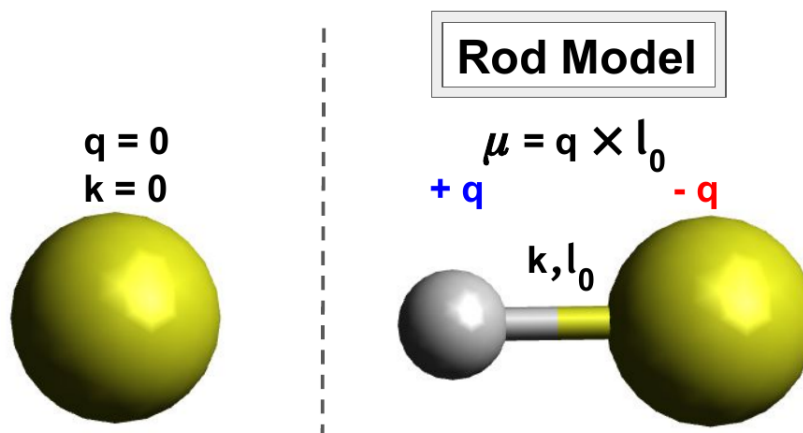


Figure 2.5: Outline of the rod model. Gold’s core are represented by yellow spheres, while the charged virtual sites are depicted by the grey sphere. For visualization of the structures the softwares Visual Molecular Dynamics (VMD),⁸⁶ (X-Window) Crystalline Structures and Densities (XCrySDen)⁸⁷ and Avogadro⁸⁸ were employed during this work.

At this stage, the focus was the description of the electrostatic part of the force field, which has the functional form:

$$E_{FF-Elect} = \frac{1}{4\pi\epsilon_0} \sum_{ij, \text{nbond}} \frac{q_i q_j}{r_{ij}} \quad (2.5)$$

Where q_a are the atomic charges and r_{ab} are the distances between atoms. Later the long range interaction was added by fitting the parameters of Lennard-Jones Potential, σ and ϵ .

Since in this model, each atom of the metal has a permanent dipole, an orientational averaging (i.e., $T > 0$) is necessary to generate physically meaningful results. This was derived through a molecular dynamic simulation.

This was the method to include the polarization, applied to the metal slab.

We were interested in computing the charges that describe the electrostatic part of the force-field, this was achieved through fitting of the QM electrostatic potential, for that matter, a method to partitionate this QM potential and select relevant sites was required, and will be shortly presented in the next section.

2.4 Merz-Singh-Kollman (MK) model

From the electrostatic potential around the metal surface, derived in a previous steps with the hybrid QM/MM scheme, a fitting of charges was performed. So as to identify

the best way to execute this fitting, a set of reference points to be replicated had to be designated. Toward this selection of the most important points, a Merz-Singh-Kollman (MK)^{89,90}-like method was applied.

In the MK method, a sampling of the electrostatic potential at a number of grid points located on several layers around the system is taken into account. The layers are constructed as an overlay of Van der Waals spheres around each atom, see Figure 2.6 for an example with the case of a water molecule. Each layer is obtained by scaling all radii with a factor of 1.4, 1.6, 1.8, and 2.0, respectively.

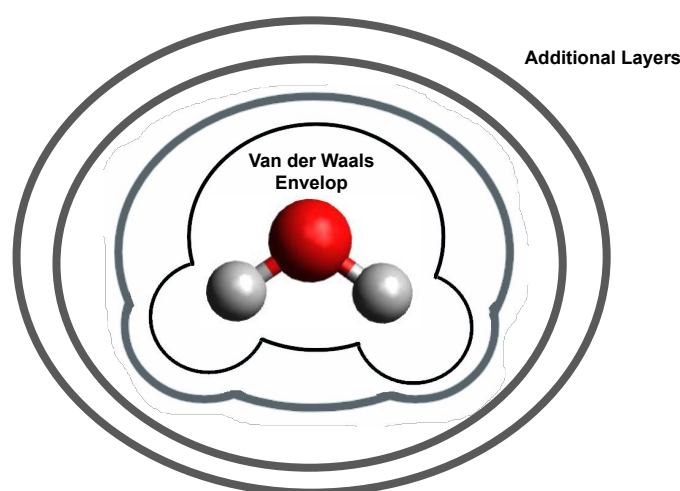


Figure 2.6: Illustration of Merz-Singh-Kollman scheme for a water molecule.

In this setting, ESP points outside the Van der Waals volume of the metal atoms and the ESP points at layers which the potential does not vanish rapidly are appointed.

In this work, the concepts of the Merz-Singh-Kollman method were adapted for the selection of relevant sites. In essence three criteria were enforced:

1. The atoms should belong to the top two layers of the metal slab. The rationale of this constraint is that these layers were expected to exhibit more polarization while the electrostatic effect of the charges of the water atoms were probably attenuated and/or screened for the lower layers.
2. The average length l of the rod of the respective atom, fixated in a minimum energy configuration or in a distribution of the dipoles in a canonical ensemble, attained through a molecular dynamics simulation, should be greater than a certain value. A higher length l , indicates a preferential orientation of the dipoles.
3. The point selection was performed also considering the electronic density (ρ) of the

metallic surface. Considering previously conducted tests, only points inside a range of ρ were chosen. This range reflects the numerical restrictions. The density must not be zero or too small, to avoid noise. In addition, ρ should not be large, this would be analogous to account points located inside the van der Waals volume.

From the electrostatic potential, charges were fitted using the Restrained Electrostatic Potential (RESP)^{91–93} technique. The basic concepts of this method are described in the next section.

2.5 Restrained Electrostatic Potential (RESP)

The Restrained Electrostatic Potential (RESP)^{91–93} method was employed to obtain the set of atomic charges that optimally reproduce the region of inter-molecular interaction of the ESP-QM. That is, a least squares algorithm including a penalty function was implemented to fit the charge q_j to each atomic center j within the selected region of the system.

In the fitting procedure, the calculation of the electrostatic potential \hat{V}_i is carried out using the formula:

$$\hat{V}_i = \sum_j \frac{q_j}{r_{ij}} \quad (2.6)$$

Where r_{ij} designates the distance between each atomic center j and each point i selected by the Merz-Singh-Kollman-like method.

After the partial charges were fitted, the Van der Waals parameters are also adjusted, the concepts the led to the fitting methodology are describe in the next section.

2.6 Non-bonded Lennard-Jones parameters

Following the charge fitting, to reproduce the QM adsorption energy and geometry of the most energetically stable adsorption structure of isolated water, the dispersion interaction at the interface was computed. This was achieved through the fitting of a pair potential, specifically a Lennard-Jones (LJ) potential. In this context, the dispersion part of the force field has the analytical/functional form as in Equation 2.7.

$$E_{FF-LJ} = \sum_{ij, \text{nbond}} \epsilon_O \left[\left(\frac{\sigma_O^*}{r_{ij}} \right)^m - 2 \left(\frac{\sigma_O^*}{r_{ij}} \right)^n \right] + \sum_{ij, \text{nbond}} \epsilon_H \left[\left(\frac{\sigma_H^*}{r_{ij}} \right)^m - 2 \left(\frac{\sigma_H^*}{r_{ij}} \right)^n \right] \quad (2.7)$$

Where the parameters σ^* (the distance at which the inter-particle potential is minimum) and ϵ (the depth of the potential well, that is, the equilibrium nonbond energy), see Figure

2.7, of the long range non-bonded interaction were calculated for the Oxygen-Metal pair and the Hydrogen-Metal pair.

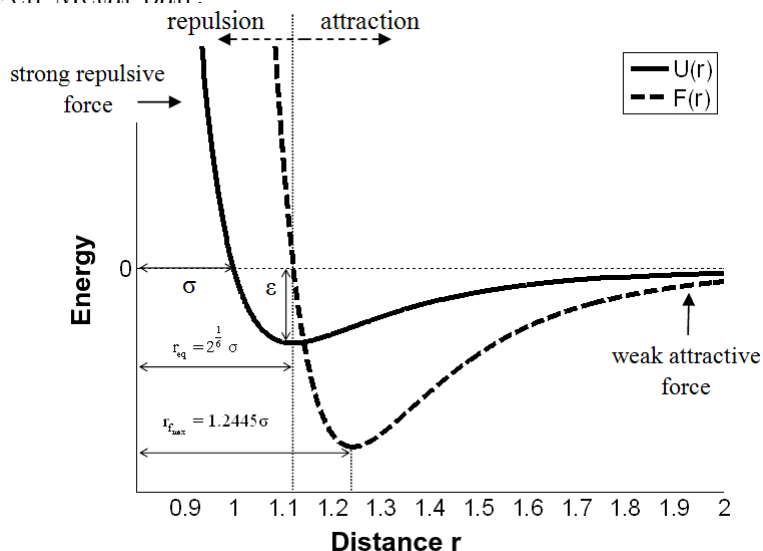


Figure 2.7: Lennard-Jones potential $U(r)$, and internal force $F(r)$. Adapted from Damasceno *et al.*⁹⁴

In this work the exponents m and n of Equation 2.7 were 12 and 6 respectively. This potential, designated as 12-6 LJ,⁹⁵ is implemented in the software employed in this work, called Assisted Model Building with Energy Refinement(AMBER)⁹⁶ (and also in other MD programs as CHARMM,⁹⁷ CVFF⁹⁸ and OPLS-AA⁹⁹)

The attractive term of the potential is represented by the negative part with exponent “-6”. This value has a physical meaning since, by considering that the interaction is mediated by a dipole-dipole interaction, London¹⁰⁰ proved that a thermal average over all angles (allowing the orientation of dipoles to fluctuate with a Boltzmann weighting factor), implicates that the dispersive contribution has to decay with $1/r^6$.¹⁰¹ That said, the other term, which represents the Pauli repulsion, is computed through a steep function that grows asymptotically as approaches zero. This behaviour could be achieved using an exponential function until a certain cut-off radius, or using other polynomial functions. Particularly, the exponent “-12” is widely implemented, since it is computationally very efficient as it is carried out by simply squaring the $1/r^6$ term. Yet, this value carries no physical meaning, and usually leads to an overestimation of the repulsion as pointed out by Bazgier *et al.*¹⁰²

The theory summarized in this chapter was considered during planning and development of the parametrization protocol, and will be referred in the following chapters. The particular details of implementation of this protocol, such as the method or the reason by which many of the parameters were selected and also which tools were applied, are

described in the next chapter.

Chapter 3

PARAMETRIZATION PROTOCOL

The theory that underpins a computational procedure to parametrize a classical potential that includes polarization effects for water-metal interfaces was explained in the last chapter. In this chapter, the scope of this course of action will be delineate. It is worth mentioning that this methodology can be, in principle, applied for any metal, but in particular in this work gold was the subject.

As sketched in the Figure 3.1, the first step of the protocol used to parametrize the force field that models the electrochemical interface between metal and water was the geometry optimization. The rationale behind this approach is that in order to parametrize the force field, one need a geometry that will be used as reference.

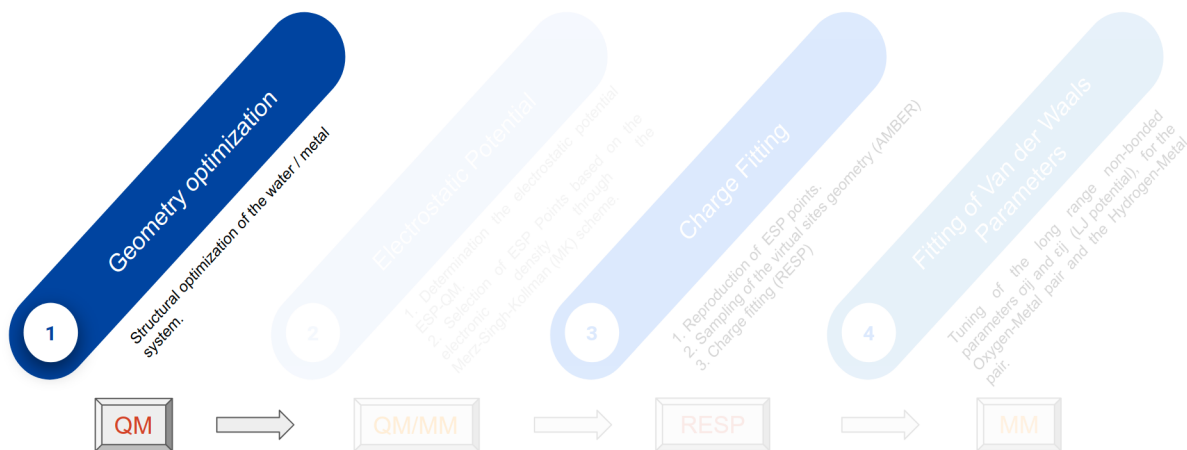


Figure 3.1: Diagram of the steps of a computational protocol to develop a force field for water/metal interface, capable to account the polarization effects of the system. Focus on the first step: Geometry optimization.

In principle, this geometry could be attained through many strategies, e.g. by selecting a representative configuration from a sampling employing an *ab initio* molecular dynamics simulation. But, in this work we chose to start from the simplest approach, that is to use the configuration with lowest energy, i.e. a local minimum (which have been reported in

the literature as the global minimum⁸⁾ of the potential energy surface. This is justified by the fact that the probability of the system to be in that configuration is higher. In order to compute the geometry associated with the minimum of the potential energy we employed an optimization scheme, designated as geometry relaxation procedure, its details will be described in the following.

3.1 Reference geometry calculation procedure

As just mentioned we are searching for geometry configuration with the lowest energy, this means we are probing the potential energy surface for local minima, in essence we use the the forces, determined by Hellman-Feynman theorem,¹⁰³ as a criteria for finding those minima, the closer to zero the closer to one those configurations. For the water-metal system there are some minima reported in the literature, like the flat, the top and the flat-down configurations, as will be shown in the Chapter 4. The difference in energy between these configurations is of the same order of magnitude as the adsorption energy for this system. Therefore, in principle, the geometric reference, our primary goal, could be an average of these configurations. Yet it is also reported in the literature, that the flat configuration is the configuration with the lowest energy,⁸ so we use it as the geometry of reference.

The geometric optimization procedure is sketched in Figure 3.2. Basically, we assumed the Born-Oppenheimer approximation, and applied a self-consistent cycle of a conjugate gradient (CG) procedure, embedded with a self-consistent cycle to determine the electronic structure (in this work by employing the DFT framework as will be explained next). Both these calculations were performed in the Spanish Initiative for Electronic Simulations with Thousands of Atoms (SIESTA)^{104,105} 4.0 code, an open source computer program designed to carry out electronic structure calculations in the framework of Density Functional Theory (DFT) calculations. The correspondent energy and forces of each configuration at each iteration step of the CG were calculated, until a threshold related to the forces was achieved.

As mentioned in the introduction, the objective of this work is to parametrize a force field by fitting some properties, e.g. the electrostatic potential, retrieved from a quantum mechanics calculation. In this matter, DFT, as briefly outlined in Section 2.1, was the chosen framework. Accordingly, the electronic structure calculation on each step of the conjugated gradient method, above mentioned and illustrated in Figure 3.2, was carried

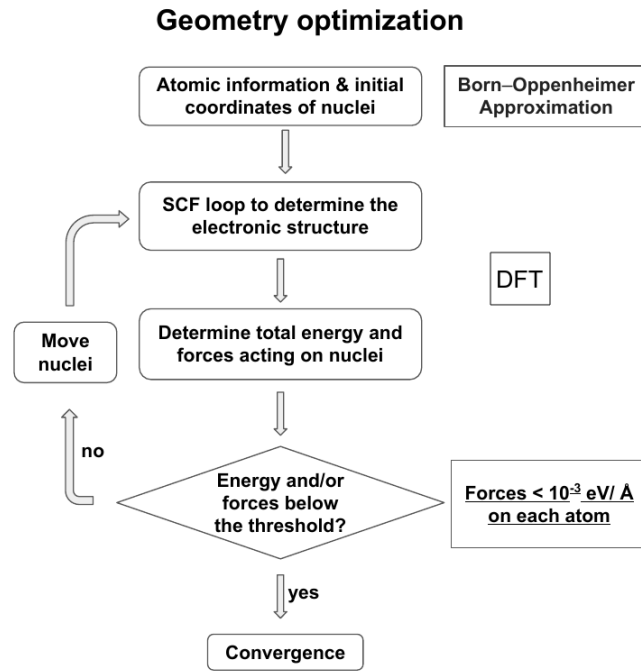


Figure 3.2: Diagram of a geometry optimization procedure, by means of a CG scheme embedded with an electronic structure calculation through DFT method.

out by another self consistent cycle, as shown in Figure 3.3.

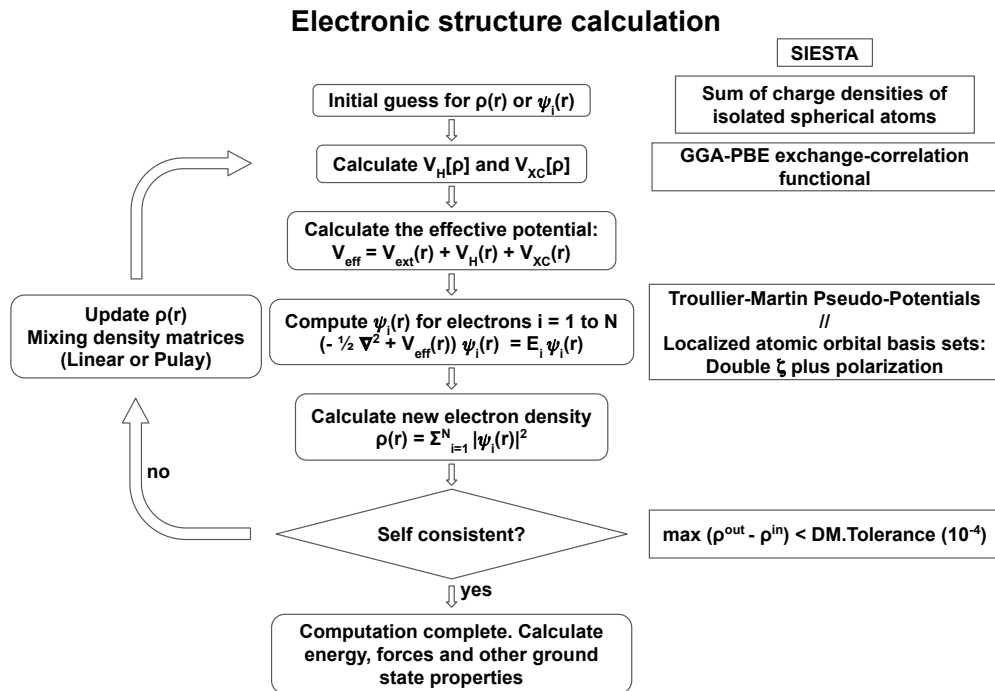


Figure 3.3: Framework of DFT’s self consistent procedure, with indication of the approximations and the restrictions employed. Besides a brief description of the analytical form of some of its steps.

In essence, after the initial “guess” of electron density, this quantity was calculated through the Kohn-Sham scope of DFT, explained in Section 2.1.1. As clarified in Section

2.1.2, this method requires an approximation towards the exchange-correlation functional. Basically this was applied to evaluate the effective potential that was then introduced into the one electron Kohn-Sham system of equations, see Equation 2.1. At this stage, as mentioned in Section 2.1.3, the interaction between core and valence electrons was described by a pseudo-potential, while valence electrons were described by strictly-localized atomic orbitals. This calculation was carried until the difference between the electron density in consecutive steps was below a threshold. For each step a mix of the previous density matrices were used for the calculation of the effective potential. The particulars of the methods, software and criterias applied in this chart are summarized in the Section 4.1.

3.2 Electrostatic potential

Following the flowchart of Figure 2.1, the next issue to be addressed was the electrostatic potential.

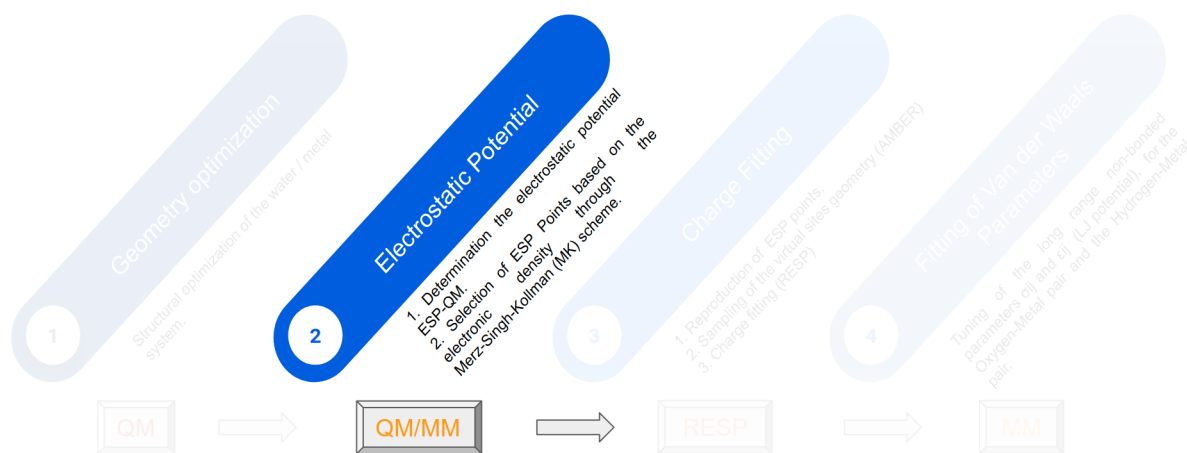


Figure 3.4: Diagram the steps of a computational protocol to develop a force field for water/metal interface, capable to account the polarization effects of the system. Focus on the second step: Computing the electrostatic potential.

The size and time scales of full *ab initio* simulations, required to reproduce electronic degrees of freedom and the sampling of the “thermal/dynamical” properties of the water/metal interface, are beyond the current limit of feasibility since the computational cost is too high. Therefore, following the idea of Warshel and Levitt,³⁷ described in Section 2.2, a hybrid quantum mechanics/molecular mechanics (QM/MM) method, was applied. This allowed to benefit from the merits of both the quantum methods (accuracy) and the classical molecular dynamics (speed).

As mentioned in Section 2.2, the QM/M procedure applied in this work was adapted

from Sanz-Navarro's⁸⁰ and Crespo's⁸¹ articles. In essence, the QM/MM method consist of the following protocol, sketched in Figure 3.5.

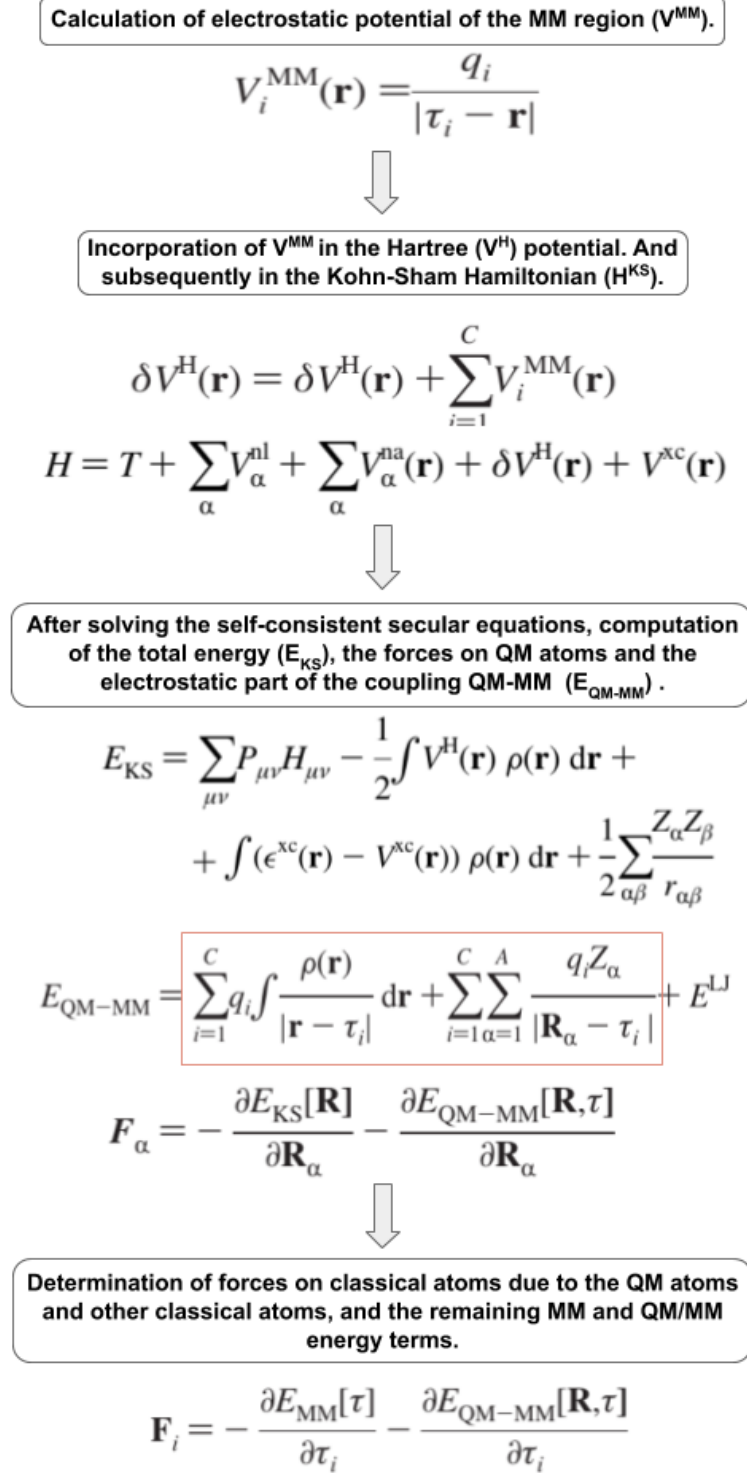


Figure 3.5: Fluxogram of the steps of the QM/MM procedure, with the analytical formulas of the computed parameters at each step, according to Sanz-Navarro's⁸⁰ and Crespo's⁸¹ articles.

The electrostatic potential generated by the classical point charges of the water molecule, see Figure 3.6, was computed and inserted in the QM calculation as an additional external

potential, in Equations 2.1. In this stage, the water molecule was represented with the transferable intermolecular potential with 3 points (TIP3P)¹⁰⁶ model, see information in support Section 6.3.5.

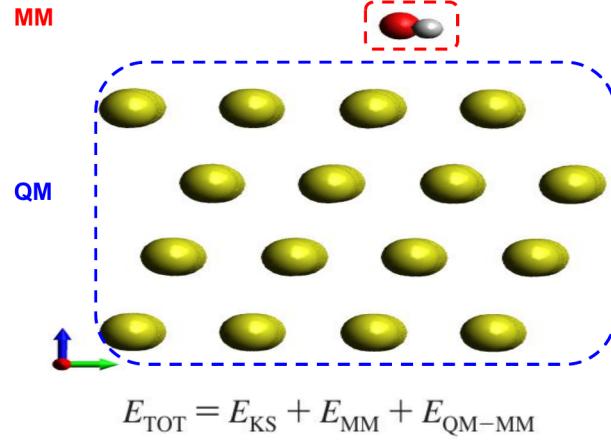


Figure 3.6: Illustration of the QM/MM components. In this case is an additive scheme, without mechanical coupling. The water molecule is represented by the TIP3P model and accounted for the MM part of the system. The electrostatic potential generated by its classical point charges were applied as an external potential in the QM calculation of the metal slab which accounted for the QM part of the system.

Then the QM self-consistent cycle is performed. From this calculations the E_{QM} and the electrostatic part of $E_{\text{QM/MM}}$ is retrieved from SIESTA.^{104,105} Next, the achieved electronic charge density is used to calculate forces in the classical atoms and is computed by the driver program which also calculates the remaining MM and QM/MM energy terms.

From the local minimum energy geometry, the electronic density, the electrostatic potential without external field (No-ext VH) and the neutral atom electrostatic potential (VNA) of this configuration were calculated in SIESTA^{104,105} in a single point hybrid QM/MM calculation calculation.

The neutral atom potential is the sum of the Hartree electrostatic potential $V^H(\vec{r})$ generated by the localized electron density plus the local part of the pseudo-potential V^{loc} :

$$V_{i+e}^{\text{NA}} = \sum_{j=1}^{N_{\text{at}}} \left(V_{e,j}^{H,\text{loc}} + V_{i,j}^{\text{loc}} \right) \quad (3.1)$$

Where the index i indicates ion and the index e indicate electron. The first term in the equation incorporates the long-range ionic contributions to the Hartree potential. This $V^H(\vec{r})$ is generated from the electron density $\rho(\vec{r})$ which is computed as the sum of

the valence electron density localized on atoms in the undistorted bulk plus the distorted electron density due to the formation of surface $\delta\rho(\vec{r})$:

$$\rho(\vec{r}) = \sum_{j=1}^{N_{at}} \rho_{e,j}^{atom} + \delta\rho(\vec{r}) \quad (3.2)$$

When there is a surface, which is the case for this work, the average value of the Hartree potential in the middle of the slab deviate considerably from that of the neutral atom potential. Since the formation of the surface does not affect the neutral atom potential inside of the slab, the mean value of this potential can be adopted as a reference level, which is exactly the criteria adopted by SIESTA developers.¹⁰⁷ Because of this particular reference, in order to allow the transferability of the electrostatic potential, which was used later in the protocol of this work in another code, a VNA correction was performed. Basically we employed a built in from SIESTA,^{104,105} called macroave to plot the nanosmoothed averages of the above mentioned electrostatic potentials related to the direction perpendicular to the slab. Then we compute the shift between them at the region outside the slab.

3.3 Rod model

As mentioned before, another property that the model account is the metal's polarizability. Which means we wanted to assess the propensity that a charge distribution, like the electron cloud of the metal atom, to be influenced, that is for its shape to be distorted, by the an external electric field, in our case generated by electrostatic interactions with its neighbor atoms and the water molecule. In pursuance of mimicking the polarizability of the metal surface induced by the water molecules, instead of changing the charges of the metal atoms, we resorted to the method described in Section 2.3 where virtual charge sites were added to the metal atoms, this is illustrated in Figure 3.7.

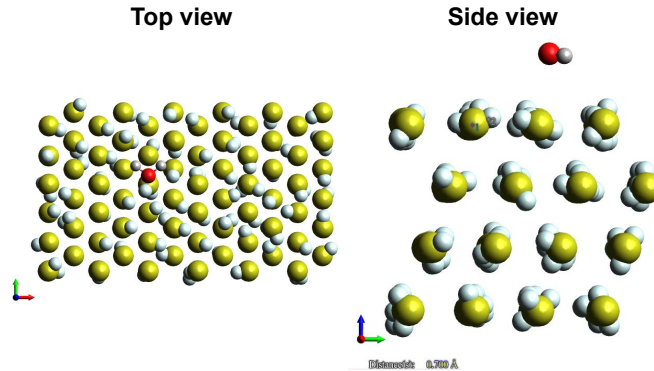


Figure 3.7: Overview of the virtual sites of the rod model. The yellow spheres stands for metal ions, while the red and gray spheres designate the oxygen and hydrogen atoms and white spheres indicates the virtual charged particles of the rod model, respectively.

The procedure, in a few words, involve artificially implementing geometric constraints in the virtual sites, representing charged particles, in order for them to only spin around the respective ion. Therefore we were actually adding dipoles around the metal atoms, which accounted for the polarization effect.

It is worth noticing that, by the same token as in Born-Oppenheimer approximation, the electronic polarization occur in a much shorter time interval than nuclear motion. Also, the interaction between the core and the virtual charge is entirely electrostatic. Since the metal only have an instantaneous dipole, not a permanent one, the temporal average of the dipole moment must be null to produce valid/accurate results. To that end, the parameters of bond length l_0 , virtual site's charge q and mass m should be tuned so that they are bounded by temperature, through properties like polarization ($\alpha = \frac{\mu^2}{3k_B T}$) and the typical intrinsic timescale that is determined by the rotational frequency ($\omega = \frac{2k_B T}{I_0^2 m}$).

In this work, the virtual sites were created with a regular distance l_0 of 0.7 Å, a small charge q of 0.3 a.u. and a massa m of 2 a.u, following the analysis of Iori and Corni.⁸³ These values were selected as to avoid instability issues on simulations. The latter would arise for example if l_0 was to long, because it would cause collisions among the virtual sites or neighbour atoms, or if l_0 was too small, since it would not accurately describe the electrostatics. In addition, the charge must had been concomitantly balanced to avoid non physical events such as the total dipole moment at zero field not averaging to zero. This phenomena was observed when q was high and, to minimize the total energy, a glassy (freezing) behaviour was ensued from alignment of the interacting orientable dipoles in ambient temperature for example. Furthermore, to achieve an equilibrium between the influence of the two parameters, it was also considered that the model was set to describe a conductor, so the polarizability α and hence the charge q , should be high, at least enough to replicate the image charge effects reported for this system.

In order to attain the required averaging a molecular dynamic simulation, was carried out in the Assisted Model Building with Energy Refinement (AMBER).⁹⁶ As it will be shortly clarified in the next section.

3.4 Molecular dynamics

Since there is no requirement of a complex functional form, e.g. with Gaussians, or on-the-fly calculations of the polarization, the QM/MM method with embedded virtual sites as in the rod scheme, is an efficient and fast method to parametrize the water metal-metal

interface interaction through an average polarization.

In order to compute the average behaviour of the rods, classical molecular mechanics was applied. To that end the QM unit cell was replicated and placed in a supercell with a pattern like a 3x2 grid, as shown in Figure 3.8. The rationale behind this approach was that the quantum mechanic calculation carried out in SIESTA had PBC, so in order to remove border effects and emulated a compatible system, the original QM cell had to be replicated.

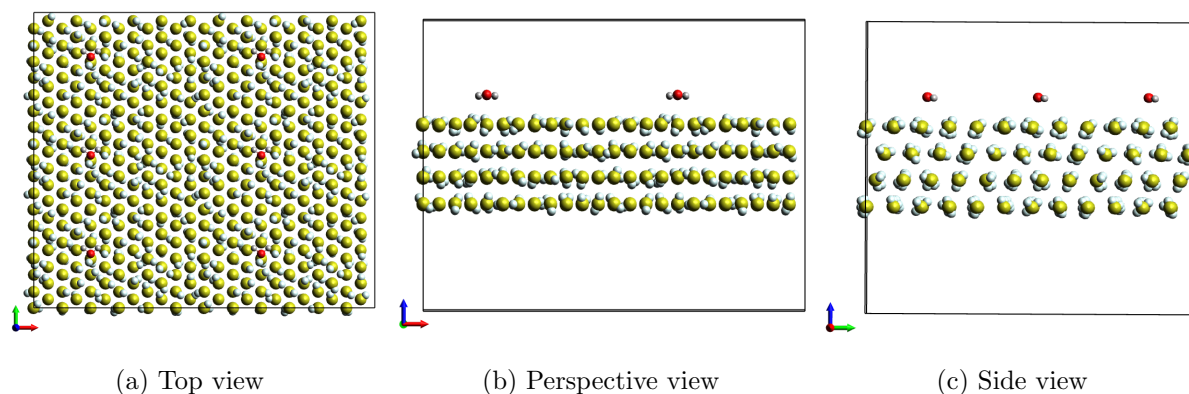


Figure 3.8: Overview of the supercell system, consisted of a 3x2 pattern grid of replicas of the QM unit cell, applied in the classical molecular dynamic simulation in order to retrieve the average behavior of the rods.

Now, about the choice of the configuration/size of the extended system, in previous tests, this setting was the case with minimum computational cost that ensured convergence of desired properties, e.g. distribution of the dipoles.

The classical molecular dynamics simulation to achieve the average configuration of the rods was performed in the NVT ensemble, and it was carried out in the Simulated Annealing with NMR-Derived Energy Restraints (SANDER), a MD engine of AMBER,⁹⁶ and the system was thermalized with Langevin thermostat. The simulation had 10^5 steps of 2 fs and a cutoff radius of 8 Å for Van der Waals and Coulomb interactions were considered. The initial temperature of the thermostat was 400 K and the final temperature was 300 K. The metal and the water atoms were fixed while the virtual sites represented by charge particles were allowed to rotate around the respective ion.

After the running, the average of input coordinates was computed through CPP-TRAJ¹⁰⁸ (another utility of AMBER). The average geometry of the metal/rod fragments gives insights of the influence of polarization, e.g atoms at bottom layers of the slab, are not as affected by the water as the top layers, so the motion of the rods do not present

preferential orientation and as consequence the average length of the rods is smaller. On the other hand the electrostatic force acting on the virtual site moving around the ions at the top layers were more intense, therefore these rods exhibited a more prominent preferential orientation (i.e. higher average length).

By considering only atoms on the top two layers of the slab and imposing the criteria that the average length of the rod must had been larger than 0.05 \AA , the relevant sites were computed.

The purpose of the steps 2 and 3 from the protocol described in Figure 2.1 is to fit classical charges that can reproduce the electrostatic potential acquired from the QM simulation. The solution of this fitting problem is not unique. By imposing different constraints to the charge sites during the fitting procedure, one achieve different patterns of the electrostatic potential. In order to evaluate which restrictions would lead to a potential that best reproduces the QM electrostatic potential, four sets of fitting profiles were created.

The idea was to evaluate the influence of each one of the sites. Therefore the first step is to establish a reference set, i.e. one set must fit all charges. This set was designated as “Free”, basically all the atoms were fitted and the charges were allowed to assume any value.

Then, from the hypothesis that the atoms from two bottom layers and the atoms far from water molecule do not show preferential orientation (polarization) and their charge will have small intensity, that could be neglected, a simplification in the fitting would be to set the value of those atoms as zero and fit only the relevant sites. This restriction was implemented in two sets. The difference between them is that one had only this constraint and was labelled was “M0free”, while the other had an addition constraint that the charges of the relevant site must be equal, this was denominated as “M0Same”. In another set, designated as “Same”, all the atoms were fitted but the relevant sites were set with the same charges. The expectation was that the “Free” would not be the selected set for the final results, since all the charges and rods sites were different. Yet it was used as a reference to assess if enforcing restrictions would have negative effects.

3.5 RESP

As indicated in Figure 3.9, the next step in the protocol was the fitting of charges.

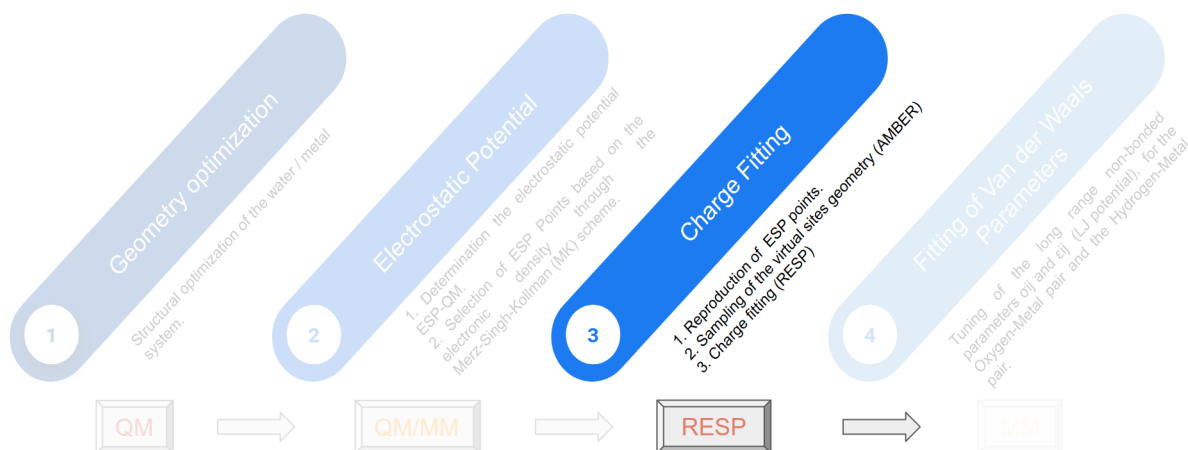


Figure 3.9: Diagram the steps of a computational protocol to develop a force field for water/metal interface, capable to account the polarization effects of the system. Focus on the third step: Fitting of Charges.

As mentioned before, towards the electrostatic part of the force field, four fittings of charge were performed. The fitting procedure used the QM electrostatic potential (along with the VNA correction) as reference. The employed routine is also part of the AMBER⁹⁶ package. In order to minimize the border effects, the system was again replicated and set in an extended cell. In this case there was also a requirement for a central cell, which was the original unit cell from the DFT calculation. Therefore, an odd number of replicas should be created and placed in a square grid. Previous tests indicated that comparing sets with 9 and 25 replicas the charges at the central cell did not differ beyond a certain value, that is 9 replicas in a grid of 3 by 3 pattern was enough to ensure the convergence of the charges, so this was the applied configuration in this work and the image 5 was the target cell. By doing so, a consistent periodic boundary condition was emulated. It is noteworthy that the fitting was also carried out for the other sectors of the grid, yet only the central area was the target area, since it actually has the potential from the *ab initio* calculation.

At this stage an additional constraint, about the electronic density was imposed. Based in the concept from the Merz-Singh-Kollman method and analysing the electrostatic potential from the fittings, we could observe that the range of the electronic density (ρ) had to be between 0.0001 and 0.00075 in order for the fitting sets to reproduce the QM potential.

3.6 Van der Waals interaction

The last part of the protocol conveyed in Figure 2.1 was the fitting of the Van der Waals parameters, which was conceived based in the theory of Section 2.6.

It is worth mentioning that the approach in this work deals with the dispersion interactions separately from the electrostatic interactions, that is we fitted the Van der Waals parameters without considering the electrostatic interactions that we derived in the previous step of the protocol. In principle, since at that stage we had the charges fitted from the QM electrostatic potential, we should have fitted the σ s and ϵ s also accounting for the rods which yielded the polarization of the metal. Yet, as an initial approximation we examined the fitting procedures as if they were independent. We expected that this approach provided values within some ranges, for each of the Lennard-Jones variables, which can be used as initial parameters for a SCAN procedure considering the electrostatic part.

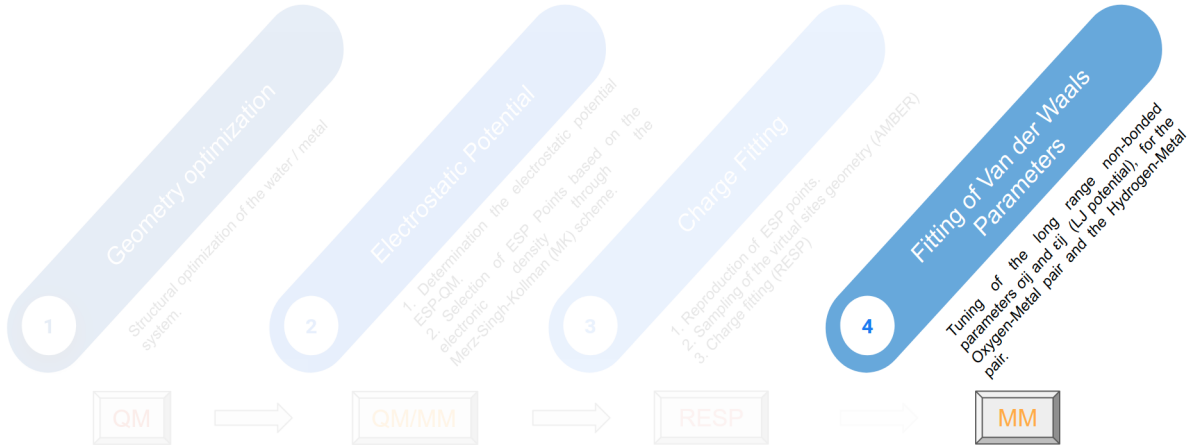


Figure 3.10: Diagram the steps of a computational protocol to develop a force field for water/metal interface, capable to account the polarization effects of the system. Focus on the forth step: Fitting of Van der Waals parameters.

In this step, initially the σ were computed using the engine from Mathematica¹⁰⁹ to solve (find the root of) the equation of the force, see Equation 3.3 (calculated from the definition as minus the gradient of the potential, delimited by Equation 2.7), imposing that the σ had to be positive (since is a distance) and both σ and ϵ had to be real.

$$F = 12 \sum_{ij, \text{nbond}} \epsilon_O \left[\left(\frac{\sigma_O^{*12}}{r_{ij}^{14}} \right) - \left(\frac{\sigma_O^{*6}}{r_{ij}^8} \right) \right] + 12 \sum_{ij, \text{nbond}} \epsilon_H \left[\left(\frac{\sigma_H^{*12}}{r_{ij}^{14}} \right) - \left(\frac{\sigma_H^{*6}}{r_{ij}^8} \right) \right] \quad (3.3)$$

As for the input of r_{ij} , the distances between the atoms of water and the seven nearest metal atoms, retrieved from the QM calculation, were used.

As previously mentioned, we wish to evaluate the four parameters σ_O , ϵ_O , σ_H and ϵ_H . One way to approach this to calculate when the force is zero, see Figure 2.7, since this would allow us to assess the two σ , because the Lennard-Jones potential has some specific correlation between some coefficients.

Now, for the ϵ s, we need an energy scale as reference, so one option is to use the adsorption energy. Basically a small range of ϵ can be used as input of MD energy minimization's and later the adsorption energy of the resulting configuration is compared with the adsorption energy from the QM calculation.

For the metal-metal interaction the parameters proposed by the INTERFACE³² force field were used, it is a non-polarizable force field which treats each gold atoms as a charge-neutral Lennard-Jones particle.

With the parameters fitted (charge and Van der Waals) the polarizable force field to describe the water/gold interface was characterized. In the next chapter the data collected to validate each part of protocol are presented and discussed.

Chapter 4

RESULTS

4.1 System

As mentioned in the previous chapter, the method of parametrization of the force-field to describe water-metal interface interactions is seemingly general, that is, supposedly can be applied to any metal. Yet, in this work, gold (particularly a face centered cubic (FCC) crystal structure Au(111) surface, the most stable surface of gold), was used as prototype system, and in this chapter the data retrieved for this system will be presented and analysed.

The reasoning for choosing the Au(111)-H₂O system is that, from the electrochemical perspective, since electrical conductivity have a crucial impact in performance,¹¹⁰ close packed metal surfaces have already been widely used as template¹¹¹ (partially because they are conductive by nature). However, they are bounded by their corrosive susceptibility.¹¹² Accordingly, a noble metal like gold is a great candidate for electrode material due to its chemical stability, which also have practical convenience for experiments, as samples do not degrade with the atmospheric moist. Yet, this resistance against oxidation in moist, in addition to its relucet/shinny aspect kept its use somewhat restrict to jewellery, art related activities (due to his economical value is not used like other metals for load bearing structures or conductors³²) and used for many centuries as coinage material.¹¹³ Only recently a myriad of applications have been unleashed by the prospect of its catalytic activity, a hot topic in condensed matter and related areas.¹¹³

In addition, gold express many remarkable properties. For instance, comparing with other transition metals, it barely exhibits oxophilicity, that is, it rarely forms oxides.¹¹⁴ Besides, there is an interesting hypothesis that gold form a pseudo-hydrogen bond with water adsorbed at its surface¹¹⁵ which produces another whole bunch of distinctive prop-

erties worth investigating.

In order to assess the quality of the description of the gold, the lattice constant and the work function were computed. As shown in Table 4.1, these properties are in good agreement with the experimental values reported by Patel¹¹⁶ and by Hansson¹¹⁷ respectively, within a margin error of 7%.

		Properties	Experimental	This work	Error %
Slab Bulk		Lattice constant (Å)	4.078	4.23	-3.7
		Work Function (eV)	-5.33	-4.97	6.7

Table 4.1: Properties of the gold slab. Comparing with experimental values reported by Patel¹¹⁶ (lattice constant) and by Hansson¹¹⁷(work function).

The value for lattice constant also agrees with the pattern of PBE results, i.e. to overestimates the empirical value. This value indicates a good balance of the size of the basis set, the pseudo potential and the exchange-correlation functional used.

Now, for the reason an aqueous system was chosen, comparing to other solvents, water have many features favorable for its use in electrolytes, it is not toxic and is abundant in the atmosphere,¹¹⁸ thus is cheap. In addition, due to its high dielectric constant ($\epsilon=78.5$) it can solvate anions and cations and favors ionic reactions.^{119,120}

In order to verify the quality of the representation of the isolated water molecule, its geometric properties and the dipole moment were computed and compared with experimental data reported by Benedict *et al* and¹²¹ and Clough *et al*¹²² respectively, as shown in Table 4.2:

		Properties	Experimental	This work	Error %
Water		Dipole Moment (Debye)	1.8546	2.047	-10.4
		Dist O-H (Å)	0.9572	0.968	-1.1
		Angle \angle H-O-H ($^{\circ}$)	104.52	103.9	0.5

Table 4.2: Properties of the water molecule. Comparing with experimental data reported by Benedict *et al* (water's internal angle and O-H distances) and¹²¹ and Clough *et al*¹²²(dipole moment).

The values for the water also indicates a good description since there is an agreement with experimental values reported in the literature, with an error below 11%.

As explained at the beginning of Chapter 3, we need a geometry reference for the fitting of the parameters of the force field. As input, the prototype system we used was a

FCC metal slab made of 4 layers, each with 6 x 4 atoms, as shown in Figure 4.1, was set in an unit cell with lattice vectors with lengths/magnitudes of 17.99 Å, 10.39 Å and 27.34 Å, with a grid dimension (mesh) along each lattice vector of 192, 120 and 288 points, respectively.

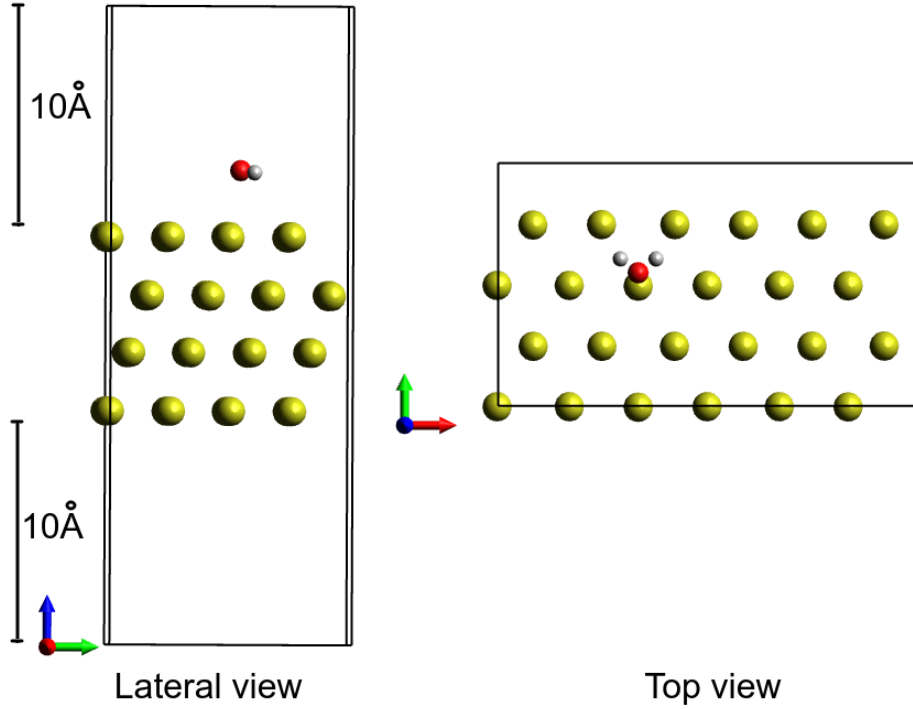


Figure 4.1: Prototype system used in the geometry optimization scheme, a 4 layers slab of gold with 6 vs 4 atoms per layer and one molecule of water, in an unit cell with 20 Å of vacuum in the slab’s non periodical direction.

Since SIESTA^{104,105} works by default with periodic boundary conditions, in order to minimize spurious interaction between slabs¹²³(dipole-dipole interaction existed between neighboring images), 20 Å of vacuum was introduced in the slab’s non periodical direction. Then a water molecule was placed above the slab, that is, a coverage of 1/24 was used.

With the topology set described above, a self-consistent cycle of geometric optimization procedure was performed as explained in the Section 3.1.

Both the CG’s and the electronic structure calculation’s self consistent cycles were carried out in the SIESTA 4.0 code.^{104,105}

In order to describe the exchange-correlation effects, the Perdew, Burke and Ernzerhof (PBE)^{57,58} exchange-correlation functional (a “flavor” of the Generalized Gradient Approximation (GGA) class of exchange-correlation functionals) was chosen. Representa-

tion of the electronic core states were accounted for by means of norm conserving pseudo-potentials in the Troullier-Martin form.⁷⁹ The sampling of the first Brillouin zone was just on the Gamma Γ point.

The orbitals were expanded using strictly-localized atomic orbital basis sets, a type of finite support basis set. Unlimited multiple-zeta and angular momenta, polarization and off-site orbitals can be modeled with this sort of basis set. In this work some double- ζ plus polarization basis sets (PP-pVDZ) were used. They are described in depth in the supplementary section (chapter 6) along with the pseudo-potentials.

The criteria for conjugate gradient SCF loop was that the forces (determined by Hellman-Feynman theorem¹⁰³) had the restriction to be less than 10^{-3} eV/Å on each atom. The difference between the electron density in consecutive steps for the electronic structure determination had the threshold of 10^{-4} .

In order to assess the quality of the description of the interactions in the water/metal interface, we analysed some adsorption parameters. Initially we investigated the geometric aspects of the adsorption. The first addressed topic was the adsorption site of water on the Au(111), that is the relative position of water related to the gold atoms. Water can be above an atom of metal or above the bond between two metal atoms, considering a FCC(111) surface seeing from the top these possibilities are: atop (the atom rest directly above a metal atom from the top layer), hollow HPC (the atom rest directly above a metal atom from the first sublayer), hollow FCC (the atom rest directly above a metal atom from the second sublayer) or bridge. See Figure 4.2:

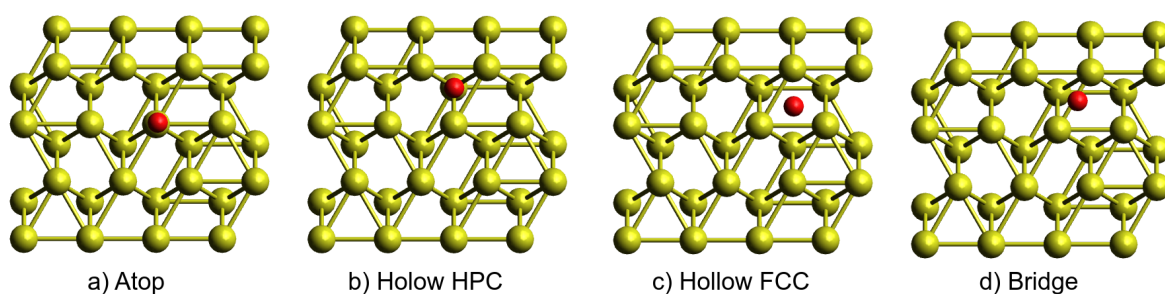


Figure 4.2: Illustration from top perspective, of water's adsorption sites at the Au(111) surface. The yellow spheres stands for gold atoms, while the red spheres designate the oxygen atom of the water molecule.

According to Huzayyin,⁸ the atop position is the most stable position for water at a gold surface. The parameter used in this work to clarify if water was at the atop

adsorption site, was the distance between the closest gold atom and the projection of the oxygen position on the slab's surface. here we designated it as δ , see Figure 4.3:

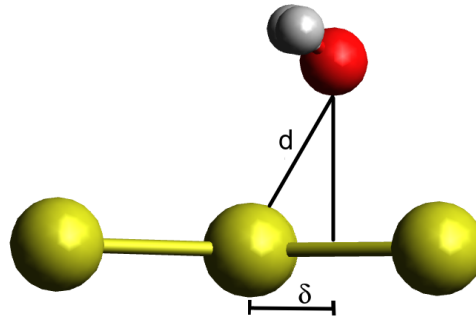


Figure 4.3: Distances between water molecule and gold atoms in the top layer. Distance δ was applied to check if the water molecule was at atop position, and distance d was applied in the Van der Waals parameters fitting. The yellow spheres stands for gold atoms, while the red and gray spheres designate the oxygen and hydrogen atoms of the water molecule, respectively.

The second geometric aspect that was analysed was the orientation of water's dipole moment relative to the slab's surface. Considering the directions of the OH bonds, we can describe if the orientation of water's dipole moment is parallel to the surface or if it is perpendicular to it, and in this case if it is pointing towards the surface or away from it. In this work we achieved the local minima in three configurations namely configurations "Flat", "Flat-Down" and "Up". See Figure 4.4.

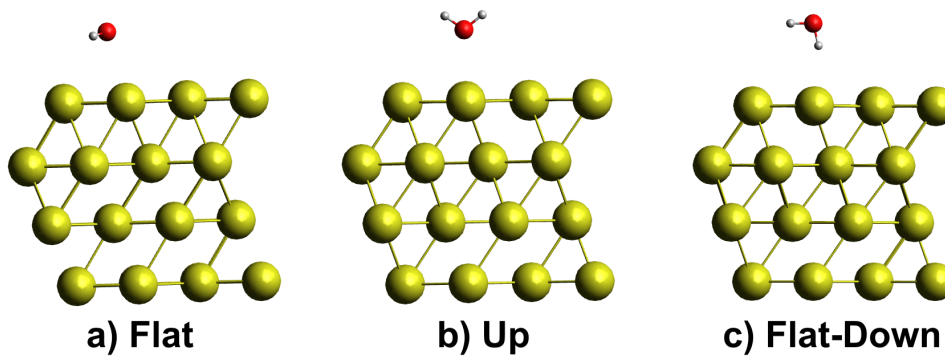


Figure 4.4: Most energetically stable geometries of the isolated water molecule at a Au(111) metallic surface. On the left there is the flat configuration, with water's dipole moment parallel to the slab's surface, on the middle there is the up configuration with the water's dipole moment perpendicular to the slab's surface and pointing away from surface and on the right theres the flat-down configuration with the water's dipole moment pointing towards the slab's surface in a slanted/oblique direction.

The parameter used in this work to differentiate between these configurations was the

angle between the vectors of the OH bonds and the vector parallel to the surface, called the binding angle α , as shown in Figure 4.5:

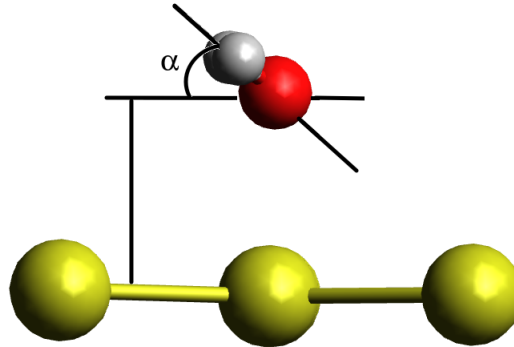


Figure 4.5: Illustration of the binding angle α between water and the gold surface, applied to identify if the water molecule was in the flat, down, up or flat-down configuration.

	Dist O-Au (Å)	δ (Å)	Dist O-H (Å)	\angle H-O-H ($^\circ$)	$\angle\alpha$ ($^\circ$)
Flat	2.93	0.62	0.97	103.68	-5.94
Flat_down	3.49	0.07	0.97	103.27	89.75
Up	2.96	0.72	0.97	104.89	-

In all configurations water was atop, but the flat and up were slightly dislocated ($\delta = 0.62\text{\AA}$ and $\delta = 0.62\text{\AA}$ respectively). In the flat configuration, the hydrogens were slightly pointing towards the surface ($\alpha = 84.06^\circ$), while in the up position they were practically perpendicular to the surface and pointing away from the surface. Considering the distance between oxygen and surface of gold atoms (2.93\AA) the flat configuration is closest to the experimental value of 2.85\AA , reported by Huzayyin.⁸

The internal angle of water were between 103.27° and 104.89° while the OH bond distance was 0.97\AA for the three cases, these are in good agreement with the experimental values (104.52° and 0.957\AA) also reported by Huzayyin.⁸

Along with the geometric parameters, the adsorption energy was also calculated in order to evaluate the quality of the description of the interactions between water molecule and the metal slab. The adsorption energy per water molecule was determined according to the formula:¹¹³

$$E_{ads} = E_{H_2O/Au} - E_{H_2O} - E_{Au} \quad (4.1)$$

where $E_{H_2O/Au}$, E_{Au} and E_{H_2O} are the energy of the total water-metal system, the bare surface and the isolated water molecule, respectively. In this context, a negative value of

E_{ads} indicates an exothermic chemisorption process.

Config	Ads (eV)	Ads with BSSE cor. (eV)
Flat	-0.15	-0.09
Flat_down	-0.11	-0.06
Up	-0.09	-0.06

Table 4.3: Adsorption energies for each configuration of water molecule related to the metal surface, with and without BSSE error correction.

In the flat configuration the adsorption energy was -0.15 eV. Accounting the correction for the basis set superposition error (BSSE), this was reduced by 40% (-0.09 eV). This could indicate that large basis sets were not used in the calculation. Yet another relevant point in this analysis is about the occupancy of orbitals. Usually, using only occupied orbitals, a small BSSE is induced. But in this work, in order to account for polarization effects of the metal, a basis set with unoccupied orbital was applied, see information in the support Section 6.1. Comparing with different basis set, previously examined for this system, we believe that the later factor, had the major influence in the overestimation of the energy.

In the literature, there are adsorption energy values reported varying between -0.11 eV and -0.17 eV^{8,24,25,113,124} so the value computed in this work is within range. It is worth mentioning that these energy values were computed with different constraints, for example number of layers in the slab, vacuum region placed between the slabs, coverage and position of the water molecule, besides different functionals or methods of different levels of theory. All these factors contribute for the discrepancies among them. Nevertheless, in the discussion of results of the values of each respective article, the range was deemed as in good agreement with the experimental value so the achieved value was also considered accurate. The difference between total energy of each configuration was also computed and, as expected, the flat was the most energetically favorable, with a difference in energy of 0.05 eV and 0.07 eV comparing with the flat-down and the up configuration respectively.

With the geometry data of the flat configuration, the electrostatic potential was computed as described in Section 3.2. As mentioned in that Section, in order for the electrostatic potential from the QM calculation to be fitted and compared with the potential produced by the force field, a VNA correction was required to allow the transferability of the electrostatic potential, since SIESTA^{104,105} has a particular energy reference scale. To

compute the VNA correction we needed to calculate the electrostatic potential without external field and the neutral atom electrostatic potential in order to set the electrostatic potential. The VNA correction was calculated based on the Figure 4.6, in which are shown the plots of the nanosmoothed average electrostatic potentials related to the direction perpendicular to the slab.

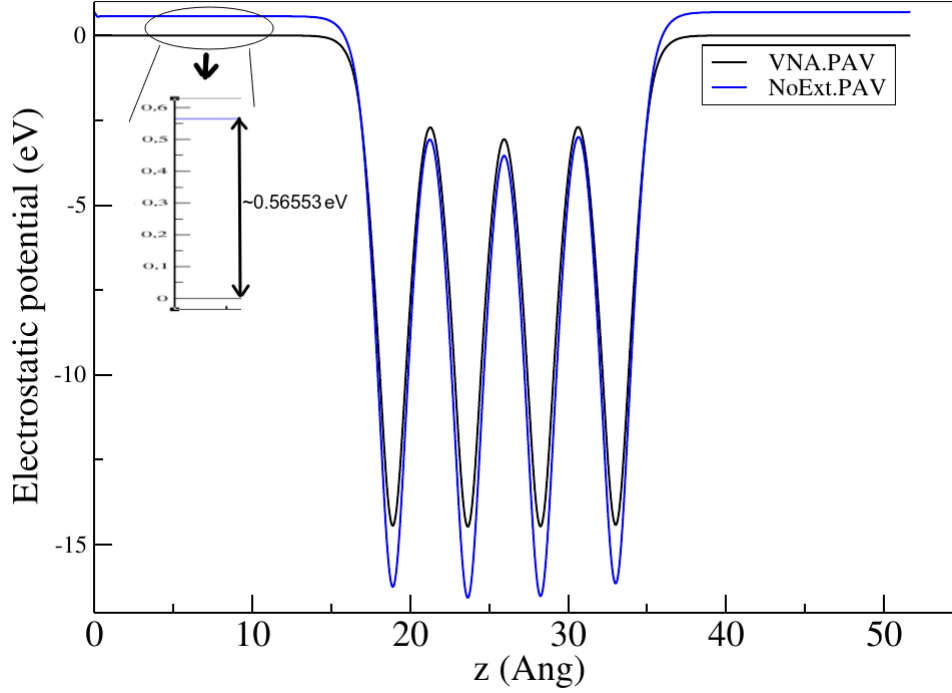


Figure 4.6: Plot of the nanosmoothed averages, of the electrostatic potentials without external field (No-ext) and the neutral atom electrostatic potential, in the z direction (slab's non periodical direction) in order to compute the VNA Shift.

As shown in Figure 4.6, for the prototype system of this work, the VNA correction was 0.57 eV.

4.2 Selected sites

As mentioned in the Sections 2.3, 3.3 and 3.4, in order for the rod scheme to have physical meaning, we need to compute an orientational average of the rods. There were two ways to achieve this, one by sampling many configurations of the system, altering the rod's positions, and at each configuration we perform a charge fitting and at the end we calculate the average of these fittings, and the other way as to compute the average of the configurations through molecular dynamics simulation and then perform the fitting with

this configuration. We assumed the approximation that these alternatives were equivalent and we proceeded with the latter.

From the molecular dynamics simulation, as explained in Section 3.4, we obtained the average configuration shown in Figures 4.7 and 4.8.

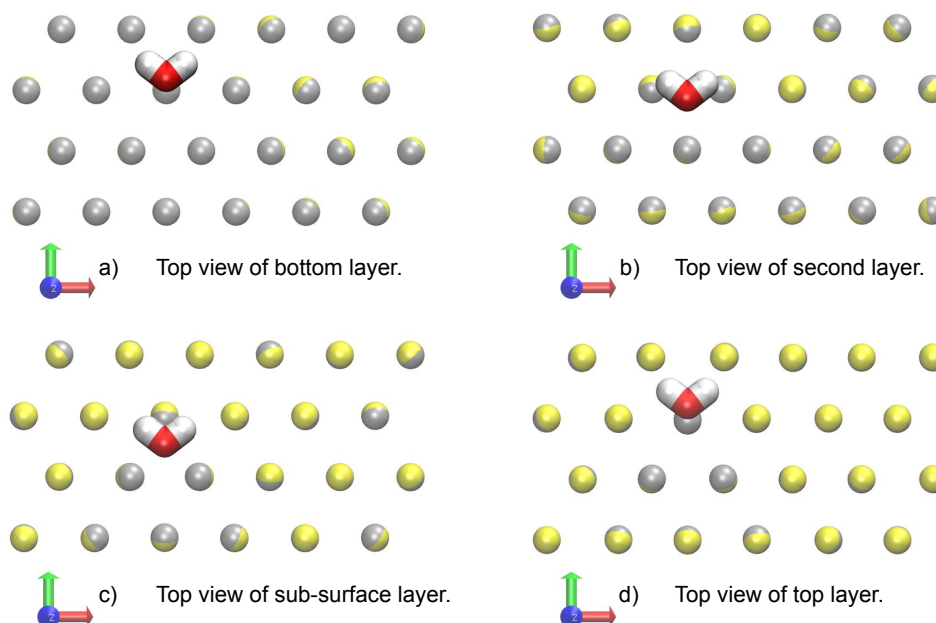


Figure 4.7: Top view of the average behaviour of the rods for each layer of the slab. In the yellow/gray spheres, yellow stands for gold atoms while the gray portion indicates the virtual sites representing the charged particles of the rod model. The red and white spheres designate the oxygen and hydrogen atoms of the water molecule, respectively.

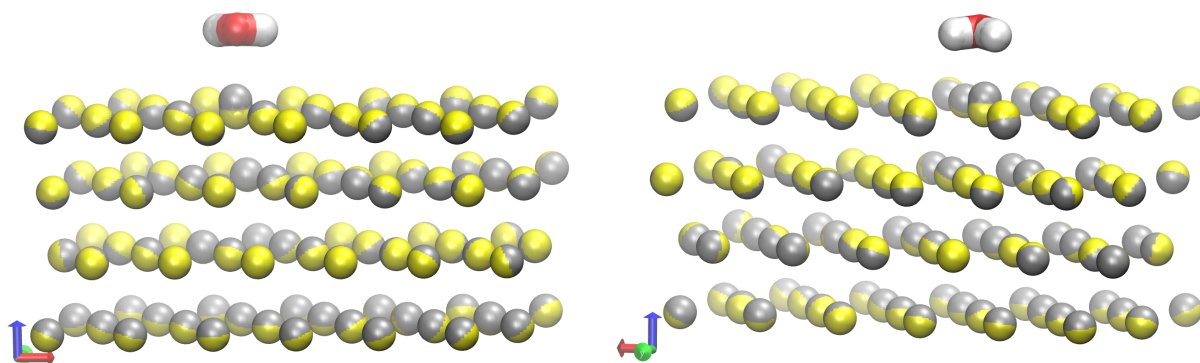


Figure 4.8: Side view of the average behaviour of the rods. In the yellow/gray spheres, yellow stands for gold atoms while the gray portion indicates the virtual sites representing the charged particles of the rod model. The red and white spheres designate the oxygen and hydrogen atoms of the water molecule, respectively.

Following the conjecture that the rods on the top layer would account for most part

of the total polarization, and the incorporation of a few additional layers of metal atoms with rods would account for the rest of the polarization, only the two top layers were considered in the selection of relevant sites. In addition, one constraint was applied: the average length l of the rod of the respective gold atom had to be greater than or equal to 0.05 \AA . By imposing these restrictions, 15 relevant sites were selected, as shown in Figure 4.9, the metal index and average length l of the rod are reported in Table 4.4:

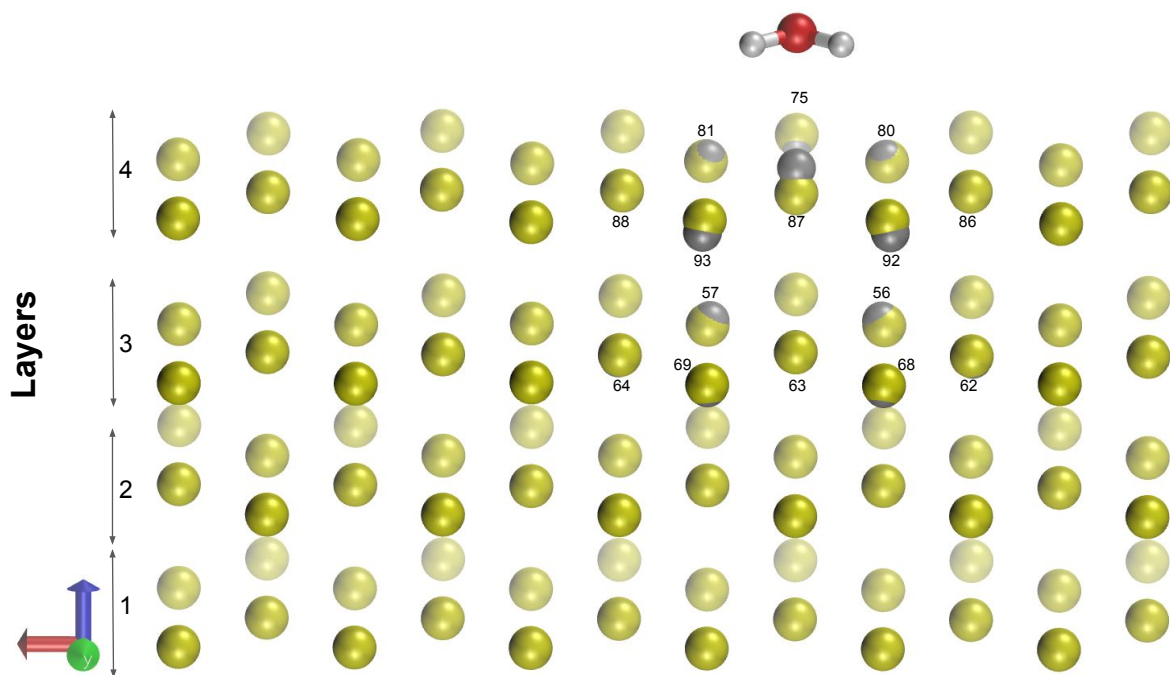


Figure 4.9: Perspective view of the average behaviour of the rods, with indication of the relevant sites.

The top layer starts from metal ID 73, so 8 relevant sites were on the sub surface layer and 10 were on the top layer. From the literature, e.g. from the work of Liu *et al*,¹¹³ it is well known that, for this system, the interaction between p orbital of adsorbate (oxygen) and d orbital of gold has a stressed role in the adsorbate – substrate interaction, therefore the binding is strongly localized on the surface. Indeed, virtual sites of surface atoms around the water showed the most intense preferential orientation, with larger values of average length of the rods.

In this sense, as expected, the nearest gold atom (ID 87) had the largest average length (0.44 \AA), towards the oxygen site, while the next closest atoms (ID 92 and 93) pointed away from the hydrogen sites (0.21 \AA), see Figure 4.9. In this image sites with values of l greater than 0.08 \AA (except for ID 63, because it was pointing in the opposite direction)

could be visualized.

Metal ID	$l(\text{\AA})$
56	0.09
57	0.09
62	0.06
63	0.09
64	0.06
68	0.06
69	0.05
75	0.06
80	0.06
81	0.06
86	0.06
87	0.44
88	0.06
92	0.21
93	0.21

Table 4.4: Description of the average lengths l of the rods of the selected sites and the indexes of their correspondent metal. The l s were computed in CPPTRAJ after a 600 ps classical molecular dynamics simulation in the NVT ensemble. These rods were selected by fulfilling the criteria that this l s were larger or equal than 0.05 \AA and also that the virtual sites were associated with metal atoms belonging to the top two layers.

After the analysis of the selected sites, the restriction of considering only the top layers was removed to check if more relevant sites would appear in case of just the criteria for average length of the rods was met. By doing so, as expected considering the decay of values of l from the top and the sub layer, only the previous 15 sites were selected.

4.3 RESP

After identifying the relevant sites, we wished to evaluate which sets of restrictions, would provide good accuracy in the charge fitting. As mentioned in Section 3.4 we needed a control group so we established the set “Free” in which all charges were fitted. From

the hypothesis that the atoms from sites other than the selected as relevant were neutral, we established the sets “M0Free” and “M0Same”, by imposing that the charges at the relevant sites were fitted while the charge at other sites were set as zero. In the later an additional constraint was imposed that charges at relevant sites were equal. This additional constrain was used alone in another set, designated as “Same”.

The evaluation of the quality of the RESP fittings was conducted qualitatively from plots of isosurfaces of the electrostatic potential, see Figures 4.10 to 4.13 and quantitatively through evaluations of the associated errors, see Table 4.5. From these data, one of the sets of restriction was selected and an analysis of its respective charges was performed.

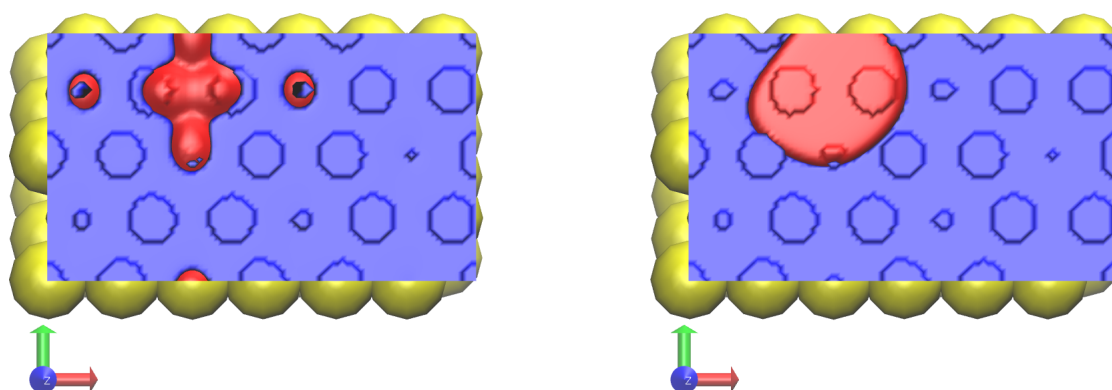


Figure 4.10: Comparison between QM/MM (left), and RESP-Free (right, all charges were fitted) potential. The blue and red colors represent the most negative and most positive values of electrostatic potential.

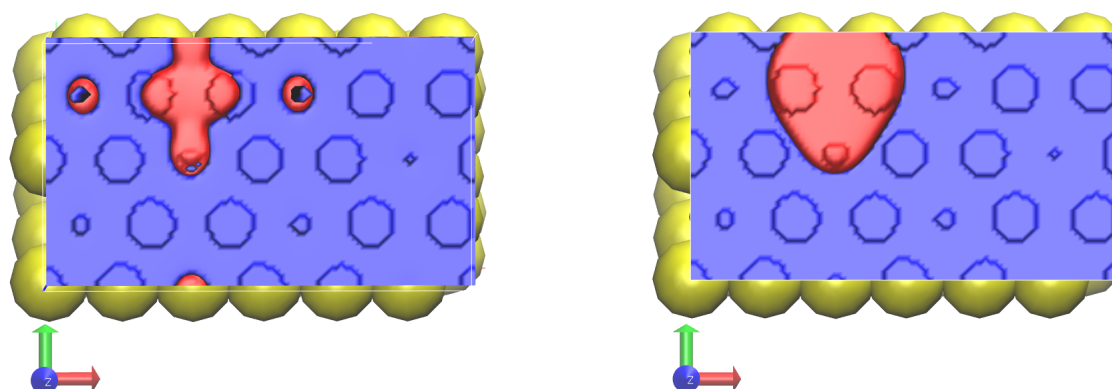


Figure 4.11: Comparison between QM/MM (left) and RESP-M0free (right, charges of the relevant site were fitted while charges of other sites were set to be zero) potential. The blue and red colors represent the most negative and most positive values of electrostatic potential.

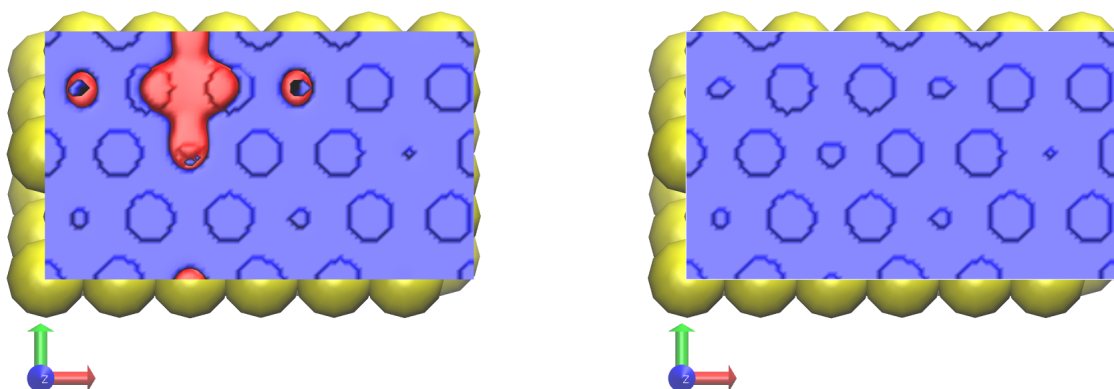


Figure 4.12: Comparison between QM/MM (left) and RESP-M0Same (right, charges of the relevant site were equal while charges of other sites were set to be zero) potential. The blue and red colors represent the most negative and most positive values of electrostatic potential.

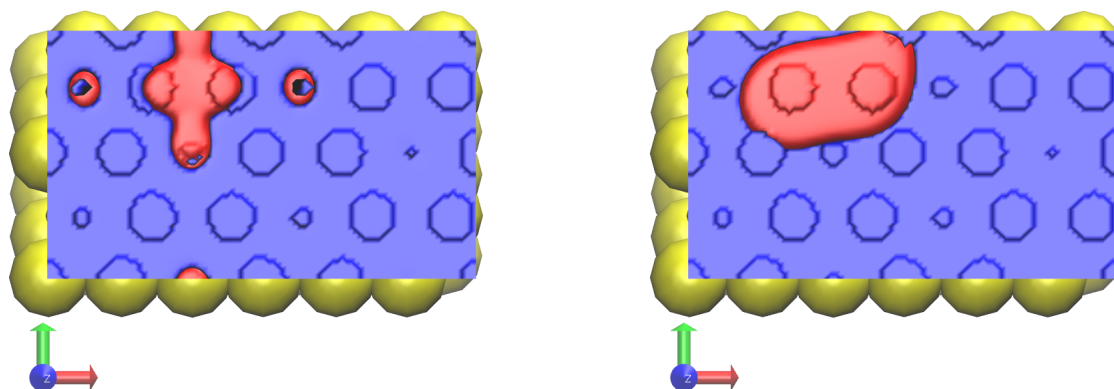


Figure 4.13: Comparison between QM/MM (left) and RESP-Same (right, charges of the relevant site were equal while the charges at other sites were fitted) potential. The blue and red colors represent the most negative and most positive values of electrostatic potential.

As shown in Figures 4.10 to 4.13, only the set “M0Same” was not able to pinpoint the correct main region comparing with the plot of the QM electrostatic potential. In this case, only the potential of the metal without the image charge can be seen.

As shown in Figure 4.14, the electrostatic potential from the QM/MM calculation presents two separately regions with positive potential indicated by “1” and “2” in the image. This pattern appeared because the water molecule was set near a border of the unit cell and since QM calculations uses periodic boundary conditions, part of the potential that represents the interactions in the interface was depicted in the opposite side of the cell. None of the fitting sets could accurately describe region “2”. This is reasonable for the M0free and M0Same sets, since the relevant sites, which were the only ones with charges different from zero, were all concentrated in the region “1”. Yet for the Free and

Same sets, where all charges were fitted, it was expected to correctly exhibit the pattern of region “2”. This could mean that the intensity of that potential was just below sensibility of the fitting procedure, or that a larger system would be required to eliminate the border effects during the RESP procedure.

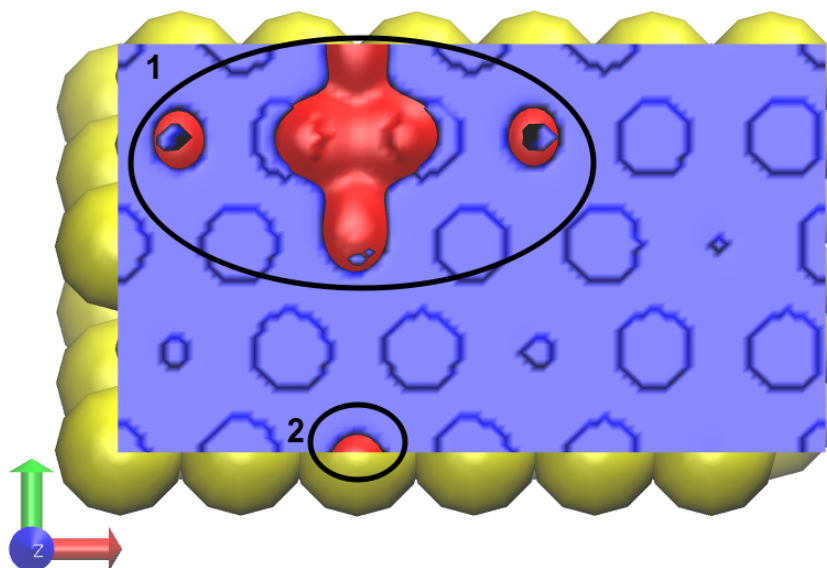


Figure 4.14: QM/MM electrostatic potential. The blue and red colors represent the most negative and most positive values of electrostatic potential.

Qualitatively the M0free seems to be the set with the best restriction, since as indicated by Figure 4.11, it identified the correct region where the interaction of the slab with the water is more intense and also preserved the symmetry of the region as in the QM potential.

As shown in Table 4.5, the root-mean-square (RMS) error and the relative root-mean-square (RRMS) error¹, per image in each set of restrictions were calculated to compare the weight that each constraint had in the quality of the fittings.

$$RMS = \sqrt{\frac{\sum_{i=1}^n (\hat{y}_i - y_i)^2}{n}} \quad RRMS = \sqrt{\frac{ERROR^2}{Total \quad Variance}} \quad (4.2)$$

where n is the test set, \hat{y}_i are the predicted values and y_i are the observable values.

¹Obtained by dividing the RMS by the mean of observed values.

	Free		M0free		M0Same		Same	
AREA	RRMS	RMS	RRMS	RMS	RRMS	RMS	RRMS	RMS
Full System	0.60594	0.80289	0.64669	0.85688	0.74093	0.98175	0.62463	0.82765
Image 1	0.58988	0.78081	0.65003	0.86044	0.75937	1.00517	0.61714	0.8169
Image 2	0.61304	0.81335	0.64723	0.85871	0.72547	0.96251	0.63196	0.83845
Image 3	0.59003	0.78101	0.64367	0.85202	0.74191	0.98205	0.61411	0.81289
Image 4	0.58753	0.77833	0.64287	0.85163	0.73362	0.97186	0.61454	0.81411
Image 5	0.64196	0.85229	0.64458	0.85576	0.70896	0.94124	0.64804	0.86035
Image 6	0.58926	0.78061	0.63983	0.84761	0.7312	0.96865	0.60908	0.80688
Image 7	0.60996	0.80739	0.65621	0.86861	0.78485	1.03889	0.62658	0.8294
Image 8	0.62393	0.82779	0.64766	0.85928	0.73291	0.97238	0.63949	0.84843
Image 9	0.60634	0.80261	0.64775	0.85742	0.74609	0.98759	0.62012	0.82084

Table 4.5: Statistics of RESP fitting. Showing the root-mean-square error and the relative root-mean-square error for each image in each set of restrictions applied in the RESP procedure.

At each set of restriction, both errors followed the same trend. Bearing in mind that a lower value of RMS, indicates that the model can predict the data more accurately, one can observe the following:

In the target image, the set “Free” had the smallest errors while the set “M0Same” had the largest error. This was expected since in set “Free” all atoms were fitted and qualitatively was evident set “M0Same” does not reproduce the electrostatic potential. The second smallest errors were in the set “M0free”, this was different for the other images. Since in sets “Free” and “Same”, all atoms were fitted the accuracy was expected to be higher. This may indicate that in average the charges at sites that were not deemed relevant are actually zero, which was exactly the restriction imposed in the set “M0free”. This was checked in Tables 4.6 and 4.7. Indeed for the two bottom layers the average was zero as in the set “M0free”. It is worth noticing that since the fitting method applied a hyperbolic restraint function, the magnitude of the charges was small, so this may difficult the analysis. This data also corroborates that the set “M0free” may be a good choice for the fitting.

Image\Layer	Element	Free				Qtot-Image
		1	2	3	4	
1	Au	0.004	-0.003	-0.006	0.004	-0.059
	HR	0.004	-0.003	-0.006	0.004	
2	Au	0.000	-0.005	-0.003	0.004	-0.196
	HR	0.000	-0.005	-0.003	0.004	
3	Au	0.003	-0.003	-0.005	0.003	-0.058
	HR	0.003	-0.003	-0.005	0.003	
4	Au	0.006	-0.001	-0.005	0.002	0.077
	HR	0.006	-0.001	-0.005	0.002	
5	Au	0.000	0.000	0.000	0.002	0.000
	HR	0.000	0.000	0.000	-0.002	
6	Au	0.007	-0.001	-0.005	0.001	0.062
	HR	0.006	-0.001	-0.005	0.001	
7	Au	0.007	0.000	-0.005	0.001	0.136
	HR	0.007	0.000	-0.005	0.001	
8	Au	0.004	-0.002	-0.003	0.000	-0.008
	HR	0.004	-0.002	-0.003	0.000	
9	Au	0.006	-0.002	-0.004	0.001	0.046
	HR	0.006	-0.002	-0.005	0.001	

Table 4.6: Average RESP charges of each layer of the slab for the set “Free”.

Image\Layer	Element	Same				Qtot-Image
		1	2	3	4	
1	Au	0.005	-0.002	-0.007	0.005	0.041
	HR	0.005	-0.002	-0.007	0.004	
2	Au	0.001	-0.005	-0.004	0.006	-0.200
	HR	0.001	-0.005	-0.005	0.004	
3	Au	0.004	-0.001	-0.006	0.004	0.038
	HR	0.004	-0.001	-0.006	0.004	
4	Au	0.006	0.000	-0.007	0.003	0.076
	HR	0.006	0.000	-0.008	0.003	
5	Au	0.000	0.000	0.002	0.002	0.000
	HR	0.000	0.000	-0.002	-0.002	
6	Au	0.006	0.000	-0.007	0.003	0.055
	HR	0.006	0.000	-0.007	0.002	
7	Au	0.006	-0.001	-0.007	0.003	0.000
	HR	0.006	-0.001	-0.007	0.002	
8	Au	0.006	0.000	-0.006	0.002	0.064
	HR	0.006	0.000	-0.007	0.001	
9	Au	0.004	-0.002	-0.007	0.004	-0.074
	HR	0.004	-0.002	-0.007	0.003	

Table 4.7: Average RESP charges of each layer of the slab for the set “Same”.

The charges from the RESP fitting, for each of the fifteen relevant sites, considering each set of restrictions, in the Image 5 is shown in Figure 4.15:

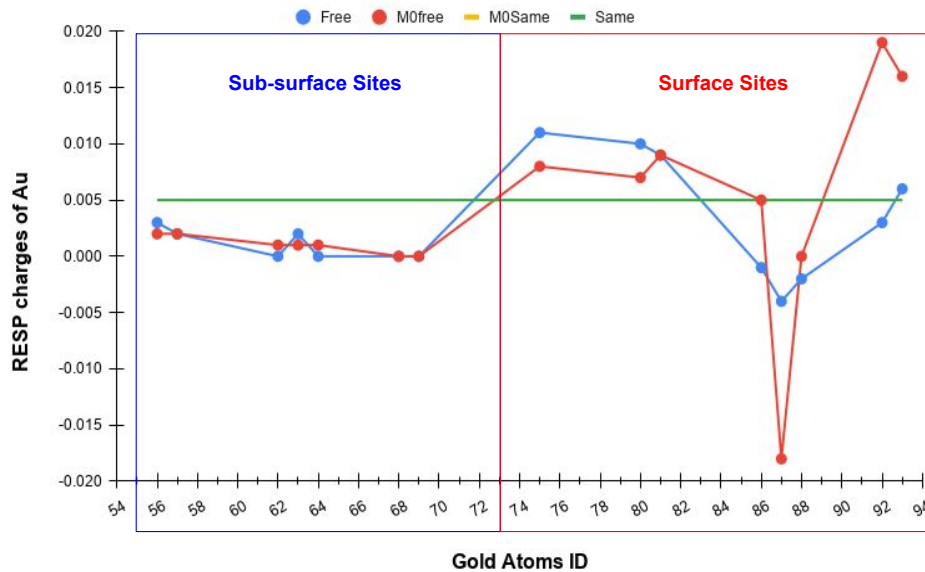


Figure 4.15: Charges from the RESP fitting of the QM electrostatic potential, for each of the fifteen relevant sites, in each set of restrictions, in the Image 5.

The average charge for the set “Free” was 0.003, while for set “M0free” was 0.004, and for the sets “M0Same” and “Same” was 0.005. As expected, for the sets “Free” and “M0free”, the site “87” had the charge with more intensity followed by the sites “92” and “93”. For these two sets the sub-surface sites were practically the same, but for the surface, although most of the sites followed a similar trend, they were quite different in intensity.

4.4 Adjustment of Van der Waals parameters

In order to apply the method described in Section 2.6, for each configuration of local minima achieved by QM calculations, the distances between each atom from the water molecule and the seven nearest gold atoms were computed, see Figures 4.16 to 4.18 they are reported in Table 4.8

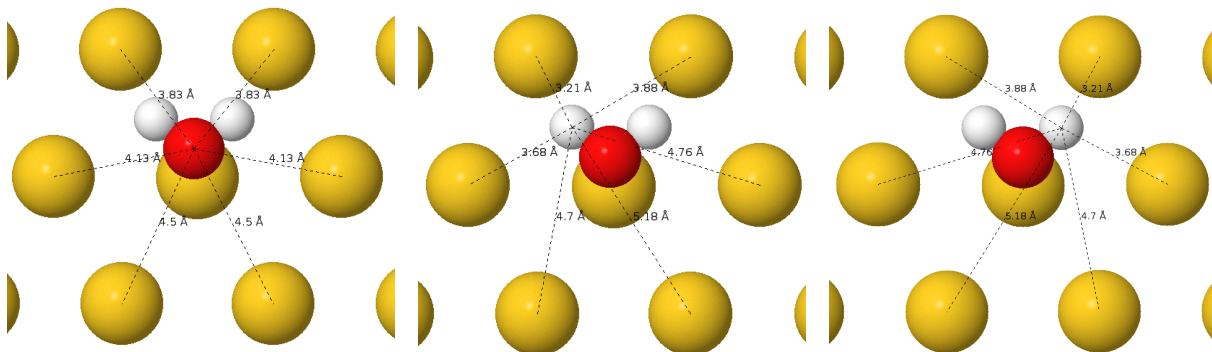


Figure 4.16: Distances between each atom from the water molecule in the flat configuration and the seven nearest gold atoms. On the left the focus is the oxygen, in the middle is one of the hydrogen labeled as Hydrogen 1 and on the right is the other hydrogen labeled as Hydrogen 2.

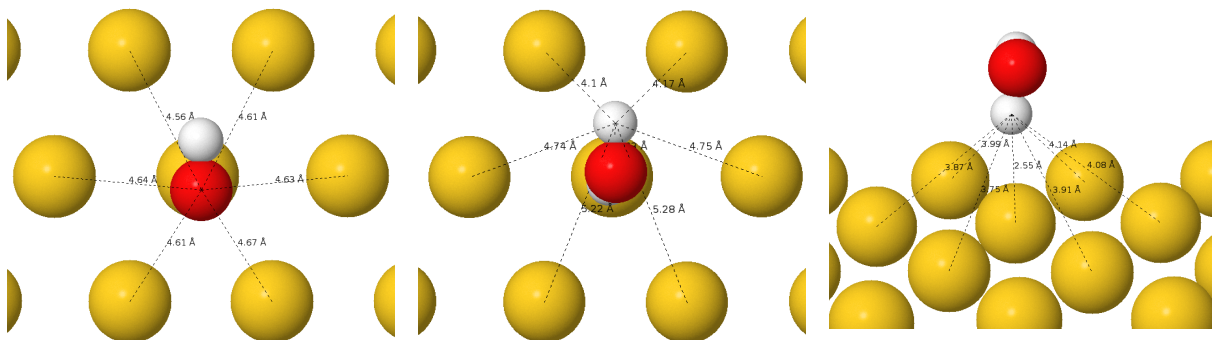


Figure 4.17: Distances between each atom from the water molecule in the flat-down configuration and the seven nearest gold atoms. On the left the focus is the oxygen, in the middle is one of the hydrogen labeled as Hydrogen 1 and on the right is the other hydrogen labeled as Hydrogen 2.

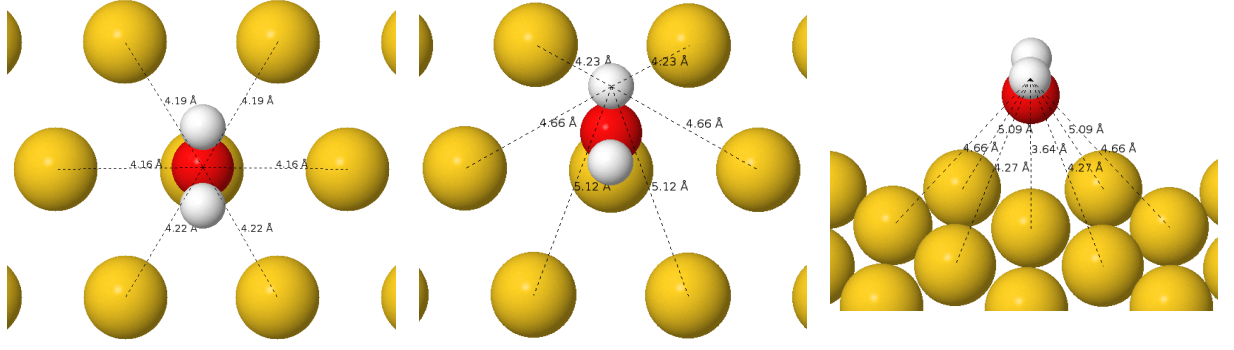


Figure 4.18: Distances between each atom from the water molecule in the flat configuration and the seven nearest gold atoms. On the left the focus is the oxygen, in the middle is one of the hydrogen labeled as Hydrogen 1 and on the right is the other hydrogen labeled as Hydrogen 2.

Conf	Flat			Flat_down			Up		
Elem	Oxygen	Hydrogen1	Hydrogen2	Oxygen	Hydrogen1	Hydrogen2	Oxygen	Hydrogen1	Hydrogen2
Dist (Å)	3,83	3,21	3,88	4,56	3,99	4,1	4,19	4,23	5,09
	4,12	3,68	4,76	4,64	3,87	4,74	4,16	4,66	4,66
	4,5	4,7	5,18	4,61	3,75	5,22	4,22	5,12	4,27
	4,5	5,18	4,7	4,67	3,91	5,28	4,22	5,12	4,27
	4,13	4,76	3,68	4,63	4,08	4,75	4,16	4,66	4,66
	4,83	3,38	3,21	4,61	4,14	4,17	4,19	4,23	5,09
	2,93	3,11	3,11	3,49	2,55	3,63	2,96	3,64	3,64

Table 4.8: Distances between each atom from the water molecule and the seven nearest gold atoms, considering the up, the flat-down and the up configurations.

By applying these distances as the r_{ij} values in equation 3.3, and setting the force to 0, and also imposing the restrictions mentioned in Section 3.6, Mathematica used an corresponding exact system and numericized the result to compute the σ s. Then, using the adsorption energies, shown in Table 4.3 applied in Equation 2.7, as the E_{FF-LJ} , Mathematica compute a range for ϵ_H and a relationship between ϵ_H and ϵ_O as reported in Table 4.9 :

Configuration	Relation	Restriction
Flat-Down	$\epsilon_O = 2.98235 \cdot 10^{-18} \cdot (1.02266 \cdot 10^{16} - 2.54201 \cdot 10^{17} \epsilon_H)$	$0 < \epsilon_H < 0.0402305$
Flat	$\epsilon_O = 2.5149 \cdot 10^{-17} \cdot (2.42226 \cdot 10^{15} - 1.25968 \cdot 10^{17} \epsilon_H)$	$0 < \epsilon_H < 0.0192291$
Up	$\epsilon_O = 3.9386 \cdot 10^{-18} \cdot (8.46053 \cdot 10^{15} - 1.00378 \cdot 10^{18} \epsilon_H)$	$0 < \epsilon_H < 0.00842871$

Table 4.9: Relations between ϵ_H and ϵ_O for each configuration.

From this we can plot the graphs for the potential for the oxygen, the hydrogen and both together, as in Figure 4.19:

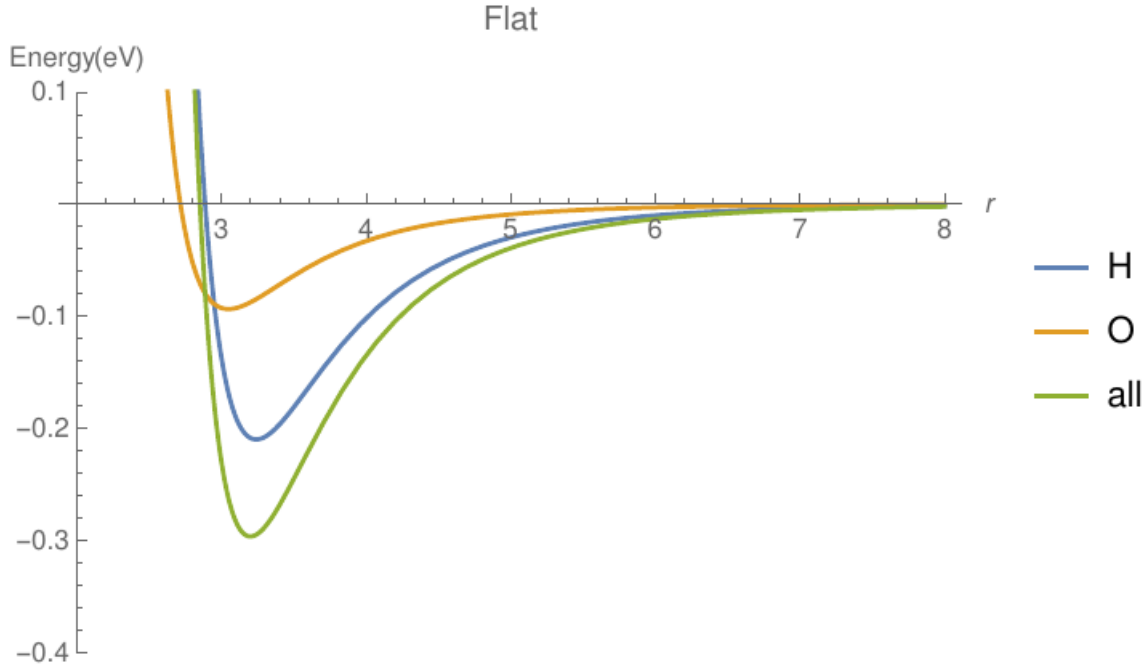


Figure 4.19: Assessment of the range of the Lennard Jones parameters with water at the flat configuration.

One of the relevant aspects that we wanted to ensure was that the force field would be capable to accurately describe the top position as the most stable adsorption site, since this is observed in the QM calculations. This can be achieved by imposing another restriction, that $\epsilon_O = 2\epsilon_H$. By doing so we calculate the values for the Van der Waals parameters for each configuration as reported in Table 4.10:

Configuration	ϵ_O (eV)	σ_O (Å)	ϵ_H (eV)	σ_H (Å)
Flat_down	0.022	3.7	0.011	2.7
Flat	0.024	3.0	0.012	3.2
Up	0.011	3.1	0.006	3.9
Ave	0.019	3.3	0.009	3.3
Err	0.007	0.4	0.003	0.6

Table 4.10: Lennard-Jones parameters for each configuration.

By imposing that $\epsilon_O = 2\epsilon_H$, the graphs from the potential energy became like in Figure 4.20

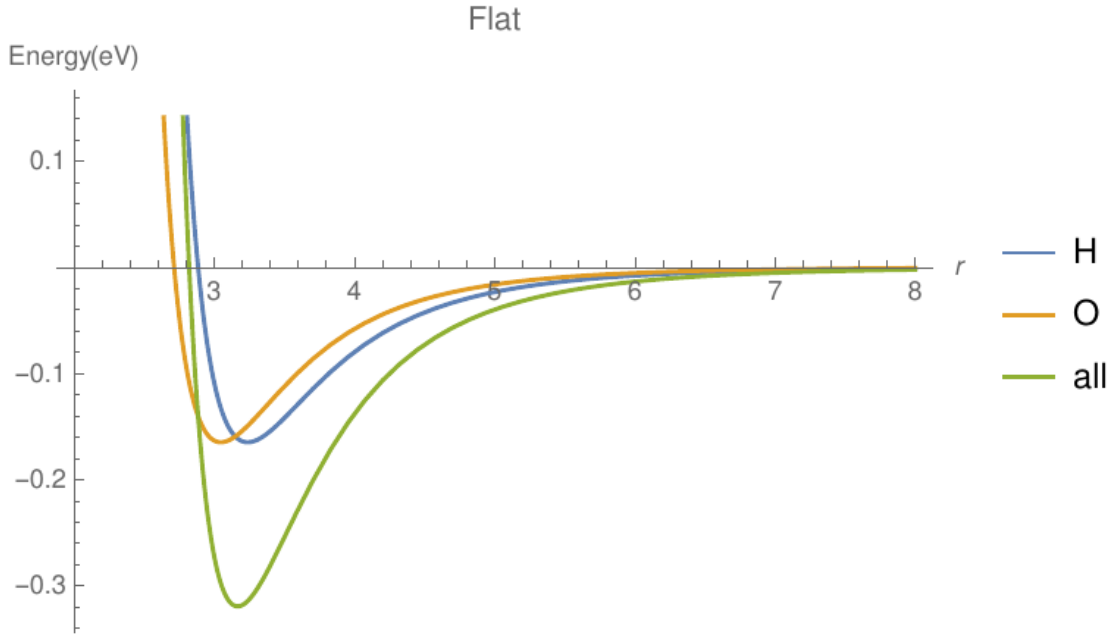


Figure 4.20: Assessment of the range of the Lennard Jones parameters with water at the flat configuration.

It is important to emphasize that, as mentioned in Section 3.6, the approach used in this Section do not accounted the electrostatic interactions, i.e. the Lennard-Jones parameters were fitted separately from the charges fitted in the previous Section. Yet, the achieved values for the averages are in good agreement with the values reported by Berg *et al.*¹²⁵

Berg¹²⁵ reported from the literature, some LJ parameters that used the same 12-6 exponents, with a modified TIP3P water model which contains an explicit interaction term for hydrogen and with a SPC water model. The case with the SPC had two references but both did not presented the σ and ϵ for the Au-H pair, so only the values for the Au-O pair could be compared. The value for the σ was 3.25 Å for both references, so a discrepancy of less than 2% with the value of our work. The values for ϵ were 0.039 eV and 0.055 eV, which are almost two and three times the value found in this work. Meanwhile for the case with the modified TIP3P water model, the σ for the Au-O pair was also in good agreement (3.41 Å, still within the range we suggested). In this case the ϵ was 0.017 eV, so was also within the error on Table 4.10. Now for the values of the Au-H pair, the ϵ was 0.010 eV and was also within the error on Table 4.10. On the other hand, the σ was 1.87 Å almost half the value achieve in our work. One hypothesis to explain this difference

is that our value comes from the average of the configurations “Flat”, “Flat-Down” and “Up”, if we also used the configuration “Down” the average could have been smaller, one perspective is to investigate the parametrization procedure used in that paper.

Berg also reported his own values, using a 12-6 LJ with a modified TIP3P water model and with a model called COMPASS. The values for the σ were 3.18 Å and 3.95 Å for the Au-O and the Au-H pair respectively. Both are within the range in Table 4.10. Yet the values for the ϵ 's were completely different, with the value for Au-O pair been overestimated while the value for the Au-H been underestimated. In the paper Berg also advocate that the LJ 12-6 had the worse parameter R^2 and that a Buckingham or Morse potential could yield better fitting. Since their parameters are different we could not compare directly.

Chapter 5

CONCLUSIONS AND PERSPECTIVES

In this work a description of the water/gold interface through a parametrized force field capable to account the polarization based on the ROD model was developed. According to the methodology described in the chapter 3, to achieve the parameters of this force field, the protocol consists of a fitting of charges of an electrostatic potential obtained from DFT calculations, followed by a fitting of the Van der Waals terms.

The configuration with lowest energy, in the case of the Au-H₂O the water at the atop adsorption site in the flat configuration, was the reference geometry used for the computation of the electrostatic potential. The configurations associated with the local minima of the potential energy surface were evaluated through an optimization procedure in the framework of DFT. The optimizations were carried out with basis sets and pseudo-potentials described in the supplementary material.

The data acquired for properties such as the lattice constant and work function of the gold slab, the geometric parameters and the dipole moment of the isolated water molecule and the adsorption parameters (energy and geometric parameters) of the water/metal interface, were analyzed to assess the quality of the description of the metal, the water and interactions at interface, respectively. All of them were in good agreement with data reported in the literature, being within a range of 11% of error from experimental data. In addition the flat configuration was verified as the configuration with lowest energy. From these results we inferred that the data from the QM simulation provided a good description for the system.

Then the electrostatic potential was computed employing the SIESTA QM/MM scheme as proposed by Sanz-Navarro *et al.*⁸⁰ and also the VNA correction was calculated to allow transferability to other codes.

For the force field to account the polarization in the metal slab, the ROD model was applied. In order to achieve an orientational average of the rods so that they produce results with physical meaning, we used a classical molecular dynamic simulation. From the average configuration we selected sites that met the criteria that indicated preferential orientation, like having a average length larger than a certain value (0.05 Å) and being associated with ions in the top layers of the slab.

Afterwards, we implemented four sets of constraints over the fitting sites, to determine which would lead to better fitting of the QM electrostatic potential. Then a fitting of charges was performed using a least squares minimization with a penalty function (RESP) method. Comparing the plots between the QM electrostatic potential and the fitted potentials, qualitatively we observed that the set of restriction “M0Same” were only the selected sites were fitted and they had the same charge while the others had null charge, could not reproduce the pattern of the QM potential. The plots also indicated that the 3x3 grid was not enough to eliminate the border effects that came from the fact that the software we used for the fitting did not accounted the periodic boundary conditions used in the QM simulation. In addition, considering the symmetry of potential, the set of restrictions “M0free” only the selected sites were fitted while the others had null charge was set which better reproduced the QM electrostatic potential.

For a quantitative assessment of the quality of the fitting, the RMS and RRMS errors were analysed to verify which set of constraints led to more accurate fitting. As expected, the set “Free” which fitted all the sites and allow for them to have any value, had the smallest errors while the set “M0Same” had the largest errors. The set “M0free” had the second smallest errors.

Analysing the average of the charges on the bottom layers of the slab, we observed that even for the set were all sites were fitted (“Free” and “Same”), this average was zero, this could indicate that the approximation of setting all sites other than the selected sites as zero, as in the sets “M0free” and “M0Same” was an appropriate ansatz. From this results we believe that the set “M0free” can provide the best parameters for the fitting of charges to reproduce the QM electrostatic potential. Later the parameters (σ_{ij} and

ϵ_{ij}) from Van der Waals were also fitted. For that we adopted an approximation, where we neglected the electrostatic contribution and evaluated just the long range dispersion interactions. Basically, we applied the distances between the atoms of the water and the seven closest neighbor atoms of gold, from the three local minima configurations we determined, in the equation for the force derived from a Lennard Jones potential with exponents 12 and 6. By finding the root of this equation we determined the σ_{ij} . Then, by using these values and the adsorption energy and imposing a restriction to guarantee the correct adsorption site, in the equation for the LJ potential, we determined some ranges for the Van der Waals parameters. The values within these ranges were in agreement with the values from similar models, reported in the literature, although not concomitantly.

With these adjusted parameters the force field is expected to be able to reproduce the surface polarization and adsorption properties of the system.

The next step would be to perform a scan within the range of the achieved Lennard Jones parameters, accounting the electrostatic contribution and compare for example the results of the adsorption energy. Or to perform a classical molecular dynamic simulation with the fitted parameters (both from the electrostatics's and the average of the LJ parameters) and check some properties of the adsorption.

Bibliography

- ¹ Ana Dobrota and Igor Pasti. Chemisorption as the essential step in electrochemical energy conversion - review. *Journal of Electrochemical Science and Engineering*, 01 2020.
- ² Luana S. Pedroza, Adrien Poissier, and M. V. Fernández-Serra. Local order of liquid water at metallic electrode surfaces. *Journal of Chemical Physics*, 142(3), 01 2015.
- ³ Matthew Pellow, Christopher Emmott, Charles Barnhart, and S. Benson. Hydrogen or batteries for grid storage? a net energy analysis. *Energy Environ. Sci.*, 8, 04 2015.
- ⁴ Alejandro Arvia and Roberto Salvarezza. An interdisciplinary approach to the electrochemistry at solid electrodes. *Journal of the Brazilian Chemical Society*, 8:91–100, 12 1996.
- ⁵ Kang Cho, Hyung-Kyu Lim, and Hyungjun Kim. Structure, dynamics, and wettability of water at metal interfaces. *Scientific Reports*, 9, 12 2019.
- ⁶ Alessandro Fortunelli, William Goddard, Luca Sementa, and Giovanni Barcaro. Optimizing the oxygen evolution reaction for electrochemical water oxidation by tuning solvent properties. *Nanoscale*, 7, 02 2015.
- ⁷ Zhuoxin Liu, Yan Huang, Yang Huang, Qi Yang, Xinliang Li, Zhaodong Huang, and Chunyi Zhi. Voltage issue of aqueous rechargeable metal-ion batteries. *Chem. Soc. Rev.*, 49:180–232, 2020.
- ⁸ Ahmed Huzayyin, Jin Hyun Chang, Keryn Lian, and Francis Dawson. Interaction of water molecule with Au(111) and Au(110) surfaces under the influence of an external electric field. *Journal of Physical Chemistry C*, 118(7):3459–3470, 02 2014.

- ⁹ Fritz Scholz. *Electrochemistry in a Divided World: Innovations in Eastern Europe in the 20th Century*. 01 2015.
- ¹⁰ B.E. Conway, O.J. Murphy, and S. Srinivasan. *Electrochemistry in Transition: From the 20th to the 21st Century*. Springer US, 2013.
- ¹¹ A.J. Bard. *Electroanalytical Chemistry: A Series of Advances*. Electroanalytical Chemistry: A Series of Advances. Taylor & Francis, 1998.
- ¹² P.G. Bruce. *Solid State Electrochemistry*. Chemistry of Solid State Materials. Cambridge University Press, 1997.
- ¹³ Vladimir Shepelin. Electrochemical mechanism in catalysis. Technical report, 03 2016.
- ¹⁴ R. Fang and J. Hauser. A theoretical analysis of the current-voltage characteristics of solar cells. Technical report, 05 1979.
- ¹⁵ E. E. van Dyk, A. R. Gxasheka, and E. L. Meyer. Monitoring current-voltage characteristics of photovoltaic modules. In *Conference Record of the Twenty-Ninth IEEE Photovoltaic Specialists Conference, 2002.*, pages 1516–1519, 05 2002.
- ¹⁶ Olle Björneholm, Martin H. Hansen, Andrew Hodgson, Li-Min Liu, David T. Limmer, Angelos Michaelides, Philipp Pedevilla, Jan Rossmeisl, Huaze Shen, Gabriele Tocci, Eric Tyrode, Marie-Madeleine Walz, Josephina Werner, and Hendrik Bluhm. Water at interfaces. *Chemical Reviews*, 116(13):7698–7726, 2016. PMID: 27232062.
- ¹⁷ A. Hodgson and Samreen Haq. Water adsorption and the wetting of metal surfaces. *Surface Science Reports*, 64:381–451, 09 2009.
- ¹⁸ David T. Limmer, Adam P. Willard, Paul Madden, and David Chandler. Hydration of metal surfaces can be dynamically heterogeneous and hydrophobic. *Proceedings of the National Academy of Sciences of the United States of America*, 110(11):4200–4205, 03 2013.
- ¹⁹ Adel M.A. Mohamed, Aboubakr M. Abdullah, and Nathalie A. Younan. Corrosion behavior of superhydrophobic surfaces: A review. *Arabian Journal of Chemistry*, 8(6):749 – 765, 2015.

- ²⁰ Louise J. Criscenti, Randall T. Cygan, Ara S. Kooser, and Harold K. Moffat. Water and halide adsorption to corrosion surfaces: Molecular simulations of atmospheric interactions with aluminum oxyhydroxide and gold. *Chemistry of Materials*, 20(14):4682–4693, 2008.
- ²¹ Nuria Garcia-Araez, Paramaconi Rodriguez, Violeta Navarro, Huib J. Bakker, and Marc T.M. Koper. Structural effects on water adsorption on gold electrodes. *Journal of Physical Chemistry C*, 115(43):21249–21257, 11 2011.
- ²² V. Matolín, I. Matolínová, F. Dvořák, V. Johánek, J. Mysliveček, K.C. Prince, T. Skála, O. Stetsovykh, N. Tsud, M. Václavů, and B. Šmíd. Water interaction with ceo2(111)/cu(111) model catalyst surface. *Catalysis Today*, 181(1):124 – 132, 2012. Frigyes Solymosi’s special issue Planar Model System and Heterogeneous Catalysis.
- ²³ Sebastian Schnur and Axel Groß. Properties of metal-water interfaces studied from first principles. *New Journal of Physics*, 11, 12 2009.
- ²⁴ Roger Nadler and Javier Fdez Sanz. Effect of dispersion correction on the Au(1 1 1)-H₂O interface: A first-principles study. *Journal of Chemical Physics*, 137(11), 9 2012.
- ²⁵ A. Michaelides, V. A. Ranea, P. L. de Andres, and D. A. King. General Model for Water Monomer Adsorption on Close-Packed Transition and Noble Metal Surfaces. *Physical Review Letters*, 90(21):4, 2003.
- ²⁶ haijun pan, Xiangying Meng, and Gaowu Qin. Hydrogen generation by water splitting on hematite (0001) surfaces: First-principles calculations. *Phys. Chem. Chem. Phys.*, 16, 10 2014.
- ²⁷ Jian Feng Li, Yi Fan Huang, Sai Duan, Ran Pang, De Yin Wu, Bin Ren, Xin Xu, and Zhong Qun Tian. SERS and DFT study of water on metal cathodes of silver, gold and platinum nanoparticles. *Physical Chemistry Chemical Physics*, 12(10):2493–2502, 03 2010.
- ²⁸ Patricia A. Thiel and Theodore E. Madey. The interaction of water with solid surfaces: Fundamental aspects. *Surface Science Reports*, 7(6):211 – 385, 1987.
- ²⁹ Michael A. Henderson. The interaction of water with solid surfaces: fundamental aspects revisited. *Surface Science Reports*, 46(1):1 – 308, 2002.

- ³⁰ G. Cicero, A. Calzolari, S. Corni, and A. Catellani. Anomalous wetting layer at the Au(111) surface. *Journal of Physical Chemistry Letters*, 2(20):2582–2586, 10 2011.
- ³¹ Maria Fyta. Classical potentials and force fields. In *Computational Approaches in Physics*, 2053-2571, pages 4–1 to 4–15. Morgan & Claypool Publishers, 2016.
- ³² Hendrik Heinz, R. A. Vaia, B. L. Farmer, and R. R. Naik. Accurate simulation of surfaces and interfaces of face-centered cubic metals using 12-6 and 9-6 lennard-jones potentials. *Journal of Physical Chemistry C*, 112(44):17281–17290, 11 2008.
- ³³ Stephan N. Steinmann, Rodrigo Ferreira De Moraes, Andreas W. Götz, Paul Fleurat-Lessard, Marcella Iannuzzi, Philippe Sautet, and Carine Michel. Force Field for Water over Pt(111): Development, Assessment, and Comparison. *Journal of Chemical Theory and Computation*, 14(6):3238–3251, jun 2018.
- ³⁴ Thomas S. Hofer and Andreas O. Tirlir. Combining 2d-Periodic Quantum Chemistry with Molecular Force Fields: A Novel QM/MM Procedure for the Treatment of Solid-State Surfaces and Interfaces. *Journal of Chemical Theory and Computation*, 11(12):5873–5887, 10 2015.
- ³⁵ Muhammad Faheem and Andreas Heyden. Hybrid quantum mechanics/molecular mechanics solvation scheme for computing free energies of reactions at metal-water interfaces. *Journal of Chemical Theory and Computation*, 10(8):3354–3368, 08 2014.
- ³⁶ Cameron J. Bodenschatz, Sapna Sarupria, and Rachel B. Getman. Molecular-level details about liquid H₂O interactions with CO and sugar alcohol adsorbates on Pt(111) calculated using density functional theory and molecular dynamics. *Journal of Physical Chemistry C*, 119(24):13642–13651, 05 2015.
- ³⁷ A. Warshel and M. Levitt. Theoretical studies of enzymic reactions: Dielectric, electrostatic and steric stabilization of the carbonium ion in the reaction of lysozyme. *Journal of Molecular Biology*, 103(2):227–249, 1976.
- ³⁸ Gerrit Groenhof. Introduction to qm/mm simulations. *Methods in molecular biology (Clifton, N.J.)*, 924:43–66, 01 2013.
- ³⁹ P. Hohenberg and W. Kohn. Inhomogeneous electron gas. *Phys. Rev.*, 136:B864–B871, 11 1964.

- ⁴⁰ W. Kohn and L. J. Sham. Self-consistent equations including exchange and correlation effects. *Phys. Rev.*, 140:A1133–A1138, 11 1965.
- ⁴¹ Rafael L.H. Freire, Diego Guedes-Sobrinho, Adam Kiejna, and Juarez L.F. Da Silva. Comparison of the Performance of van der Waals Dispersion Functionals in the Description of Water and Ethanol on Transition Metal Surfaces. *Journal of Physical Chemistry C*, 122(3):1577–1588, 01 2018.
- ⁴² Masumeh Foroutan, Mehdi Darvishi, and S. Mahmood Fatemi. Structural and dynamical characterization of water on the Au (100) and graphene surfaces: A molecular dynamics simulation approach. *Physical Review E*, 96(3), 09 2017.
- ⁴³ Gerald I. Kerley. On corrections to the born-oppenheimer approximation, 2013.
- ⁴⁴ J. R. Trail and R. J. Needs. Shape and energy consistent pseudopotentials for correlated electron systems. *The Journal of Chemical Physics*, 146(20):204107, 2017.
- ⁴⁵ Aron Cohen, Paula Mori-Sánchez, and Weitao Yang. Insights into current limitations of density functional theory. *Science (New York, N.Y.)*, 321:792–4, 09 2008.
- ⁴⁶ Jiří Klimeš, David R Bowler, and Angelos Michaelides. Chemical accuracy for the van der waals density functional. *Journal of Physics: Condensed Matter*, 22(2):022201, 12 2009.
- ⁴⁷ Sándor Kristyán and Péter Pulay. Can (semi)local density functional theory account for the london dispersion forces? *Chemical Physics Letters*, 229(3):175 – 180, 1994.
- ⁴⁸ Axel D. Becke. Perspective: Fifty years of density-functional theory in chemical physics. *The Journal of Chemical Physics*, 140(18):18A301, 2014.
- ⁴⁹ W. Koch and M. C. Holthausen. *A Chemist’s Guide to Density Functional Theory*. Wiley - VCH, Weinheim - New York, 2nd edition, 2001.
- ⁵⁰ Robert G. Parr and Weitao Yang. *Density-Functional Theory of Atoms and Molecules (International Series of Monographs on Chemistry)*. Oxford University Press, USA, 1994.
- ⁵¹ Klaus Capelle. A bird’s-eye view of density-functional theory. *Brazilian Journal of Physics*, 36:1318 – 1343, 12 2006.

- ⁵² Zhi-Jian Zhao and Jinlong Gong. Chapter 14 - uncertainties in theoretical description of well-defined heterogeneous catalysts. In Paolo Fornasiero and Matteo Cargnello, editors, *Morphological, Compositional, and Shape Control of Materials for Catalysis*, volume 177 of *Studies in Surface Science and Catalysis*, pages 541 – 565. Elsevier, 2017.
- ⁵³ Mark T. Lusk and Ann E. Mattsson. High-performance computing for materials design to advance energy science. *MRS Bulletin*, 36(3):169–174, 03 2011.
- ⁵⁴ M. Schlesinger. *Modelling and Numerical Simulations II*. Modern Aspects of Electrochemistry. Springer New York, 2009.
- ⁵⁵ R. Catlow, C.R.A. Catlow, and E.A. Kotomin. *Computational Materials Science*. NATO Science Series: Computer and systems sciences. IOS Press, 2003.
- ⁵⁶ M. Fuchs, M. Bockstedte, E. Pehlke, and M. Scheffler. Pseudopotential study of binding properties of solids within generalized gradient approximations: The role of core-valence exchange correlation. *Physical Review B - Condensed Matter and Materials Physics*, 57(4):2134–2145, 1998.
- ⁵⁷ Ales Zupan, Kieron Burke, M. Ernzerhof, and John Perdew. Distributions and averages of electron density parameters: Explaining the effects of gradient corrections. *J. Chem. Phys.*, 106:10184–10193, 06 1997.
- ⁵⁸ John Perdew, Matthias Ernzerhof, Ales Zupan, and Kieron Burke. Nonlocality of the density functional for exchange and correlation: Physical origins and chemical consequences. *J. Chem. Phys.*, 108:1522–1531, 01 1998.
- ⁵⁹ Joel Ireta, Jörg Neugebauer, and Matthias Scheffler. On the accuracy of DFT for describing hydrogen bonds: Dependence on the bond directionality. *Journal of Physical Chemistry A*, 108(26):5692–5698, 06 2004.
- ⁶⁰ D. R. Hamann. H_2O hydrogen bonding in density-functional theory. *Phys. Rev. B*, 55:R10157–R10160, 04 1997.
- ⁶¹ Christopher J. Cramer and Donald G. Truhlar. Density functional theory for transition metals and transition metal chemistry. *Physical Chemistry Chemical Physics*, 11(46):10757–10816, 2009.

- ⁶² Javier Carrasco, Jiří Klimeš, and Angelos Michaelides. The role of van der waals forces in water adsorption on metals. *The Journal of Chemical Physics*, 138(2):024708, 2013.
- ⁶³ Isidro Lorenzo Geadá, Hadi Ramezani-Dakhel, Tariq Jamil, Marialore Sulpizi, and Hendrik Heinz. Insight into induced charges at metal surfaces and biointerfaces using a polarizable Lennard-Jones potential. *Nature Communications*, 9(1), 12 2018.
- ⁶⁴ Timo Jacob and William A. Goddard. Agostic interactions and dissociation in the first layer of water on Pt(111). *Journal of the American Chemical Society*, 126(30):9360–9368, 08 2004.
- ⁶⁵ Felix O. Kannemann and Axel D. Becke. Van der waals interactions in density-functional theory: Rare-gas diatomics. *Journal of Chemical Theory and Computation*, 5(4):719–727, 2009. PMID: 26609577.
- ⁶⁶ Juarez Da Silva, Catherine Stampfl, and Matthias Scheffler. Adsorption of xe atoms on metal surfaces: New insights from first-principles calculations. *Physical review letters*, 90:066104, 03 2003.
- ⁶⁷ James Benigna. Photoelectron spectroscopy in advanced placement chemistry. *Journal of Chemical Education*, 91(9):1299–1305, 2014.
- ⁶⁸ A. D. Becke and K. E. Edgecombe. A simple measure of electron localization in atomic and molecular systems. *The Journal of Chemical Physics*, 92(9):5397–5403, 1990.
- ⁶⁹ Richard M. Martin. *Electronic Structure: Basic Theory and Practical Methods*. Cambridge University Press, 2004.
- ⁷⁰ Peter Schwerdtfeger. The pseudopotential approximation in electronic structure theory. *ChemPhysChem*, 12(17):3143–3155, 2011.
- ⁷¹ Kevin F. Garrity, Joseph W. Bennett, Karin M. Rabe, and David Vanderbilt. Pseudopotentials for high-throughput DFT calculations. *Computational Materials Science*, 81:446–452, 2014.
- ⁷² J. R. Trail and R. J. Needs. Norm-conserving Hartree-Fock pseudopotentials and their asymptotic behavior. *Journal of Chemical Physics*, 122(1), 2005.

- ⁷³ V. Milman, B. Winkler, J. A. White, C. J. Pickard, M. C. Payne, E. V. Akhmatkaya, and R. H. Nobes. Electronic Structure, Properties, and Phase Stability of Inorganic Crystals: A Pseudopotential Plane-Wave Study. *International Journal of Quantum Chemistry*, 77(5):895–910, 2000.
- ⁷⁴ G. B. Bachelet, D. R. Hamann, and M. Schlüter. Pseudopotentials that work: From h to pu. *Phys. Rev. B*, 26:4199–4228, 10 1982.
- ⁷⁵ Martin Kiffner, Dieter Jaksch, and Davide Ceresoli. A polynomial ansatz for norm-conserving pseudopotentials. *Journal of Physics Condensed Matter*, 30(27), 06 2018.
- ⁷⁶ David Vanderbilt. Soft self-consistent pseudopotentials in a generalized eigenvalue formalism. *Phys. Rev. B*, 41:7892–7895, 04 1990.
- ⁷⁷ D. R. Hamann, M. Schlüter, and C. Chiang. Norm-conserving pseudopotentials. *Phys. Rev. Lett.*, 43:1494–1497, 11 1979.
- ⁷⁸ James R Chelikowsky. The pseudopotential-density functional method applied to nanostructures. *Journal of Physics D: Applied Physics*, 33(8):R33–R50, 03 2000.
- ⁷⁹ N. Troullier and JoséLuís Martins. A straightforward method for generating soft transferable pseudopotentials. *Solid State Communications*, 74(7):613–616, 1990.
- ⁸⁰ Carlos F. Sanz-Navarro, Rogeli Grima, Alberto García, Edgar A. Bea, Alejandro Soba, J. M. Cela, and Pablo Ordejón. An efficient implementation of a QM-MM method in SIESTA. *Theoretical Chemistry Accounts*, 128(4):825–833, 02 2011.
- ⁸¹ Alejandro Crespo, Damián A. Scherlis, Marcelo A. Martí, Pablo Ordejón, Adrián E. Roitberg, and Darío A. Estrin. A dft-based qm-mm approach designed for the treatment of large molecular systems: Application to chorismate mutase. *The Journal of Physical Chemistry B*, 107(49):13728–13736, 2003.
- ⁸² Nicolas Ferré, Xavier Assfeld, and Jean Louis Rivail. Specific force field parameters determination for the hybrid ab initio QM/MM LSCF method. *Journal of Computational Chemistry*, 23(6):610–624, 04 2002.
- ⁸³ F. Iori and S. Corni. Including image charge effects in the molecular dynamics simulations of molecules on metal surfaces. *Journal of Computational Chemistry*, 29(10):1656–1666, 06 2008.

- ⁸⁴ J. Ilja Siepmann and Michiel Sprik. Influence of surface topology and electrostatic potential on water/electrode systems. *The Journal of Chemical Physics*, 102(1):511–524, 1995.
- ⁸⁵ F. Iori, R. Di Felice, E. Molinari, and S. Corni. GolP: An atomistic force-field to describe the interaction of proteins with Au(111) surfaces in water. *Journal of Computational Chemistry*, 30(9):1465–1476, jul 2009.
- ⁸⁶ William Humphrey, Andrew Dalke, and Klaus Schulten. Vmd: Visual molecular dynamics. *Journal of Molecular Graphics*, 14(1):33 – 38, 1996.
- ⁸⁷ Anton Kokalj. Xcrysden—a new program for displaying crystalline structures and electron densities. *Journal of Molecular Graphics and Modelling*, 17(3):176 – 179, 1999.
- ⁸⁸ Marcus Hanwell, Donald Curtis, David Lonie, Tim Vandermeersch, Eva Zurek, and Geoffrey Hutchison. Avogadro: an advanced semantic chemical editor, visualization, and analysis platform. *Journal of cheminformatics*, 4:17, 08 2012.
- ⁸⁹ U. Chandra Singh and Peter A. Kollman. An approach to computing electrostatic charges for molecules. *Journal of Computational Chemistry*, 5(2):129–145, 1984.
- ⁹⁰ Brent H. Besler, Kenneth M. Merz Jr., and Peter A. Kollman. Atomic charges derived from semiempirical methods. *Journal of Computational Chemistry*, 11(4):431–439, 1990.
- ⁹¹ Christopher I. Bayly, Piotr Cieplak, Wendy D. Cornell, and Peter A. Kollman. A well-behaved electrostatic potential based method using charge restraints for deriving atomic charges: The RESP model. *Journal of Physical Chemistry*, 97(40):10269–10280, 1993.
- ⁹² Junmei Wang, Piotr Cieplak, and Peter A. Kollman. How well does a restrained electrostatic potential (resp) model perform in calculating conformational energies of organic and biological molecules? *Journal of Computational Chemistry*, 21(12):1049–1074, 2000.

- ⁹³ Wendy D Cornell, Piotr Cieplak, Christopher I Bayly, and Peter A Kollman. Application of RESP charges to calculate conformational energies, hydrogen bond energies, and free energies of solvation. *J. Am. Chem. soc.*, 115(7):9620–9631, 1993.
- ⁹⁴ Daniela Damasceno, Euclides Mesquita, and Nimal Rajapakse. Mechanical behavior of nano structures using atomic-scale finite element method (afem). *Latin American Journal of Solids and Structures*, 14:2046–2066, 01 2017.
- ⁹⁵ J E Lennard-Jones. Cohesion. *Proceedings of the Physical Society*, 43(5):461–482, sep 1931.
- ⁹⁶ David A. Pearlman, David A. Case, James W. Caldwell, Wilson S. Ross, Thomas E. Cheatham, Steve DeBolt, David Ferguson, George Seibel, and Peter Kollman. Amber, a package of computer programs for applying molecular mechanics, normal mode analysis, molecular dynamics and free energy calculations to simulate the structural and energetic properties of molecules. *Computer Physics Communications*, 91(1):1 – 41, 1995.
- ⁹⁷ A. D. MacKerell, D. Bashford, M. Bellott, R. L. Dunbrack, J. D. Evanseck, M. J. Field, S. Fischer, J. Gao, H. Guo, S. Ha, D. Joseph-McCarthy, L. Kuchnir, K. Kuczera, F. T. K. Lau, C. Mattos, S. Michnick, T. Ngo, D. T. Nguyen, B. Prodhom, W. E. Reiher, B. Roux, M. Schlenkrich, J. C. Smith, R. Stote, J. Straub, M. Watanabe, J. Wiórkiewicz-Kuczera, D. Yin, and M. Karplus. All-atom empirical potential for molecular modeling and dynamics studies of proteins. *The Journal of Physical Chemistry B*, 102(18):3586–3616, 1998. PMID: 24889800.
- ⁹⁸ Pnina Dauber-Osguthorpe, Victoria A. Roberts, David J. Osguthorpe, Jon Wolff, Monique Genest, and Arnold T. Hagler. Structure and energetics of ligand binding to proteins: Escherichia coli dihydrofolate reductase-trimethoprim, a drug-receptor system. *Proteins: Structure, Function, and Bioinformatics*, 4(1):31–47, 1988.
- ⁹⁹ William L. Jorgensen, David S. Maxwell, and Julian Tirado-Rives. Development and testing of the opls all-atom force field on conformational energetics and properties of organic liquids. *Journal of the American Chemical Society*, 118(45):11225–11236, 1996.
- ¹⁰⁰ Fritz London. Zur theorie und systematik der molekularkräfte. *Zeitschrift für Physik*, 63(3-4):245–279, 1930.

- ¹⁰¹ P.W. Atkins and J. De Paula. *Atkins' Physical Chemistry*. Macmillan Higher Education, 2006.
- ¹⁰² Václav Bazgier, Karel Berka, Michal Otyepka, and Pavel Banáš. Exponential repulsion improves structural predictability of molecular docking. *Journal of Computational Chemistry*, 37(28):2485–2494, 2016.
- ¹⁰³ R. P. Feynman. Forces in molecules. *Phys. Rev.*, 56:340–343, 08 1939.
- ¹⁰⁴ Daniel Sánchez-Portal, Pablo Ordejón, Emilio Artacho, and José M. Soler. Density-functional method for very large systems with lcao basis sets. *International Journal of Quantum Chemistry*, 65(5):453–461, 1997.
- ¹⁰⁵ José M Soler, Emilio Artacho, Julian D Gale, Alberto García, Javier Junquera, Pablo Ordejón, and Daniel Sánchez-Portal. The SIESTA method for ab initio order-n materials simulation. *Journal of Physics: Condensed Matter*, 14(11):2745–2779, 03 2002.
- ¹⁰⁶ William L. Jorgensen, Jayaraman Chandrasekhar, Jeffrey D. Madura, Roger W. Impey, and Michael L. Klein. Comparison of simple potential functions for simulating liquid water. *The Journal of Chemical Physics*, 79(2):926–935, 1983.
- ¹⁰⁷ Javier Junquera, Magali Zimmer, Pablo Ordejón, and Philippe Ghosez. First-principles calculation of the band offset at BaO/BaTiO_3 and SrO/SrTiO_3 interfaces. *Phys. Rev. B*, 67:155327, Apr 2003.
- ¹⁰⁸ Daniel R. Roe and Thomas E. Cheatham. Ptraj and cpptraj: Software for processing and analysis of molecular dynamics trajectory data. *Journal of Chemical Theory and Computation*, 9(7):3084–3095, 2013. PMID: 26583988.
- ¹⁰⁹ Wolfram Research, Inc. Mathematica, Version 12.1. Champaign, IL, 2020.
- ¹¹⁰ Ruiyuan Tian, Nolito Alcala, Steven O'Neill, Dominik Horvath, Joao Coelho, Aideen Griffin, Yan Zhang, Valeria Nicolosi, Colm O'Dwyer, and Jonathan Coleman. Quantifying the effect of electronic conductivity on the rate-performance of nanocomposite battery electrodes. *ACS Applied Energy Materials*, 01 2020.
- ¹¹¹ P. Schmuki and S. Virtanen. *Electrochemistry at the Nanoscale*. Nanostructure Science and Technology. Springer New York, 2009.

- ¹¹² A. Moncmanová. *Environmental Deterioration of Materials*. Advances in Architecture. WIT Press, 2007.
- ¹¹³ Ruiqiu Liu. Adsorption and dissociation of H₂O on Au(111) surface: A DFT study. *Computational and Theoretical Chemistry*, 1019(1):141–145, 09 2013.
- ¹¹⁴ Kasper P. Kepp. A quantitative scale of oxophilicity and thiophilicity. *Inorganic Chemistry*, 55(18):9461–9470, 2016. PMID: 27580183.
- ¹¹⁵ Eugene S. Kryachko. Gold in hydrogen bonding motif-fragments of essay. In Nino Russo, Victor Ya. Antonchenko, and Eugene S. Kryachko, editors, *Self Organization of Molecular Systems*, pages 315–334, Dordrecht, 2009. Springer Netherlands.
- ¹¹⁶ Vinayak Keshavlal Patel. *Lattice constants, thermal expansion coefficients, densities, and imperfections in gold and the alpha-phase of the gold-indium system*. PhD thesis, Missouri University of Science and Technology, 1967.
- ¹¹⁷ G. V. Hansson and S. A. Flodström. Photoemission study of the bulk and surface electronic structure of single crystals of gold. *Physical Review B*, 18(4):1572–1585, 1978.
- ¹¹⁸ Luana S. Pedroza and Antônio J.R. Da Silva. Adiabatic intramolecular movements for water systems. *Journal of Chemical Physics*, 128(10), 2008.
- ¹¹⁹ J.M. Berg, J.L. Tymoczko, and L. Stryer. *Biochemistry, Fifth Edition*. W.H. Freeman, 2002.
- ¹²⁰ Daniel Elton. *Understanding the Dielectric Properties of Water*. PhD thesis, Stony Brook University, 12 2016.
- ¹²¹ W. S. Benedict, N. Gailar, and Earle K. Plyler. Rotation-vibration spectra of deuterated water vapor. *The Journal of Chemical Physics*, 24(6):1139–1165, 1956.
- ¹²² Shepard A. Clough, Yardley Beers, Gerald P. Klein, and Laurence S. Rothman. Dipole moment of water from stark measurements of h₂o, hdo, and d₂o. *The Journal of Chemical Physics*, 59(5):2254–2259, 1973.
- ¹²³ Marta Rosa, Rosa Di Felice, and Stefano Corni. Adsorption Mechanisms of Nucleobases on the Hydrated Au(111) Surface. *Langmuir*, 34(49):14749–14756, 12 2018.

- ¹²⁴ S. Kandoi, Amit Gokhale, Lars Grabow, J.A. Dumesic, and M. Mavrikakis. Why au and cu are more selective than pt for preferential oxidation of co at low temperature. *Catalysis Letters*, 93:93–100, 03 2004.
- ¹²⁵ Andrej Berg, Christine Peter, and Karen Johnston. Evaluation and Optimization of Interface Force Fields for Water on Gold Surfaces. *Journal of Chemical Theory and Computation*, 13(11):5610–5623, nov 2017.
- ¹²⁶ G P Kerker. Non-singular atomic pseudopotentials for solid state applications. *Journal of Physics C: Solid State Physics*, 13(9):L189–L194, 03 1980.
- ¹²⁷ David Vanderbilt. Optimally smooth norm-conserving pseudopotentials. *Physical Review B*, 32(12):8412–8415, 1985.
- ¹²⁸ Philipp Haas, Fabien Tran, and Peter Blaha. Calculation of the lattice constant of solids with semilocal functionals. *Physical Review B - Condensed Matter and Materials Physics*, 79(8), 02 2009.
- ¹²⁹ Beate Paulus and Krzysztof Rosciszewski. Hartree–fock ground-state properties for the group 1 alkali metals and the group 11 noble metals. *Journal of Physics: Condensed Matter*, 19(34):346217, jul 2007.
- ¹³⁰ Cheng Lin, Guili Yin, and Yongqing Zhao. Calculation of the cohesive energy of solids with the use of valence electron structure parameters. *Computational Materials Science*, 101:168 – 174, 2015.
- ¹³¹ Rajeev Ahuja, Sandeep Rekhi, and Börje Johansson. Theoretical prediction of a phase transition in gold. *Phys. Rev. B*, 63:212101, Apr 2001.
- ¹³² Charles Kittel. *Introduction to Solid State Physics*. Wiley, 8 edition, 2004.
- ¹³³ Cheng Wang, Huiyuan Wang, Tianlong Huang, Xuena Xue, Feng Qiu, and Qi-Chuan Jiang. Generalized-stacking-fault energy and twin-boundary energy of hexagonal close-packed au: A first-principles calculation. *Scientific Reports*, 5:10213, 05 2015.
- ¹³⁴ K. Kambe. Cohesive energy of noble metals. *Phys. Rev.*, 99:419–422, Jul 1955.

Chapter 6

SUPPLEMENTARY INFORMATION

6.1 Localized basis set description

SIESTA uses localized basis set for the expansion of Kohn-Sham orbitals. The atomic orbitals adopts the separation of the wave-functions in the radial part and the spherical harmonics:

$$\phi_{lmn}(\vec{r}) = R_{ln}(|\vec{r}_I|)Y_{lm}\left(\frac{\vec{r}_I}{|\vec{r}_I|}\right) \quad (6.1)$$

Towards the solution of radial part, SIESTA uses the exchange-correlation and pseudo-potential to find the numerical solution of the Kohn-Sham Hamiltonian:

$$\left(-\frac{1}{2r}\frac{d^2}{dr^2}r + \frac{l(l+1)}{2r^2} + V_l(r)\right)R_l(r) = \epsilon_l R_l(r) \quad (6.2)$$

The cutoff radius, in Bohr, of each “zeta” representing the radial part of the atomic orbitals for each atom of the system are reported in Tables 6.1 to 6.3:

Au					
n;l_zeta	6s_ζ1	6s_ζ2	5d_ζ1	5d_ζ2	6p_ζ1+
r_c (Bohr)	9.075	5.787	6.557	2.874	9.075

Table 6.1: Cutoff radius of each “zeta” representing the radial part of the atomic orbitals of gold atoms.

O					
n;l_zeta	2s_z1	2s_z2	2p_z1	2p_z2	3d_z1
r_c (Bohr)	4.508	2.641	6.150	2.594	3.544

Table 6.2: Cutoff radius of each “zeta” representing the radial part of the atomic orbitals of oxygen atoms.

H			
n;l_zeta	1s_z1	1s_z2	2p_z1
r_c (Bohr)	4.204	1.844	3.528

Table 6.3: Cutoff radius of each “zeta” representing the radial part of the atomic orbitals of hydrogen atoms.

6.2 Pseudo-potential

Troullier and Martins scheme⁷⁹ was developed in late 80’s and early 90’s, and it was based on Kerker’s method¹²⁶ of generating soft pseudo-potentials. In order to enhance softness¹²⁷ and simultaneously adequate the behaviour of radial part of the wavefunction, so that it does not have a cusp at the origin nor a kink at the core radius, which would generate high momentum oscillations in the Fourier transform of the pseudo-potential, Troullier-Martin pseudo-potential has a form that encompass a high (eighth) degree polynomial $p(r)$, see Equation 6.3:

$$R_l^{PP}(r) = \begin{cases} R_l^{AE}(r), & \text{if } r \geq r_{cl}, \\ r^l \cdot e^{p(r)}, & \text{if } r \leq r_{cl}. \end{cases} \quad (6.3)$$

Where R_l^{PP} and R_l^{AE} are the radial part of the wavefunction of the orbital with angular momentum l , considering the pseudo-potential and the all electrons, respectively, and r_{cl} is an arbitrary chosen core radius. The nine coefficients of Troullier-Martins’s polynomial are determined from criteria concerning for instance continuity of derivatives and analyticity of the pseudo-potential. One can solve the equations of most of the criteria by means of numerical quadrature and differentiation, along with Gauss-Jordan elimination, but more robust methods are implemented for conservation of charge (bisection) and for zero curvature at the origin (regula fars).⁷⁹

It is worth mentioning that even satisfying all nine criteria, a pseudo-potential still could be hard, if it uses too many parameters,⁷⁹ therefore the Troullier-Martins pseudo-potential was insightful by limiting to those nine variables.

6.2.1 Pseudo-potential description

The cutoff radius of each valence orbitals of the elements is described below.

For gold:

6s 1.00 r = 2.32/

6p 0.50 r = 2.29/

5d 9.50 r = 2.24/

5f 0.00 r = 2.00/

For oxygen:

2s 2.00 r = 1.14/

2p 4.00 r = 1.14/

3d 0.00 r = 1.14/

4f 0.00 r = 1.14/

For hydrogen:

1s 1.00 r = 1.25/

2p 0.00 r = 1.25/

3d 0.00 r = 1.25/

4f 0.00 r = 1.25/

6.3 Results - Slab properties

6.3.1 Lattice Parameter

The lattice constant and the bulk modulus of gold were determined by computing the total energy E for several values of volume of gold FCC unit cell. See Figure 6.1:

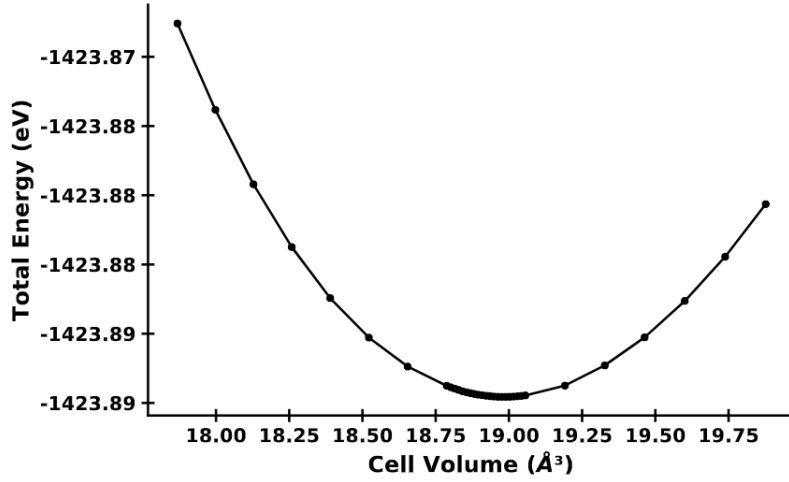


Figure 6.1: Plot of total energies vs cell volume fitted to a Murnaghan equation of state in order to evaluate Au lattice constant.

It is worth mentioning that since absolute energies depend upon the pseudo-potential used, only energy differences are physically relevant, therefore one should consider the pattern of curve not the values of total energy. These data were then fitted to an analytical form, the Murnaghan's equation of state, see Equation 6.4:

$$E(\Omega) = E_0 + \frac{B_0 \Omega}{B'_0} \left[\left(\frac{\Omega_0}{\Omega} \right)^{B'_0} + 1 \right] - \frac{\Omega_0 B_0}{B'_0 - 1} \quad (6.4)$$

Where $E(\Omega)$ means the total energy, B_0 is the modulus of incompressibility (bulk modulus) and B'_0 its first derivative with respect to the pressure, both measured at ambient pressure and Ω is the volume.

The minimum in the plot was the predicted equilibrium volume, from which the lattice constant and the bulk modulus were retrieved.

Considering the literature on the subject, Haas et al.¹²⁸ reported many values for the lattice constant of gold calculated using different functionals (LDA, SOGGA, WC, PBEsol, AM05, TPSS and PBE) and also an experimental measure. In addition Patel¹¹⁶ also reported an empirical data (here designated as Exp).

A brief comment is that we decided to show the experimental value from Patel,¹¹⁶ it is very close to the value from Haas.¹²⁸ According to the respective article, the latter data has a correction for the zero-point anharmonic expansion (ZPAE). This means that the value from thermal corrections (entropy contribution,...) was computed, so it can be directly compared with the ground state data from DFT, while the Exp2 data do not account this correction, and it's bigger lattice constant may be due to the fact that came

from a average from data collected from 288.15 K to 338.15 K.

In this work the lattice constant of gold was evaluated as 4.23 Å, in quantitative agreement (discrepancies do not exceed 5% absolute error) with the previously mentioned values obtained from calculations carried out with different exchange correlation functionals reported by Haas¹²⁸ (including also the PBE), wave-function methods and experimental data as shown in figure 6.2.

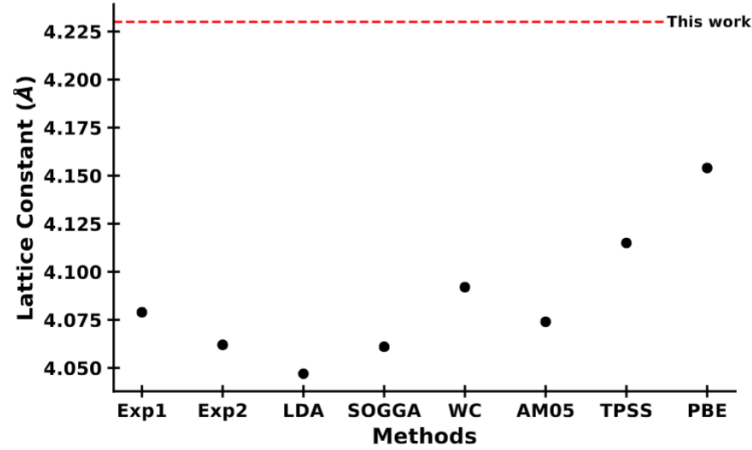


Figure 6.2: Comparison between determined lattice constant of gold. Dots represents values obtained using different functionals (LDA, SOGGA, WC, PBEsol, AM05, TPSS and PBE) reported by Haas et al.¹²⁸ and experimental values reported by Haas et al.¹²⁸(Exp1) and by Patel¹¹⁶ (Exp2). Dashed lines indicates the values calculated in this work using PBE functional.

Considering a method of lower level of theory, in this case a Hartree-Fock¹²⁹ with and without counterpoise correction (to adjust the cohesive energy) this work's value is closer to the experimental, but comparing to the empirical electron theory (EET(SCBLD))¹³⁰ the latter is closer to the experimental.

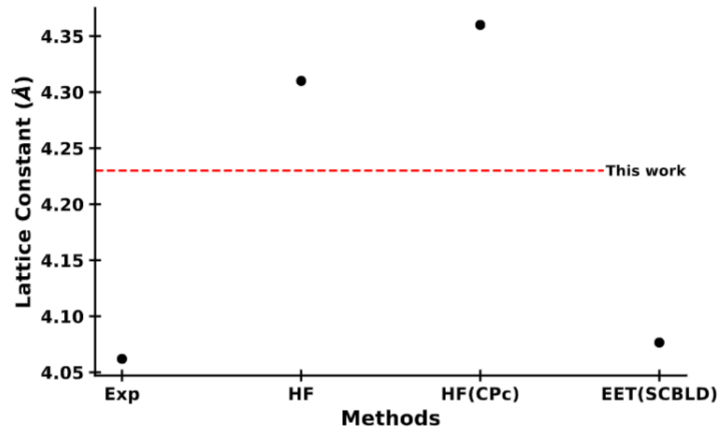


Figure 6.3: Comparison between determined lattice constant of gold. Dots represents values obtained using Hartree-Fock and experimental value reported by Haas et al.¹²⁸ and also a value from empirical electron theory. Dashed lines indicates the values calculated in this work using PBE functional.

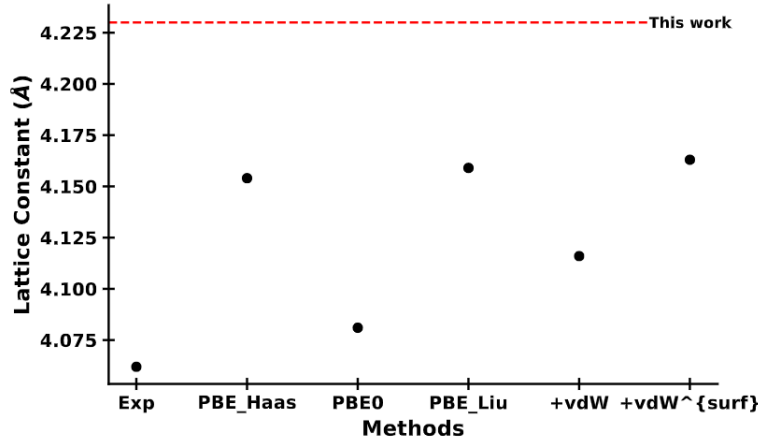


Figure 6.4: Comparison between determined lattice constant of gold. Dots represents values obtained using different functionals (LDA, SOGGA, WC, PBEsol, AM05, TPSS and PBE) reported by Haas et al.¹²⁸ and experimental values reported by Haas et al.¹²⁸(Exp1) and by Patel¹¹⁶ (Exp2). Dashed lines indicates the values calculated in this work using PBE functional.

The first observation is that comparing with other DFT exchange correlation functionals, this result follows the trend of PBE functional to over estimate the lattice constant. The difference with the PBE reported by Haas¹²⁸ is probably due to the influence of the basis set, cut-off energy and pseudo-potential in the equilibrium volume. From previous investigations, the basis set might be the dominant contribution to offset the gap observed between computed and experimental data. To a certain point, a basis set with higher cutoff radii will produce a greater lattice constant.

6.3.2 Bulk Modulus

Also derived from the curve from figure 6.2, the bulk modulus was calculated applying equation 6.4.

The bulk modulus is 116.20 GPa. This value is almost 30% below the experimental value reported of 167 ± 5 GPa.¹³¹ This poor result was expected since, as can be seen from the Equation 6.5, this parameter is related to the second derivative of one of the observable from DFT. DFT usually can not properly describe even first derivative of such quantities.

$$B = V \left(\frac{\partial^2 E}{\partial V^2} \right) = \frac{4}{9a} \frac{\partial^2 E}{\partial a^2} \quad (6.5)$$

Where B is the bulk modulus, V is the equilibrium volume, a is the lattice parameter and E may be the cohesive energy.

The discrepancy in this property however poses minimal or no problem to the aimed description of the gold-water system.

6.3.3 Cohesive Energy

Another property usually applied to examine the quality of the metal slab description is the cohesive energy (the difference between the total energies of the atom in the bulk and the isolated atom). This is equivalent to the enthalpic difference from the arrangement of atoms in a crystalline state and in the gas state.

The cohesive energy (E_{coh}) was computed according to formula

$$E_{coh} = \frac{E_{tot}^{solid} - n \cdot E_{iso}^{atom}}{n} \quad (6.6)$$

where E_{tot}^{solid} is the total energy of the elements in their ground-state crystal structures, E_{iso}^{atom} is the energy of an isolated atom, and n is the number of atoms in the crystal.

The energies were obtained after structural relaxation of the gold slab. E_{tot}^{solid} is simply the total energy. To calculate E_{iso}^{atom} , first all but one atom were turned into ghost atoms.

The cohesive energy was -2.71 eV/atom. The value is negative, which indicates that this phase (Au(111)) is energetically favorable which is in agreement with the literature. However, this value is more than 1 eV below the experimental (3.81 eV¹³²) and a 15% discrepancy from the value of -3.20 eV/atom reported by Wang *et al*¹³³ from another DFT-GGA calculation. Using a Hartree-Fock based method, the value has the opposite trend, overestimating the experimental (3.99¹³⁴ converting from kcal/mol). The same occurs comparing when using empirical electron theory (EET), the result is 3.85 eV¹³⁰ converting from kJ/mol.

6.3.4 Work Function

For a clean surface, the work function ϕ denotes the energy required to promote one electron from Fermi energy level to the vacuum level. It is a sensitive parameter of the surface geometry that can help elucidate many phenomena at the interface.

The work function was obtained from a structural relaxation procedure of the gold slab using the DFT framework. Fermi energy was retrieved from the eigenvalues of the Kohn-Sham set of equations. In the case of SIESTA a correction was required for the

alignment of the electrostatic potential due to the use of pseudo-potentials. The vacuum level was defined as the effective potential at grid points with zero density.

There are many techniques to empirically evaluate the work function of a metal slab. Two types of them were used to compare the results: the photoemission valence band width and contact potential difference (CPD). This work's value is in good agreement to the mean value between these experimental data.

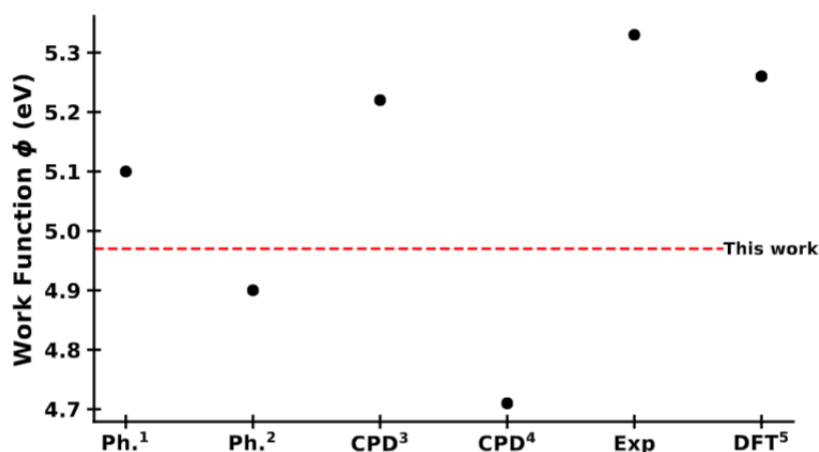


Figure 6.5: Determined work function of gold. Dots represents values using different functionals reported by Huzayyin⁸ and experimental values reported by Hansson.¹¹⁷

As mentioned, work function is a sensible parameter. The crystallographic orientation, surface defects, reconstruction and other surface related phenomena have a strong effect. Comparing with the experimental value of 5.26 ± 0.04 eV, reported by Hansson¹¹⁷ this work's value have an error of 10%.

6.3.5 Water TIP3P

According to Jorgensen *et al.*,¹⁰⁶ the water in this model has the properties describe in table 6.4

	r(OH)(Å)	\angle HOH (°)	A (10^3 kcal Å ¹² /mol)	B (kcal Å ⁶ /mol)	q(O)	q(H)
TIP3P	0.9572	104.52	582.0	595.0	-0.834	+0.417

Table 6.4: Properties of water TIP3P model.

6.3.6 Charges

The charges from the RESP fitting, for each of the fifteen relevant sites, in each set of restrictions, in each image group are reported in Tables 6.5 to 6.8. Specifically for the target image 5 the data is represented in Figure 4.15.

		Image 1				Image 2			
		Free	M0free	M0Same	Same	Free	M0free	M0Same	Same
Site 111	Au	-0.005	0.023	0.011	0.002	-0.005	-0.009	0.003	0.005
	HR	-0.005	0.021	-0.011	0.002	-0.005	-0.010	-0.004	0.003
Site 113	Au	-0.005	-0.003	0.011	0.002	-0.006	0.001	0.003	0.005
	HR	-0.005	-0.004	-0.011	0.002	-0.006	0.000	-0.004	0.003
Site 123	Au	-0.007	-0.002	0.011	0.002	-0.005	-0.004	0.003	0.005
	HR	-0.007	0.001	-0.011	0.002	-0.005	-0.005	-0.004	0.003
Site 125	Au	0.002	0.032	0.011	0.002	0.005	0.014	0.003	0.005
	HR	0.002	0.031	-0.011	0.002	0.004	0.013	-0.004	0.003
Site 127	Au	-0.001	-0.011	0.011	0.002	-0.004	0.002	0.003	0.005
	HR	-0.001	-0.011	-0.011	0.002	-0.004	0.001	-0.004	0.003
Site 135	Au	-0.003	-0.014	0.011	0.002	-0.002	-0.011	0.003	0.005
	HR	-0.003	-0.011	-0.011	0.002	-0.003	-0.012	-0.004	0.003
Site 137	Au	-0.002	0.004	0.011	0.002	0.001	-0.012	0.003	0.005
	HR	-0.001	0.006	-0.011	0.002	0.000	-0.012	-0.004	0.003
Site 149	Au	0.016	0.004	0.011	0.002	0.017	0.005	0.003	0.005
	HR	0.016	0.005	-0.011	0.002	0.018	0.006	-0.004	0.003
Site 159	Au	-0.003	-0.016	0.011	0.002	-0.004	-0.006	0.003	0.005
	HR	-0.002	-0.006	-0.011	0.002	-0.002	-0.001	-0.004	0.003
Site 161	Au	-0.008	-0.009	0.011	0.002	-0.004	-0.005	0.003	0.005
	HR	-0.007	-0.003	-0.011	0.002	-0.001	-0.001	-0.004	0.003
Site 171	Au	-0.003	-0.004	0.011	0.002	-0.001	0.004	0.003	0.005
	HR	-0.004	-0.011	-0.011	0.002	-0.003	-0.001	-0.004	0.003
Site 173	Au	0.005	-0.002	0.011	0.002	-0.004	-0.016	0.003	0.005
	HR	0.020	0.011	-0.011	0.002	0.023	0.017	-0.004	0.003
Site 175	Au	-0.005	0.001	0.011	0.002	-0.002	0.000	0.003	0.005
	HR	-0.007	-0.008	-0.011	0.002	-0.005	-0.005	-0.004	0.003
Site 183	Au	0.005	0.002	0.011	0.002	0.005	0.002	0.003	0.005
	HR	-0.001	-0.012	-0.011	0.002	0.005	0.011	-0.004	0.003
Site 185	Au	-0.002	-0.003	0.011	0.002	0.006	0.002	0.003	0.005
	HR	-0.007	0.000	-0.011	0.002	0.010	0.011	-0.004	0.003

Table 6.5: Charges from the RESP fitting, for each of the fifteen relevant sites, in each set of restrictions, in Images 1 and 2.

		Image 3				Image 4			
		Free	M0free	M0Same	Same	Free	M0free	M0Same	Same
Site 111	Au	-0.005	-0.003	0.009	0.000	-0.005	0.015	0.002	0.002
	HR	-0.005	-0.004	-0.009	0.001	-0.005	0.013	-0.002	0.001
Site 113	Au	-0.005	-0.006	0.009	0.000	-0.004	0.001	0.002	0.002
	HR	-0.005	-0.007	-0.009	0.001	-0.004	0.000	-0.002	0.001
Site 123	Au	-0.001	-0.005	0.009	0.000	-0.007	-0.003	0.002	0.002
	HR	-0.001	-0.006	-0.009	0.001	-0.007	-0.001	-0.002	0.001
Site 125	Au	0.003	0.014	0.009	0.000	0.002	0.027	0.002	0.002
	HR	0.002	0.013	-0.009	0.001	0.002	0.026	-0.002	0.001
Site 127	Au	-0.002	-0.011	0.009	0.000	-0.002	-0.015	0.002	0.002
	HR	-0.002	-0.012	-0.009	0.001	-0.001	-0.015	-0.002	0.001
Site 135	Au	-0.002	0.002	0.009	0.000	-0.003	-0.014	0.002	0.002
	HR	-0.002	0.003	-0.009	0.001	-0.003	-0.012	-0.002	0.001
Site 137	Au	-0.001	0.009	0.009	0.000	-0.002	0.003	0.002	0.002
	HR	-0.001	0.010	-0.009	0.001	-0.002	0.005	-0.002	0.001
Site 149	Au	0.015	0.007	0.009	0.000	0.016	0.007	0.002	0.002
	HR	0.016	0.008	-0.009	0.001	0.015	0.006	-0.002	0.001
Site 159	Au	-0.007	-0.008	0.009	0.000	-0.005	-0.014	0.002	0.002
	HR	-0.006	-0.004	-0.009	0.001	-0.004	-0.006	-0.002	0.001
Site 161	Au	-0.007	-0.004	0.009	0.000	-0.012	-0.010	0.002	0.002
	HR	-0.005	-0.003	-0.009	0.001	-0.010	-0.006	-0.002	0.001
Site 171	Au	-0.003	0.004	0.009	0.000	-0.004	-0.002	0.002	0.002
	HR	-0.006	-0.001	-0.009	0.001	-0.006	-0.007	-0.002	0.001
Site 173	Au	0.002	-0.009	0.009	0.000	0.005	-0.003	0.002	0.002
	HR	0.019	0.016	-0.009	0.001	0.019	0.012	-0.002	0.001
Site 175	Au	-0.006	0.004	0.009	0.000	-0.009	0.002	0.002	0.002
	HR	-0.008	-0.002	-0.009	0.001	-0.011	-0.005	-0.002	0.001
Site 183	Au	-0.002	-0.001	0.009	0.000	0.004	0.002	0.002	0.002
	HR	-0.007	0.000	-0.009	0.001	-0.002	-0.011	-0.002	0.001
Site 185	Au	-0.002	-0.002	0.009	0.000	-0.004	-0.002	0.002	0.002
	HR	-0.006	0.006	-0.009	0.001	-0.008	0.001	-0.002	0.001

Table 6.6: Charges from the RESP fitting, for each of the fifteen relevant sites, in each set of restrictions, in Images 3 and 4.

		Image 6				Image 7			
		Free	M0free	M0Same	Same	Free	M0free	M0Same	Same
Site 111	Au	-0.004	-0.003	0.001	0.001	-0.004	0.022	0.013	0.001
	HR	-0.005	-0.004	-0.002	0.000	-0.004	0.020	-0.013	0.002
Site 113	Au	-0.003	-0.009	0.001	0.001	-0.005	0.007	0.013	0.001
	HR	-0.004	-0.010	-0.002	0.000	-0.005	0.006	-0.013	0.002
Site 123	Au	-0.004	-0.006	0.001	0.001	-0.008	-0.005	0.013	0.001
	HR	-0.004	-0.006	-0.002	0.000	-0.008	-0.002	-0.013	0.002
Site 125	Au	0.002	0.010	0.001	0.001	0.005	0.042	0.013	0.001
	HR	0.002	0.009	-0.002	0.000	0.005	0.041	-0.013	0.002
Site 127	Au	-0.002	-0.010	0.001	0.001	-0.005	-0.020	0.013	0.001
	HR	-0.002	-0.011	-0.002	0.000	-0.005	-0.019	-0.013	0.002
Site 135	Au	-0.003	0.000	0.001	0.001	0.002	-0.005	0.013	0.001
	HR	-0.002	0.001	-0.002	0.000	0.002	0.000	-0.013	0.002
Site 137	Au	-0.001	0.009	0.001	0.001	0.000	0.000	0.013	0.001
	HR	-0.001	0.009	-0.002	0.000	0.000	0.003	-0.013	0.002
Site 149	Au	0.012	0.005	0.001	0.001	0.014	0.008	0.013	0.001
	HR	0.011	0.005	-0.002	0.000	0.013	0.007	-0.013	0.002
Site 159	Au	-0.010	-0.007	0.001	0.001	-0.005	-0.016	0.013	0.001
	HR	-0.009	-0.004	-0.002	0.000	-0.004	-0.007	-0.013	0.002
Site 161	Au	-0.012	-0.005	0.001	0.001	-0.012	-0.010	0.013	0.001
	HR	-0.010	-0.004	-0.002	0.000	-0.010	-0.007	-0.013	0.002
Site 171	Au	-0.004	0.004	0.001	0.001	-0.005	-0.004	0.013	0.001
	HR	-0.006	0.000	-0.002	0.000	-0.006	-0.010	-0.013	0.002
Site 173	Au	0.001	-0.009	0.001	0.001	0.000	0.001	0.013	0.001
	HR	0.017	0.017	-0.002	0.000	0.018	0.008	-0.013	0.002
Site 175	Au	-0.009	0.004	0.001	0.001	-0.006	0.000	0.013	0.001
	HR	-0.011	0.000	-0.002	0.000	-0.009	-0.007	-0.013	0.002
Site 183	Au	-0.002	0.000	0.001	0.001	0.004	0.004	0.013	0.001
	HR	-0.007	0.001	-0.002	0.000	-0.001	-0.022	-0.013	0.002
Site 185	Au	-0.003	-0.002	0.001	0.001	0.002	0.002	0.013	0.001
	HR	-0.007	0.006	-0.002	0.000	0.001	-0.006	-0.013	0.002

Table 6.7: Charges from the RESP fitting, for each of the fifteen relevant sites, in each set of restrictions, in Images 6 and 7.

		Image 8				Image 9			
		Free	M0free	M0Same	Same	Free	M0free	M0Same	Same
Site 111	Au	-0.004	-0.002	0.008	0.002	-0.004	0.002	0.010	0.002
	HR	-0.004	-0.003	-0.008	0.000	-0.004	0.001	-0.010	0.001
Site 113	Au	-0.004	0.007	0.008	0.002	-0.004	-0.004	0.010	0.002
	HR	-0.004	0.006	-0.008	0.000	-0.004	-0.005	-0.010	0.001
Site 123	Au	-0.006	-0.018	0.008	0.002	-0.005	-0.013	0.010	0.002
	HR	-0.005	-0.018	-0.008	0.000	-0.005	-0.013	-0.010	0.001
Site 125	Au	0.004	0.023	0.008	0.002	0.004	0.020	0.010	0.002
	HR	0.003	0.022	-0.008	0.000	0.004	0.019	-0.010	0.001
Site 127	Au	-0.005	-0.013	0.008	0.002	-0.005	-0.018	0.010	0.002
	HR	-0.005	-0.012	-0.008	0.000	-0.004	-0.019	-0.010	0.001
Site 135	Au	0.000	0.000	0.008	0.002	0.000	-0.002	0.010	0.002
	HR	0.000	0.002	-0.008	0.000	-0.001	0.001	-0.010	0.001
Site 137	Au	0.003	0.002	0.008	0.002	0.001	0.007	0.010	0.002
	HR	0.002	0.004	-0.008	0.000	0.000	0.009	-0.010	0.001
Site 149	Au	0.008	0.009	0.008	0.002	0.011	0.005	0.010	0.002
	HR	0.007	0.008	-0.008	0.000	0.010	0.005	-0.010	0.001
Site 159	Au	-0.010	-0.010	0.008	0.002	-0.011	-0.008	0.010	0.002
	HR	-0.007	-0.006	-0.008	0.000	-0.009	-0.005	-0.010	0.001
Site 161	Au	-0.010	-0.008	0.008	0.002	-0.011	-0.006	0.010	0.002
	HR	-0.006	-0.006	-0.008	0.000	-0.008	-0.005	-0.010	0.001
Site 171	Au	-0.004	0.006	0.008	0.002	-0.004	0.004	0.010	0.002
	HR	-0.006	0.000	-0.008	0.000	-0.006	-0.001	-0.010	0.001
Site 173	Au	-0.004	-0.007	0.008	0.002	-0.004	-0.007	0.010	0.002
	HR	0.019	0.014	-0.008	0.000	0.018	0.014	-0.010	0.001
Site 175	Au	-0.004	0.001	0.008	0.002	-0.006	0.004	0.010	0.002
	HR	-0.006	-0.004	-0.008	0.000	-0.009	-0.001	-0.010	0.001
Site 183	Au	0.003	0.003	0.008	0.002	0.003	0.004	0.010	0.002
	HR	0.001	-0.002	-0.008	0.000	0.000	-0.004	-0.010	0.001
Site 185	Au	0.003	0.003	0.008	0.002	0.003	0.002	0.010	0.002
	HR	0.002	-0.003	-0.008	0.000	0.001	0.000	-0.010	0.001

Table 6.8: Charges from the RESP fitting, for each of the fifteen relevant sites, in each set of restrictions, in Images 8 and 9.

		M0free				Qtot-Image
Image\Layer	Element	1	2	3	4	
1	Au	0.000	0.000	0.001	-0.001	0.012
	HR	0.000	0.000	0.001	-0.001	
2	Au	0.000	0.000	-0.001	-0.001	-0.020
	HR	0.000	0.000	-0.001	0.002	
3	Au	0.000	0.000	0.000	0.000	0.007
	HR	0.000	0.000	0.000	0.001	
4	Au	0.000	0.000	0.001	-0.001	-0.005
	HR	0.000	0.000	0.001	-0.001	
5	Au	0.000	0.000	0.000	0.002	0.000
	HR	0.000	0.000	0.000	-0.002	
6	Au	0.000	0.000	0.000	0.000	-0.011
	HR	0.000	0.000	0.000	0.001	
7	Au	0.000	0.000	0.002	-0.001	0.028
	HR	0.000	0.000	0.002	-0.002	
8	Au	0.000	0.000	0.000	0.000	0.000
	HR	0.000	0.000	0.000	0.000	
9	Au	0.000	0.000	0.000	0.000	-0.011
	HR	0.000	0.000	0.000	0.000	

		M0Same				Qtot-Image
Image\Layer	Element	1	2	3	4	
1	Au	0.000	0.000	0.003	0.004	0.005
	HR	0.000	0.000	-0.003	-0.004	
2	Au	0.000	0.000	0.001	0.001	-0.004
	HR	0.000	0.000	-0.001	-0.001	
3	Au	0.000	0.000	0.003	0.003	0.003
	HR	0.000	0.000	-0.003	-0.003	
4	Au	0.000	0.000	0.001	0.001	-0.007
	HR	0.000	0.000	-0.001	-0.001	
5	Au	0.000	0.000	0.002	0.002	0.000
	HR	0.000	0.000	-0.002	-0.002	
6	Au	0.000	0.000	0.000	0.000	-0.007
	HR	0.000	0.000	0.000	-0.001	
7	Au	0.000	0.000	0.004	0.004	0.007
	HR	0.000	0.000	-0.004	-0.004	
8	Au	0.000	0.000	0.002	0.003	-0.002
	HR	0.000	0.000	-0.002	-0.003	
9	Au	0.000	0.000	0.003	0.003	0.005
	HR	0.000	0.000	-0.003	-0.003	

6.3.7 Lennard Jonnes parameters

The graphs of the potential energy, with the contributions from the interactions between metal and oxygen and between metal and hydrogen, for the configurations “Flat-Down” and “Up” after the procedure described in Sections 3.6 and 4.4 imposing the criteria $\epsilon_O = 2\epsilon_H$, are shown in Figures 6.6 and 6.7, respectively:

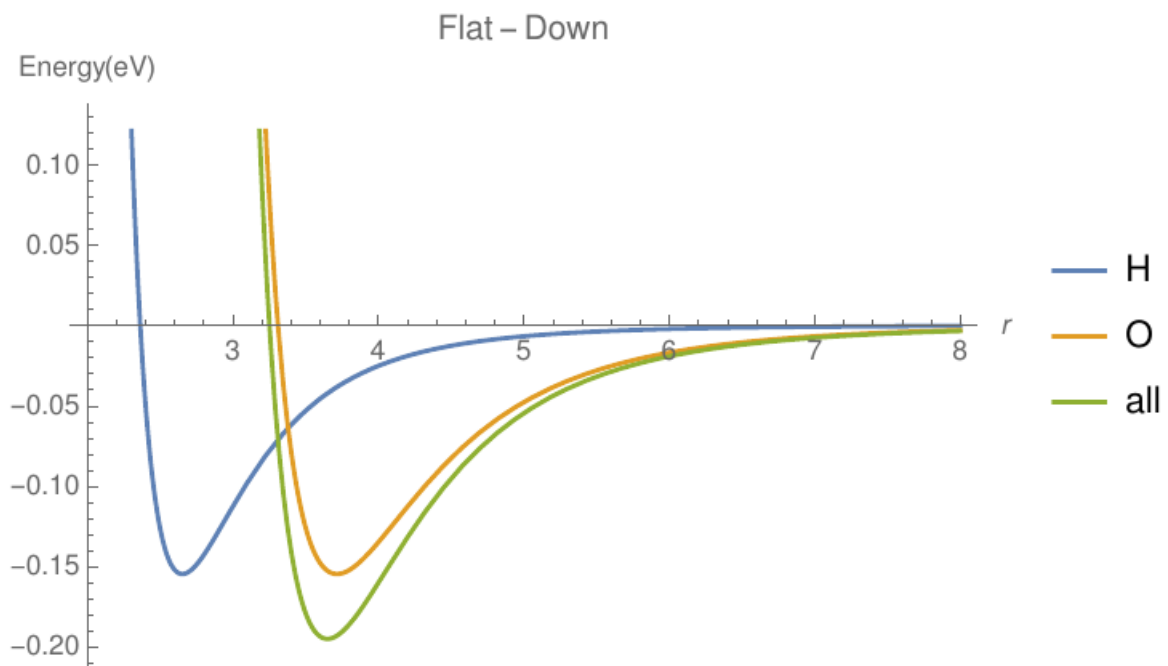


Figure 6.6: Assessment of the range of the Lennard Jones parameters with water at the flat-down configuration.

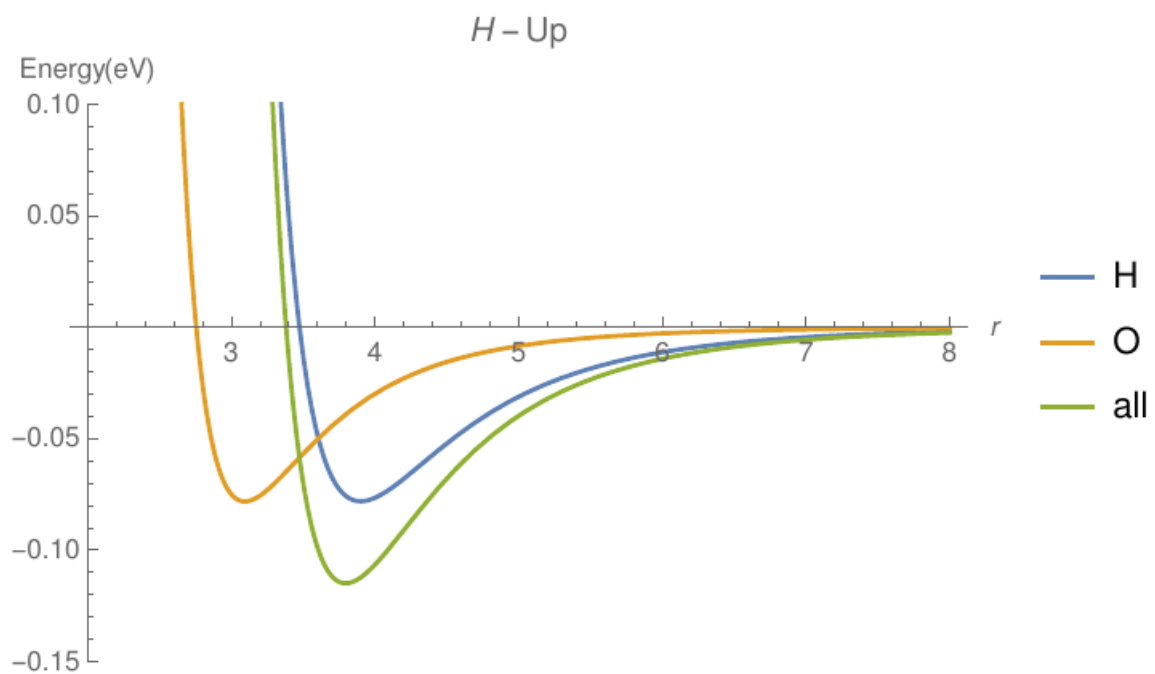


Figure 6.7: Assessment of the range of the Lennard Jones parameters with water at the up configuration.